Since 1955

Strojniški vestnik
Journal of Mechanical Engineering

no. 1-2
year 2023
volume 69

Strojniški vestnik – Journal of Mechanical Engineering (SV-JME)

Aim and Scope
The international journal publishes original and (mini)review articles covering the concepts of materials science, mechanics, kinematics, thermodynamics, energy and environment, mechatronics and robotics, fluid mechanics, tribology, cybernetics, industrial engineering and structural analysis.
The journal follows new trends and progress proven practice in the mechanical engineering and also in the closely related sciences as are electrical, civil and process engineering, medicine, microbiology, ecology, agriculture, transport systems, aviation, and others, thus creating a unique forum for interdisciplinary or multidisciplinary dialogue.
The international conferences selected papers are welcome for publishing as a special issue of SV-JME with invited co-editor(s).

Editorial Office
University of Ljubljana, Faculty of Mechanical Engineering
SV-JME, Aškerčeva 6, SI-1000 Ljubljana, Slovenia
Phone: 386 (0)1 4771 137
Fax: 386 (0)1 2518 567
info@sv-jme.eu, http://www.sv-jme.eu

Print: Demat d.o.o., printed in 240 copies

Founders and Publishers
University of Ljubljana, Faculty of Mechanical Engineering, Slovenia
University of Maribor, Faculty of Mechanical Engineering, Slovenia
Association of Mechanical Engineers of Slovenia
Chamber of Commerce and Industry of Slovenia, Metal Processing Industry Association

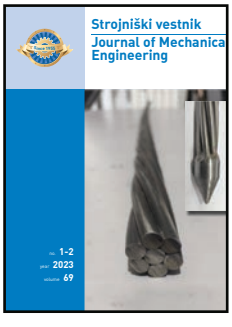

Cover:
To explore the dynamic characteristics of drilling an anchor cable in the gravel sediments of bottom holes, an anchor cable drilling experiment was carried out with and without a drill bit by using the designed anchor cable drilling test bed. The gravel drilling experiments were performed using different motion parameters, hole diameters, particle humidity, and particle types to obtain the dynamic characteristics of bit anchor cable drilling under various conditions

Image Courtesy:
Authors, Shandong University of Science and Technology, College of Mechanical and Electrical Engineering, China

General information
Strojniški vestnik – Journal of Mechanical Engineering is published in 11 issues per year (July and August is a double issue).

Institutional prices include print & online access: institutional subscription price and foreign subscription €100,00 (the price of a single issue is €10,00); general public subscription and student subscription €50,00 (the price of a single issue is €5,00). Prices are exclusive of tax. Delivery is included in the price. The recipient is responsible for paying any import duties or taxes. Legal title passes to the customer on dispatch by our distributor. Single issues from current and recent volumes are available at the current single-issue price. To order the journal, please complete the form on our website. For submissions, subscriptions and all other information please visit: *http://www.sv-jme.eu.*

You can advertise on the inner and outer side of the back cover of the journal. The authors of the published papers are invited to send photos or pictures with short explanation for cover content.

We would like to thank the reviewers who have taken part in the peer-review process.

ISSN 0039-2480, ISSN 2536-2948 (online)

The journal is subsidized by Slovenian Research Agency.

SV-JME is indexed / abstracted in: SCI-Expanded, Compendex, Inspec, ProQuest-CSA, SCOPUS, TEMA. The list of the remaining bases, in which SV-JME is indexed, is available on the website.

Strojniški vestnik - Journal of Mechanical Engineering is available on *https://www.sv-jme.eu.*

Contents

Strojniški vestnik - Journal of Mechanical Engineering
volume 69, (2023), number 1-2
Ljubljana, January-February 2023
ISSN 0039-2480

Published monthly

Papers

Strojniški vestnik - Journal of Mechanical Engineering 69(2023)1-2, 3-16

DOI:10.5545/sv-jme.2022.383
Original Scientific Paper
Received for review: 2022-09-26
Received revised form: 2022-12-13
Accepted for publication: 2023-01-04

Study on the Dynamic Characteristics of Bit Anchor Cable Drilling in the Gravel Sediments of a Soft Rock Bottom Hole

Kuidong Gao[1,2] – Jihai Liu[1,2,*] – Qingliang Zeng[3] – Jingyi Cheng[4] – Liqing Sun[1] – Lisong Lin[1,2]

[1] Shandong University of Science and Technology, College of Mechanical and Electrical Engineering, China
[2] Shandong University of Science and Technology, Key Laboratory of Mine Mechanical Engineering, China
[3] Shandong Normal University, School of Information Science and Engineering, China
[4] China University of Mining and Technology, School of Mines, China

During the pore-forming stage of floor heave treatment, the phenomenon of gravel sediment accumulation in the bottom hole often occurs, which causes great difficulties in the normal installation of the anchor cable. Based on this observation, a new anchor cable installation method was proposed, which involves installing a drill bit at the front end of the anchor cable to assist its drilling. With the help of an anchor cable drilling test bench, the influence of the bit, motion parameters, and hole environment on the performance of anchor cable drilling was studied. Through the co-simulation of the discrete element method (i.e., multibody dynamics (DEM-MBD)), the drilling process of the bit anchor cable was simulated, and the dynamic characteristics of the bit anchor cable drilling in the bottom hole gravel sediment were analysed. The results show that installing a drill bit in front of the anchor cable can greatly reduce the drilling resistance and hamper torque during anchor cable drilling. When the rotational direction of the bit anchor cable is consistent with the spiral direction of the anchor cable, the bit anchor cable can exhibit better drilling performance. The drilling resistance and hindering torque of the bit anchor cable are the largest when drilling in soaked particles, followed by drilling in dry particles, and the smallest occurs when drilling in moist particles. The research results can provide reference for the parameter setting of anchor cable auxiliary installation equipment.

Keywords: bit, anchor cable, gravel drilling, dynamic characteristic

Highlights

- *A method of bit anchor cable installation applied to gravel environment in hole was proposed.*
- *The experiment proved the feasibility of drilling the gravels in the hole with bit anchor cable.*
- *The clockwise rotation was beneficial to drilling of bit anchor cable.*
- *Rotational speed, moist particle, large particle diameter and regular shape gravel played an active role in bit anchor cable drilling.*

0 INTRODUCTION

The stability control of soft rock roadways has always been a technical problem in coal mine production and construction, especially with floor heave in the nonlinear large deformation control of soft rock roadways [1] to [3]. Floor heave will reduce the section size, hinder normal transportation, impede ventilation, and easily cause safety accidents in the roadway. Floor heave seriously restricts the safety and efficiency of coal mining [4] to [6].

As shown in Fig. 1, the main method used to solve the problem of roadway floor heave involves using an anchor cable to directly control the floor to maximize the radial stress of the floor rock mass [7] to [9]. However, due to the complexity and uncertainty of the floor rock mass, the phenomenon of hole wall instability often appears in the pore-forming stage, resulting in the accumulation of gravel sediments in the bottom hole. This sediment accumulation will greatly hinder the normal installation of anchor cables. At present, the main solution to this problem is the manual installation of anchor cables, which manually control the installation path of the anchor cable so that it can be installed close to the bottom of the borehole. However, the front end of the anchor cable is blunt, giving it a large installation resistance and low installation efficiency. In order to improve the installation efficiency of the anchor cable in the hole, auxiliary installation equipment of anchor cable was designed, as shown in Fig. 4, and a new installation method for anchor cables in the hole by installing a drill bit at the front end of the cable was proposed.

Using numerical calculation, Lin et al. [10] comparatively analysed the variation characteristics of anchor cable structure displacement under static conditions. Li and Li [11] proposed a new pressure-type anchor cable with a precast anchor head. Tao et al. [12] established the nonlinear thermomechanical coupling analysis model of the finite element structure of constant resistance by using ANSYS software. Shi et al. [13] and [14] predicted the law of the anchoring force loss through the established coupling calculation model. Yang et al. [15] studied the variation of anchor

*Corr. Author's Address: Shandong University of Science and Technology, College of Mechanical and Electrical Engineering, China, ljhsdust@163.com

cable tension by monitoring the tensile behaviour of the selected anchor cable. Wang et al. [16] studied the mechanical properties of the anchor cable under the tension-torsion coupling effect by using the established three-dimensional computational model. Through the established seabed model, Sun et al. [17] explored the relationship between the normal seabed friction coefficient and the anchor cable tension. At present, most of the research performed on anchor cables focuses on their properties and applications. There are relatively few studies on the installation of anchor cables in gravel sediments in bottom holes.

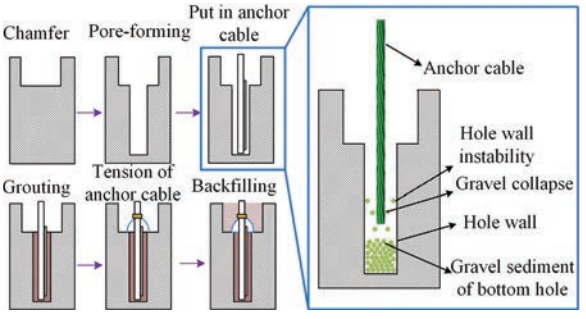

Fig. 1. *Background*

In 1971, Cundall first proposed an analysis method for discrete particles based on molecular dynamics theory [18] to [20]; the method then gradually developed into the discrete element method (DEM) [21] to [23]. The DEM method can construct the particle environment of a discrete material and can analyse the motion law of the particle under an external force [24] to [26]. However, the existing DEM software is weak in the mechanical analysis of the geometry in particles. This problem can be solved with the discrete element method and multi-body dynamic method (DEM-MBD) co-simulation. The DEM-MBD co-simulation is presently widely used in particle dynamics analysis [27], particle breakage experiment [28], and mechanical property analysis [29].

To explore the dynamic characteristics of drilling an anchor cable in the gravel sediments of bottom holes, an anchor cable drilling experiment was carried out with and without a drill bit by using the designed anchor cable drilling test bed. The gravel drilling experiments were performed using different motion parameters, hole diameters, particle humidity, and particle types to obtain the dynamic characteristics of bit anchor cable drilling under various conditions. Additionally, DEM-MBD co-simulation was used to simulate the drilling process of the bit anchor cable in the gravel sediments of a bottom hole, and the motion law of the gravel particles in the hole was obtained by drilling the bit anchor cable under different motion parameters.

The present research solves the difficulty of anchor cable installation caused by the accumulation of gravel in the hole. The anchor cable auxiliary installation equipment can solve the problems of the low efficiency and high cost of manual installation of anchor cable. The effect of the bit anchor cable on the motion of discrete particles is revealed by DEM-MBD. It is proved that the drilling process of the bit anchor cable is also a process in which the stable structure of gravel is constantly broken and rebuilt. The favourable factors of bit anchor cable installation in the environment of gravel accumulation in the hole have been determined: bit anchor cable clockwise rotation, low forward speed, high rotational speed, moist gravel particles, particle diameter 10 mm to 13 mm and regular particle shape.

1 SIMULATION MODELS AND TEST

1.1 Simulation Model

The Hertz-Mindlin (no-slip) contact model is the most commonly used model in discrete element simulation. This model has the benefits of high accuracy and high computational efficiency. DEM-MBD is a common method for simulating the motion

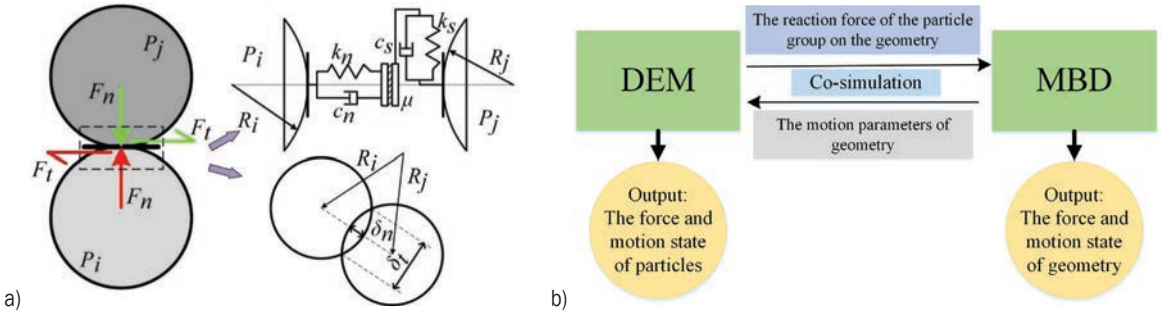

Fig. 2. *Simulation mode; a) Hertz-Mindlin (no-slip) contact model, and b) DEM-MBD co-simulation model*

of geometry in discrete particles [27] and [29]. The schematic diagram of DEM is shown in Fig. 2a. The co-simulation diagram of DEM-MBD is shown in Fig. 2b. The contact forces between particles include the normal contact force, tangential contact force and friction force. The dynamic system of normal contact force and tangential contact force is a spring-damping system. In DEM, it is assumed that the gravel pieces have the same diameter and will not be damaged or deformed under the action of external forces. In MBD, it is assumed that the anchor cable is a rigid body. The anchor cable will not bend and change its motion state under the action of external forces.

In Fig. 2 P_i is the discrete particle with radius R_i; P_j is the discrete particle with radius R_j; F_t is the tangential contact force, [N]; F_n is the normal contact force, [N]; K_s is the tangential elastic coefficient; K_n is the normal elastic coefficient; c_s is tangential damping coefficient; c_n is the normal damping coefficient; μ is the friction coefficient; δ_n is the overlap width of the particles, [m]; δ_t is the overlap length of the particles, [m].

When gravel sediments accumulate at the bottom of the hole, the most common solution is manual installation. The installation path of the anchor cable is manually controlled so that the anchor cable can be installed near the bottom of the borehole. However, manual installation has its shortcomings because the front end of the anchor cable is blunt, the installation resistance of the anchor cable is large, the installation efficiency is low, and the technique is labour-intensive. Based on these disadvantages, a new anchor cable installation method was proposed, in which a drill bit was installed at the front end of the anchor cable so that the bit could assist the anchor cable drilling. The constructed simulation model of the bit anchor cable drilling into the bottom hole gravels is shown in Fig. 3.

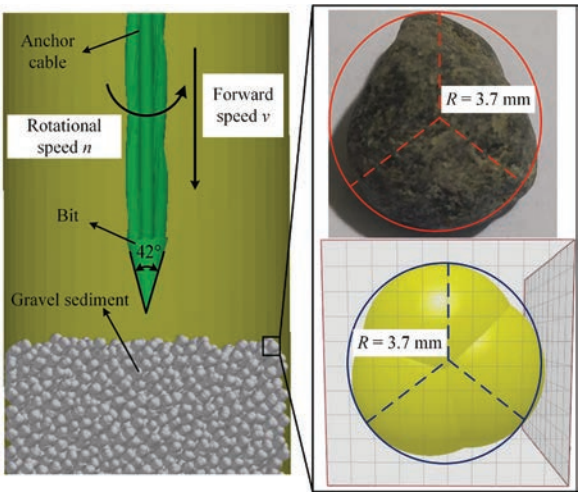

Fig. 3. *Simulation model of drilling bottom hole gravel with a bit anchor cable*

Table 1. *The parameters of DEM* [27]

	ρ [kg/m³]	σ	G [GPa]		η	μ_S	μ_R
Gravel	2700	0.29	11	Gravel – Gravel	0.62	0.74	0.2
Anchor cable	7801	0.29	8.02	Gravel – Anchor cable	0.42	0.49	0.25

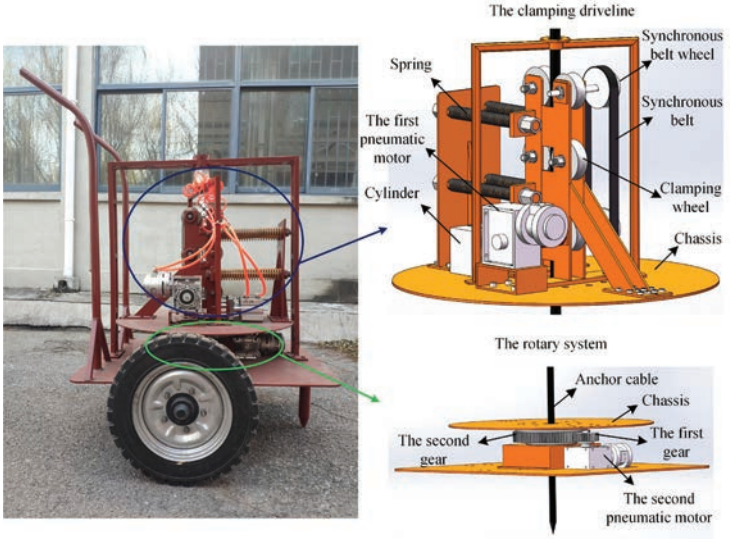

Fig. 4. *Anchor cable auxiliary installation equipment*

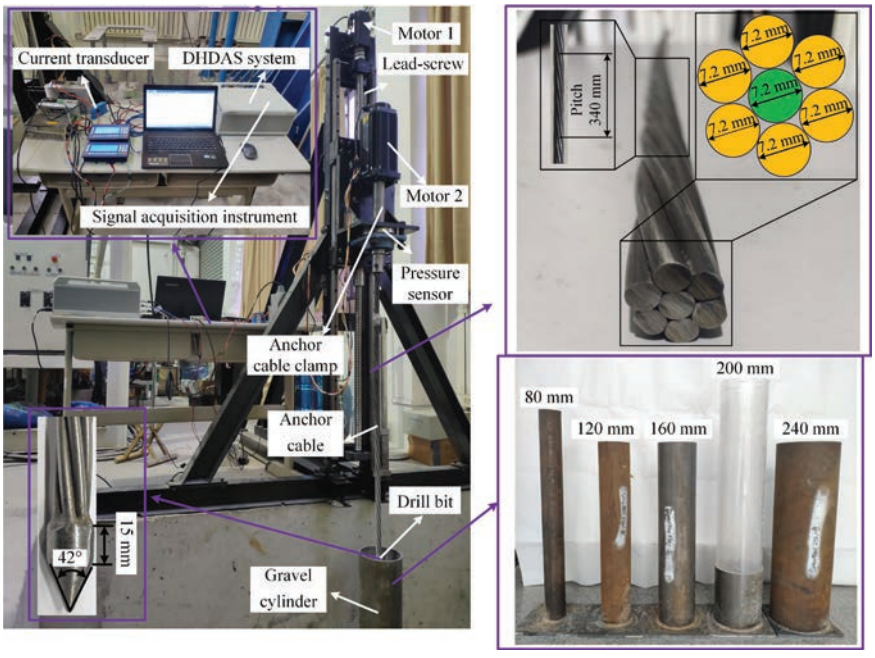

Fig. 5. *Anchor cable drilling test bed*

In Table 1 ρ is the density, σ is Poisson's ratio, G is the shear modulus, η is the coefficient of restitution, μ_S is the coefficient of static friction, and μ_R is the coefficient of rolling friction.

1.2 Test Bed

In order to improve the installation efficiency of the anchor cable in the hole, auxiliary installation equipment for the anchor cable was designed, as shown in Fig. 4; a new installation method of an anchor cable in a hole by installing a drill bit at the front end of anchor cable was proposed. The core system of the auxiliary installation device is the clamping driveline and the rotary system. The clamping of the anchor cable was realized using a cylinder, and the rotary drilling of the anchor cable was realized with two pneumatic motors.

According to the movement characteristics of the anchor cable when drilling in the gravel sediments of the bottom hole, the main structure of the anchor cable drilling test bed is shown in Fig. 5. The lead screw was driven by Motor 1 to rotate, thereby causing the vertical movement of Motor 2 and the anchor cable. The anchor cable clamp was driven by Motor 2 to rotate the anchor cable. Motor 1 and Motor 2 cooperated with each other so that the anchor cable could be drilled in the gravel in the bottom hole.

There were five kinds of gravel cylinders in total, and the diameters of the holes were 80 mm, 120 mm, 160 mm, 200 mm and 240 mm. The sensor signals of the current transducer and pressure sensor were input into the DHDAS dynamic signal acquisition and analysis system through a signal acquisition instrument. The sampling frequency of the system was 1000 Hz.

2 EXPERIMENT AND SIMULATION

Because the drilling depth and hindering torque of the anchor cable could not be measured directly through the experiment, the original data collected needed to be processed again. The current of Motor 2 could be collected through the current transducer, and the torque of Motor 2 could be obtained through Eq. (1). The torque of Motor 2 was also the total torque of the anchor cable. The drilling depth of the anchor cable could be obtained from Eq. (2), and the obstruction effect of gravel particles on the anchor cable could be obtained from Eq. (3).

$$T_1 = \frac{9550P_1}{n} = \frac{9.55\sqrt{3}UI}{n}\cos\varphi\,, \tag{1}$$

where T_1 is the motor torque, [N·m]; P_1 is the power, [W]; n is the rotational speed of Motor 2, [rpm]; U

is the voltage, [V]; I is the current, [A]; cosφ is the power factor.

$$h = P_2 t_1 \frac{n}{60}, \tag{2}$$

where h is the drilling depth of the anchor cable, [m]; P_2 is the screw pitch of the lead screw, [m], and t_1 is the running time of Motor 1, [s].

$$T = T_1 - T_0, \tag{3}$$

where T_0 is the Motor 2 torque when the drill bit just touches the particle, [N·m].

2.1 Feasibility Study on Gravel Sediments Drilling with Bit Anchor Cable

To explore the influence of a drill bit installed on the front end of an anchor cable on drilling the gravel sediment in a bottom hole, gravel drilling experiments of an anchor cable with and without a drill bit were performed. The forward speed of the anchor cable was 0.01 m/s and the rotational speed was 60 rpm. The hole diameter of the gravel cylinder was 160 mm, and the diameters of the gravel sediments were 3 mm to 6 mm. The experimental results are shown in Fig. 6.

Fig. 6 shows that installing a drill bit at the front end of the anchor cable can greatly reduce the braking effect of gravel particles on anchor cable drilling. Fig. 6a shows that at the same drilling depth, the drilling resistance of the anchor cable without a drill bit is the largest when it rotates counter-clockwise, and the drilling resistance of the anchor cable with a drill bit is the smallest when it rotates clockwise.

Fig. 6b shows that when the drilling depth is less than 0.2 m, the hindering torque by counter-clockwise rotation of the anchor cable without a bit is the largest, the clockwise rotation of the anchor cable without a bit is the second largest, and the clockwise rotation of

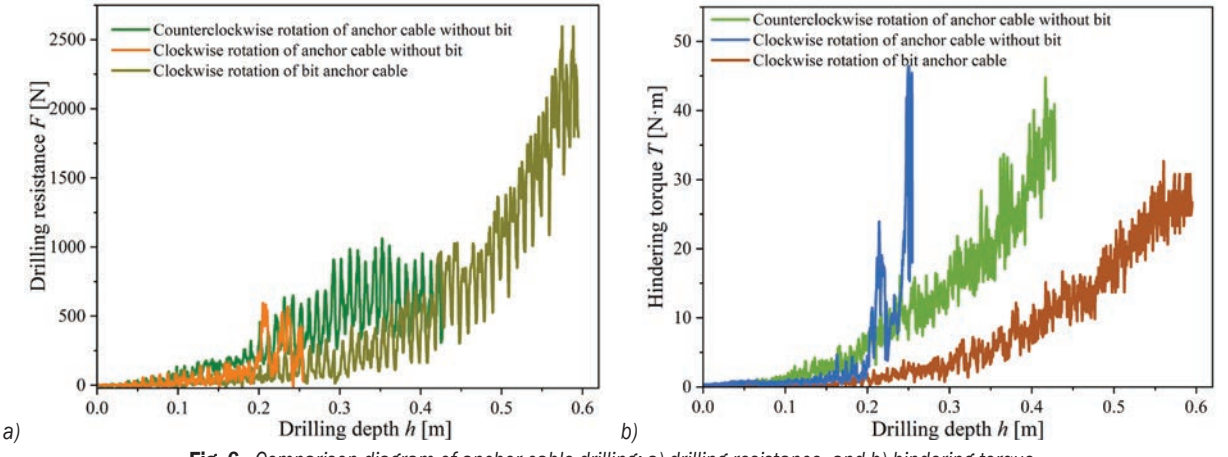

Fig. 6. *Comparison diagram of anchor cable drilling; a) drilling resistance, and b) hindering torque*

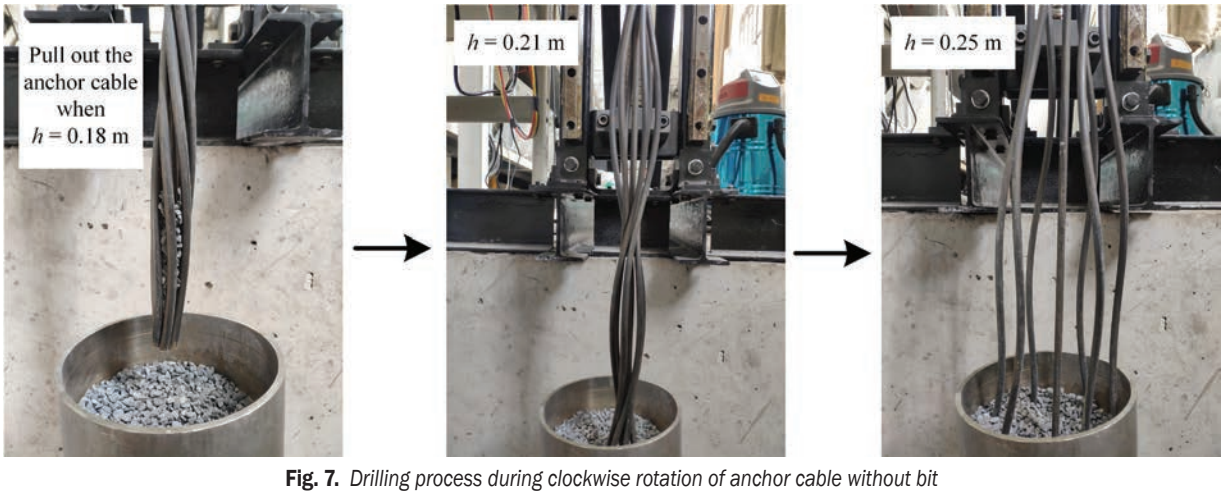

Fig. 7. *Drilling process during clockwise rotation of anchor cable without bit*

the anchor cable with a bit is the smallest. However, when the drilling depth was greater than 0.2 m, the hindering torque by the clockwise rotation of the anchor cable without a bit increased rapidly. When the drilling depth was 0.21 m, the hindering torque reached 24 N·m. When the drilling depth was 0.25 m, the hindering torque reached the maximum value of 46 N·m, and Motor 2 stopped rotating directly under this torque.

The drilling process of clockwise rotation of the anchor cable without a bit is shown in Fig. 7. Because the anchor cable has a specific spiral structure, when the rotational direction of the anchor cable was consistent with the spiral structure direction of the anchor cable, the spiral structure of the anchor cable would be untied under the action of an external force, which would cause a rapid increase in the hindering torque.

According to the results, when the anchor cable without a bit rotated clockwise to drill the gravel sediments in the bottom hole, the spiral structure of the anchor cable was damaged, which led to a rapid increase in the hindering torque. Although the anchor cable without a bit could complete the gravel drilling in the bottom hole by rotating counter-clockwise, the resistance of the anchor cable drilling was significant in the process. After the bit was installed at the front end of the anchor cable, the drilling resistance and hindering torque could be greatly reduced. Therefore, the follow-up study focused on the dynamic characteristics of bit anchor cable gravel drilling.

2.2 Influence of the Motion Parameters on the Dynamic Characteristics of Bit Anchor Cable Drilling

The process of drilling the gravel sediment in the bottom hole with the bit anchor cable primarily used two movements: the forward movement in the vertical direction and the rotary movement around the anchor cable. Because the anchor cable has a specific spiral structure, exploring the influence of the rotational direction and rotational speed on its drilling dynamic characteristics is vital.

2.2.1 Rotational Direction

To explore the influence of the rotational direction on the drilling dynamic characteristics of the bit anchor cable, drilling experiments were carried out under different rotational directions. The inner diameter of the gravel cylinder used in the experiment was 160 mm, the diameters of the gravel sediments were 3 mm to 6 mm, and the forward speed of the bit anchor cable was 0.02 m/s.

Because gravel particles have a certain fluidity, the drilling resistance and hindering torque during bit anchor cable drilling have a certain fluctuation. To facilitate a comparative analysis of the drilling resistance and hindering torque in different rotational directions, Savitzky–Golay smoothing was performed on the curves. Experimental curves after processing are shown in Fig. 8. Fig. 9 shows the average values of the drilling resistance and hindering torque in different rotation directions at drilling depths of 0.5 m to 0.55 m.

Figs. 8 and 9 show that with increasing drilling depth, the drilling resistance and hindering torque of the bit anchor cable during clockwise and counter-

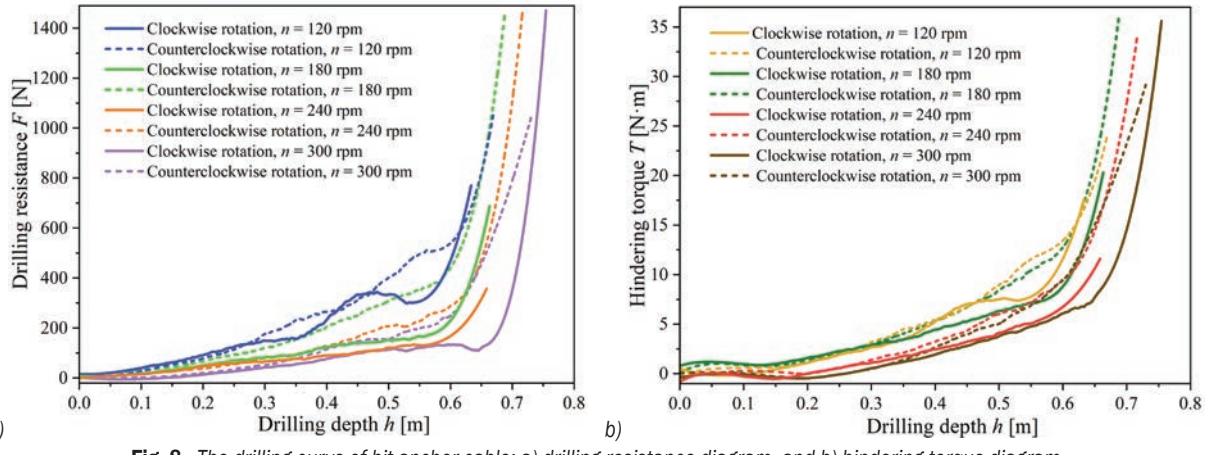

Fig. 8. *The drilling curve of bit anchor cable; a) drilling resistance diagram, and b) hindering torque diagram*

clockwise rotation increased gradually. At the same rotational speed, clockwise rotation was less hindered by particles. The drilling resistance during clockwise rotation of the bit anchor cable was much less than that of counter-clockwise rotation. When the drilling depth was 0.5 m to 0.55 m, the drilling resistance under clockwise rotational speeds of 120 rpm, 180 rpm, 240 rpm and 300 rpm was 36.5 %, 52 %, 43.6 % and 34.9 % lower than that of counter-clockwise rotation, respectively. This phenomenon was caused by the spiral structure of the anchor cable.

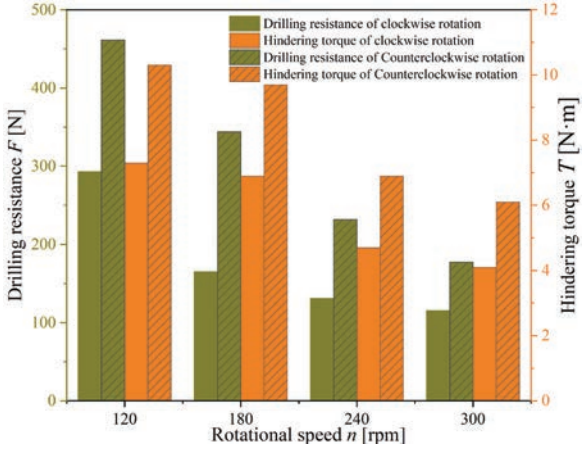

Fig. 9. *Average value of drilling resistance and hindering torque at 0.5 m to 0.55 m*

To explore the influence of the anchor cable spiral structure on gravel particle movement during bit anchor cable drilling, the simulation model in Fig. 3 was numerically simulated by using DEM-MBD co-simulation. When the forward speed was 0.02 m/s, the bit anchor cable rotated clockwise at 120 rpm, 240 rpm and 360 rpm and counter-clockwise at 120 rpm, 240 rpm and 360 rpm to simulate the drilling of gravel sediments in a bottom hole. The drilling resistance curves after Savitzky-Golay smoothing are shown in Fig. 10a. When the bit anchor cable was drilled at a forward speed of 0.02 m/s and a rotational speed of 240 rpm, the comparison of drilling resistance between the simulation and experiment is shown in Fig. 10b, and the comparison of the fitting slope is shown in Table 2.

Table 2. *The fitted slope of drilling resistance*

Condition	Rotational direction	Slope	K_2/K_1
Experiment	Clockwise rotation	$K_1 = 222.1$	1.2
Simulation	Clockwise rotation	$K_2 = 267.3$	
Experiment	Counter-clockwise rotation	$K_1 = 310.1$	1.6
Simulation	Counter-clockwise rotation	$K_2 = 491.3$	

It can be seen that although the simulation drilling resistance was generally larger than the experimental drilling resistance, the changing trend of drilling resistance was the same under different drilling depths, different rotational directions, and different rotational speeds. Therefore, the variation rule of drilling resistance in the process of bit anchor cable drilling was adequately explained through DEM-MBD co-simulation.

Fig. 11 is a motion vector diagram of gravel particles around the anchor cable under different rotational directions when the drilling depth reached 0.4 m. It can be clearly seen that when the rotational direction of the anchor cable was clockwise, the rotation of the anchor cable would give an oblique upward thrust to the surrounding particles. When the

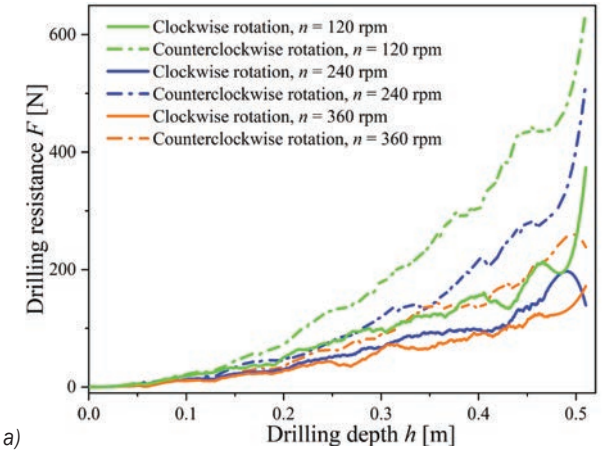

a)

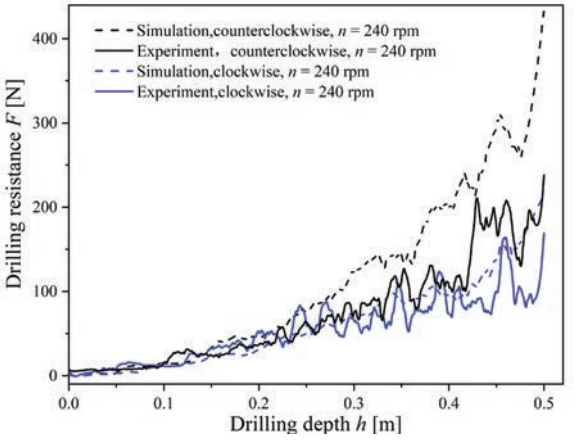

b)

Fig. 10. *Drilling resistance simulation curve; a) different rotational directions and rotational speeds, and b) Comparison of simulation and experiment*

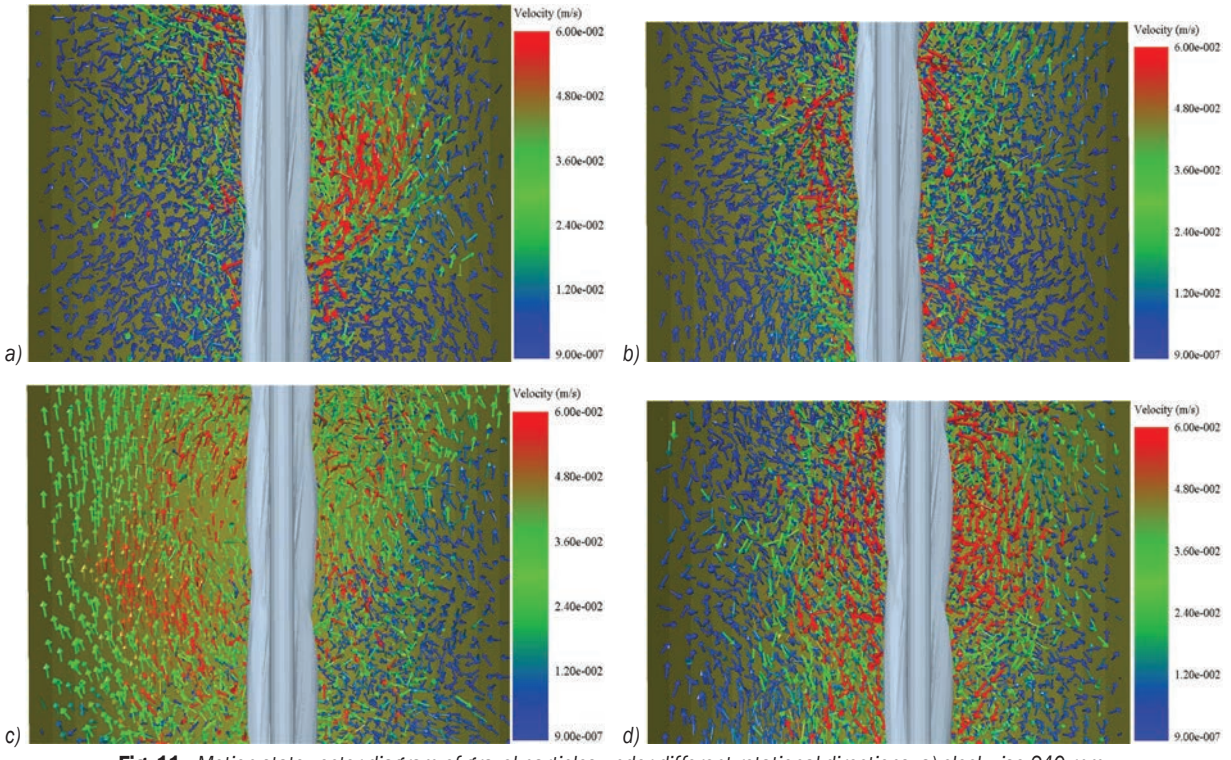

Fig. 11. *Motion state vector diagram of gravel particles under different rotational directions; a) clockwise 240 rpm, b) counter-clockwise 240 rpm, c) clockwise 360 rpm, and d) counter-clockwise 360 rpm*

rotational direction of the anchor cable was counter-clockwise, the rotation of the anchor cable would give an oblique downward thrust to the surrounding particles.

When the anchor cable gave the gravel particles an oblique upward thrust, the anchor cable was subjected to the oblique downward reaction force of the gravel particles, so the drilling resistance of the bit anchor cable was reduced. When the anchor cable gave the gravel particles an oblique downward thrust, the anchor cable was subjected to the oblique upward reaction force of the gravel particles, so the drilling resistance of the bit anchor cable was increased.

From the above results, it can be seen that clockwise rotation of the bit anchor cable could greatly reduce the drilling resistance and hindering torque during drilling compared to counter-clockwise rotation of the bit anchor cable. Therefore, in the following experiments, the rotational direction of the bit anchor cable was clockwise.

2.2.2 Rotational Speed

Fig. 8 shows that with increasing drilling depth, the drilling resistance and hindering torque of the bit anchor cable increased slowly at first and then rapidly. The drilling resistance and hindering torque of the bit anchor cable were inversely proportional to the rotational speed. It can be seen from Fig. 9 that the average drilling resistance and the average hindering torque of the bit anchor cable at the clockwise rotational speed of 300 rpm were 62.7 % and 43.1 % lower than those at the clockwise rotational speed of 120 rpm.

Figs. 11a and c show that with increasing rotational speed, the number and velocity of particles moving upward gradually increased so that the downward thrust of particles to the anchor cable spiral structure gradually increased. Therefore, the drilling resistance of the bit anchor cable in Fig. 8a gradually decreased with increasing rotational speed.

When the bit anchor cable was drilled to the bottom hole at a forward speed of 0.02 m/s, the velocity vector of gravel sediment was shown in Fig. 12. With the increase in the rotational speed of the bit anchor cable, the particle movement of the gravel in the bottom hole became increasingly intense. When the rotational speed reached 240 rpm and 360 rpm, the particles with velocities greater than 0.024 m/s presented an obvious spiral distribution, and their rotational direction was consistent with the rotational direction of the bit anchor cable.

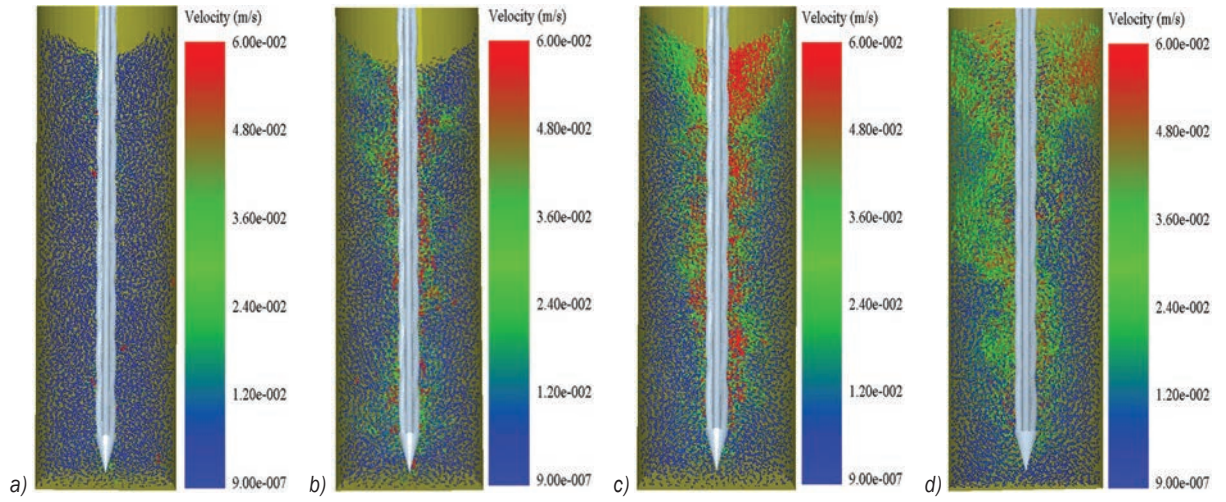

Fig. 12. *Velocity vector diagram of gravel in the bottom hole at different rotational speeds; a) n = 0 rpm, b) n = 120 rpm, c) n = 240 rpm, and d) n = 360 rpm*

Therefore, when the bit anchor cable rotated in the gravel sediments of the bottom hole, the bit anchor cable could stir the gravels, and the faster the rotational speed was, the more obvious the stirring effect. The stirring effect of the bit anchor cable on gravel particles can reduce the drilling resistance in the process of bit anchor cable drilling and allow for uniform mixing of the anchoring agent in the gravel sediments of the bottom hole in the later stage.

2.3 Influence of Particle Moisture on the Dynamic Characteristics of Bit Anchor Cable Drilling

2.3.1 Moist Particles

In the actual installation process of the anchor cable, the gravel in the hole was not completely dry, so to make the experimental environment closer to the real working conditions, drilling experiments were carried out on gravel particles with different moisture contents. The forward speed of the bit anchor cable was 0.025 m/s, and the gravel state was 3 mm to 6 mm particle after 12 h immersion. After Savitzky-Golay smoothing, the drilling resistance and hindering torque of the bit anchor cable when drilling in moist gravel particles were found, and the values are shown in Fig. 13.

Fig. 13 shows that, at the same rotational speed, the drilling resistance and hindering torque of the bit anchor cable when drilling in moist gravel particles were smaller than the values obtained when drilling in dry gravel particles. The reason for this phenomenon was related to the water molecules on the surface of the gravel particles. When the gravel particles were moist,

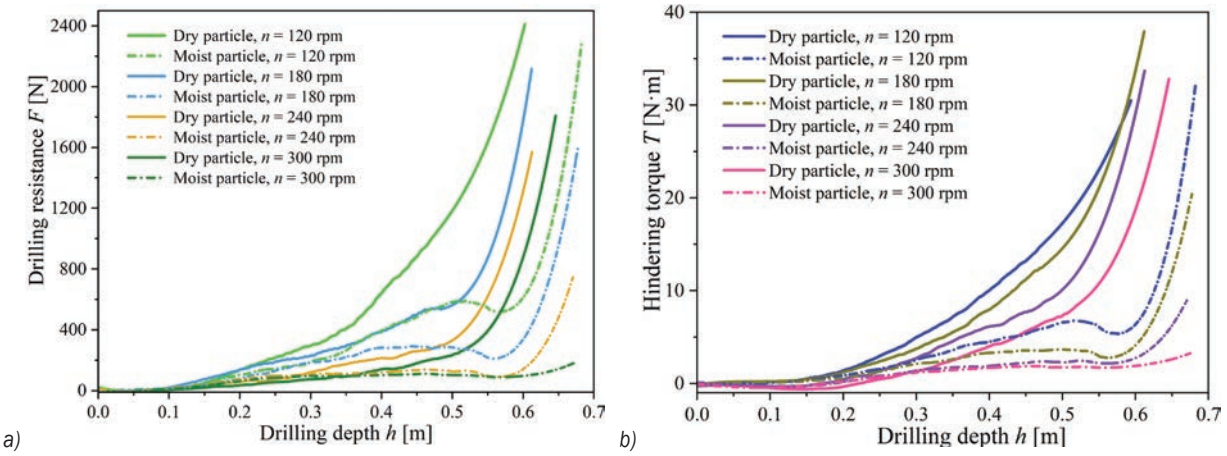

Fig. 13. *Dynamic characteristic curve of moist gravel drilling; a) drilling resistance; b) hindering torque*

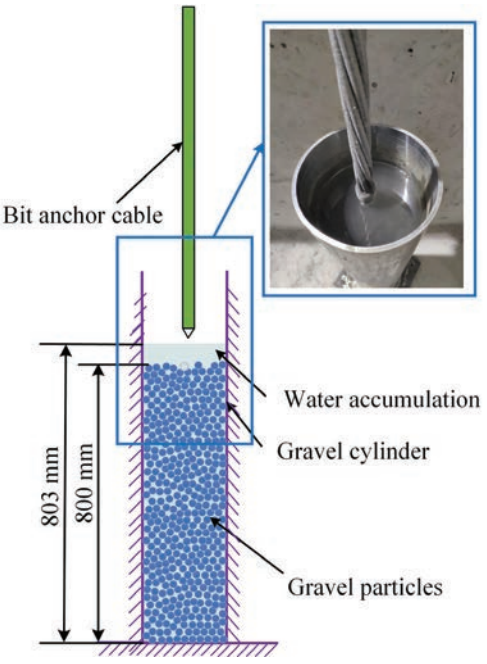

Fig. 14. *Drilling in soaked particles*

a large number of water molecules were attached to the surface of the gravel particles, and then water film formed on the surface of the gravel particles, which reduced their surface friction coefficient. Thus, the drilling resistance and hindering torque of the bit anchor cable were reduced.

Fig. 13b shows that the hindering torque of the bit anchor cable drilling at 120 rpm in moist gravel particles was lower than that of drilling at 300 rpm in dry gravel particles. Therefore, in practical work, we can reduce the difficulty of bit anchor cable installation by improving the humidity of the gravel sediment, and the effect is more obvious than increasing the rotational speed of the bit anchor cable.

2.3.2 Soaked Particles

To further explore the influence of particle humidity on the dynamic characteristics of bit anchor cable drilling, gravel drilling was carried out on gravel particles completely soaked in water. Fig. 14 shows the drilling experiment diagram of soaked particles. The diameters of the gravel particles were between 6 mm to 9 mm, and the forward speed of the bit anchor cable was 0.025 m/s. The drilling resistance and hindering torque of the bit anchor cable are shown in Fig. 15.

Fig. 15 shows that when the rotational speed was the same, the drilling resistance and hindering torque of the bit anchor cable when drilling in soaked particles were greater than those values found when drilling in dry gravel particles. When the particle diameters were 6 mm to 9 mm, the drilling resistance of the bit anchor cable when drilling in soaked particles at 300 rpm was higher than the drilling resistance obtained when drilling in dry particles at 120 rpm, which is substantially different from the trend found when drilling in moist gravel particles.

The reason for the above phenomenon relates to the amount of water in the hole. When there was less water in the hole, the friction coefficient between the gravel particles could be reduced by water attaching to the surface of the particles, and then the drilling resistance and hindering torque of the bit anchor cable could be reduced. However, when there was too much water in the hole, the excessive water hindered the movement of gravel particles and increased the drilling resistance and hindering torque of the bit

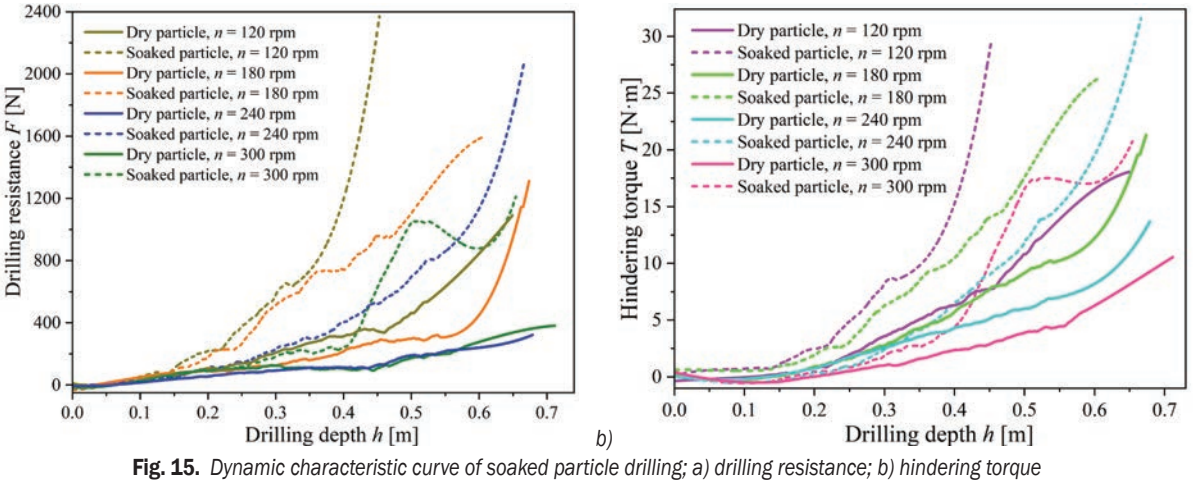

a) b)

Fig. 15. *Dynamic characteristic curve of soaked particle drilling; a) drilling resistance; b) hindering torque*

anchor cable. Therefore, excessive water in the hole should be avoided during bit anchor cable drilling; otherwise, the drilling resistance and hindering torque of the bit anchor cable will be significantly increased.

Fig. 15 shows that when the bit anchor cable was drilled in the soaked particles at a rotational speed of 300 rpm and the drilling depth reached 0.5 m, the drilling resistance and hindering torque of the bit anchor cable increased significantly. The drilling resistance was 446 % and the hindering torque was 400 % of 0.4 m. When the bit anchor cable was drilled, the stable structure of the gravel particles was constantly rebuilt and broken. Drilling depths of 0.4 m to 0.6 m fully reflected the process. When the drilling depth was 0.4 m to 0.5 m, the stability of the whole particle begins to reorganize, and when the drilling depth reached 0.5 m, the whole particle reached a stable state. 0.5 m to 0.6 m was a process in which the stable state of particles was gradually broken. In this process, the sound of friction between bit anchor cable and gravel was very obvious.

2.4 Influence of Particle Type on the Dynamic Characteristics of Bit Anchor Cable Drilling

2.4.1 Particle Diameter

Due to the different rock strata, the types of gravel sediment in different areas are also quite different. As shown in Fig. 16, different types of gravel particles in different areas were collected, with gravel diameters of 3 mm to 6 mm, 6 mm to 9 mm, and 10 mm to 13 mm. Then, the bit anchor cable was used to drill different types of gravel particles at a forward speed of 0.025 m/s. The influence of the particle diameter on the drilling resistance and hindering torque of the bit anchor cable is shown in Fig. 17. The diameter of the gravel cylinder was 160 mm.

Fig. 16. *Gravel particles of different diameters*

Fig. 17 shows that at the same rotational speed, with increasing gravel diameter, the drilling resistance and hindering torque of the bit anchor cable gradually decreased, and when the gravel diameter changed from 3 mm to 6 mm to 6 mm to 9 mm, the reduction in the drilling resistance and hindering torque of the bit anchor cable was much higher than that when the gravel diameter changed from 6 mm to 9 mm to 10 mm to 13 mm. The relationship between the diameter of gravel particles and the drilling resistance and hindering torque of the bit anchor cable was not a simple linear inverse ratio. Therefore, in real-world scenarios, when the diameter of the gravel in the hole is small, it is necessary to further improve the rotational speed of the bit anchor cable to ensure the same drilling efficiency.

2.4.2 Particle Shape

The gravel sediment in the bottom hole is not only different in diameter but also in shape. To explore the influence of particle shape on the dynamic characteristics of bit anchor cable drilling, drilling

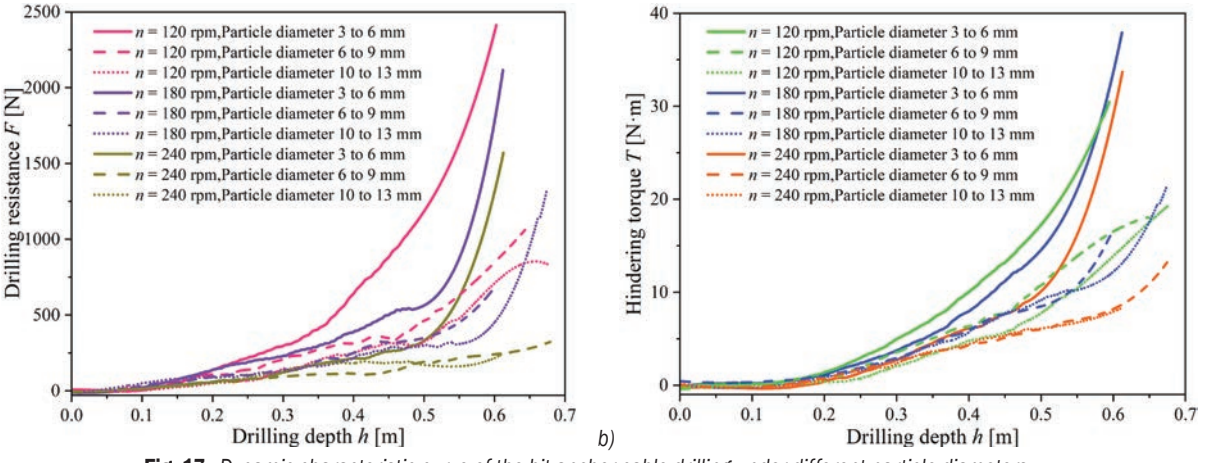

Fig. 17. *Dynamic characteristic curve of the bit anchor cable drilling under different particle diameters; a) drilling resistance, and b) hindering torque*

experiments were carried out on the particles in Fig. 18 at a forward speed of 0.025 m/s. The experimental results following Savitzky-Golay smoothing are shown in Fig. 19.

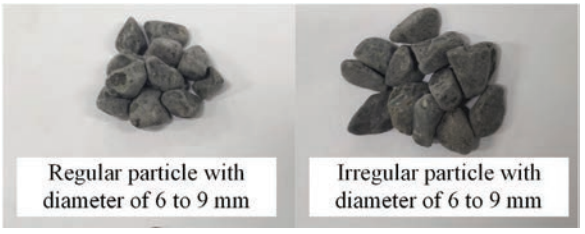

Fig. 18. *Gravel particles of different shapes*

Fig. 19 shows that under the same rotational speed, the drilling resistance and hindering torque of the bit anchor cable when drilling in regular gravels were less than those when drilling in irregular gravels. When the shape of the particle was more regular, the rolling friction coefficient of the particle was smaller. In the same external environment, its motion state was easier to change, and it was easier to roll. Therefore, when the bit anchor cable was drilling in regular particles, the number of particles with rolling friction between the particles and the bit anchor cable was greater, and the number of particles with sliding friction was lower. As a result, drilling in regular particles was less difficult than drilling in irregular particles.

At the same time, the influence of the particle shape on the drilling resistance and hindering torque of the bit anchor cable decreased gradually with increasing rotational speed. Therefore, when the particle shape in the hole is irregular, the influence of particle shape on bit anchor cable drilling can be reduced by increasing the rotational speed of the bit anchor cable.

3 CONCLUSIONS

In view of the difficulty of anchor cable installation caused by the accumulation of gravel sediment in the bottom hole, the auxiliary installation equipment for an anchor cable was designed. Moreover, a new anchor cable installation method was proposed, which works by installing a drill bit in front of the anchor cable so that the drill bit could assist anchor-cable drilling. The feasibility of this method was explored with an anchor cable drilling test bed. At the same time, the drilling process of the bit anchor cable in the gravel sediments in a bottom hole was simulated by DEM-MBD co-simulation. The main conclusions were as follows:

1. When the anchor cable was drilled clockwise without the bit, the drilling depth was only 0.25 m. When the bit was installed in front of the anchor cable, the drilling depth was 0.6 m. Installing a bit in front of the anchor cable could significantly reduce the drilling resistance and hindering torque during anchor cable drilling. Clockwise drilling of the bit anchor cable was more beneficial to anchor cable installation than counter-clockwise drilling. The drilling resistance and hindering torque of the bit anchor cable were inversely proportional to its rotational speed. The stirring effect of bit anchor cable drilling on gravel particles provides the possibility of uniform mixing of the anchor agent in the gravel sediments in a bottom hole.

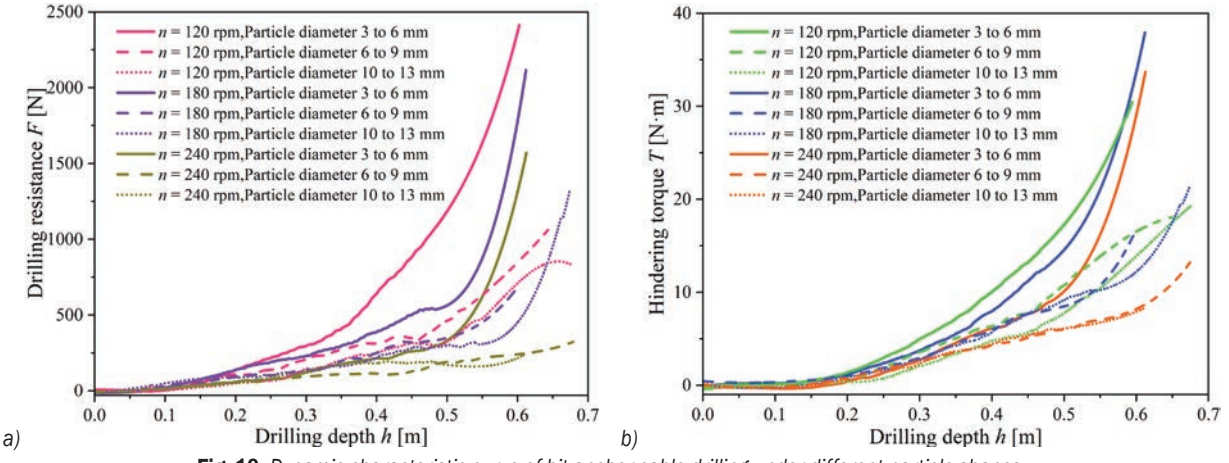

Fig. 19. *Dynamic characteristic curve of bit anchor cable drilling under different particle shapes; a) drilling resistance, and b) hindering torque*

2. The drilling resistance and hindering torque of the bit anchor cable were the largest when drilling in soaked particles, followed by drilling in dry particles, and the smallest when drilling in moist particles. Therefore, during the installation of the bit anchor cable, the gravel should be kept moist as much as possible, but excessive water in the hole should be avoided. When the stable structure of gravel particles was broken or re-established, the drilling resistance and hindering torque of bit anchor cable could change greatly. When the bit anchor cable was drilled at 300 rpm in the soaked particles, the drilling resistance and hindering torque at 0.5 m were 446 % and 400 % of those at 0.4 m, respectively.
3. The drilling resistance and hindering torque of the bit anchor cable were inversely proportional to the diameter of the gravel particles. In the experiment, the best drilling effect was achieved when the diameter of gravel particle was 10 mm to 13 mm. Compared with drilling in irregular gravels, drilling in regular gravels could make the bit anchor cable have less drilling resistance and hindering torque. The influence of particle shape on bit anchor cable drilling decreased with increasing rotational speed. Therefore, when the gravel diameter is small and the shape is irregular, it is necessary to further improve the rotational speed of the bit anchor cable to ensure the same installation efficiency.

4 ACKNOWLEDGEMENTS

The project was supported by the National Natural Science Foundation of China (Grant No.52174146) and the Project of Shandong Province Higher Educational Young Innovative Talent Introduction and Cultivation Team (Performance enhancement of deep coal mining equipment).

5 REFERENCES

[1] Hao, W., Tao, D. (2019). Research on Deformation Control Technology of Broken Soft Rock Pre-mining Roadway. IOP Conference Series: Earth and Environmental Science, vol. 358, no. 4, 042047, **DOI:10.1088/1755-131 5/358/4/042047**.

[2] Sun, Y., Li, G., Zhang, J., Xu, J. (2020). Failure mechanisms of rheological coal roadway. *Engineering Failure Analysis*, vol. 12, no. 7, 2885, **DOI:1 0.3390/su12072885**.

[3] Gao, Y., Wang, C., Liu, Y., Wang, Y., Han, L. (2021). Deformation mechanism and surrounding rock control in high-stress soft rock roadway: A case study. *Advances in Civil Engineering*, vol. 2021, 9950391, **DOI:10.1155/2021/9950391**.

[4] Xu, Y., Pan, K., Zhang, H. (2019). Investigation of key techniques on floor roadway support under the impacts of superimposed mining: theoretical analysis and field study. *Environmental Earth Sciences*, vol. 78, no. 15, 436, **DOI:10.1007/s12665-019-8431-9**.

[5] Du, M., Wang, X., Zhang, Y., Li, L., Zhang, P. (2020). In-situ monitoring and analysis of tunnel floor heave process. *Engineering Failure Analysis*, vol. 109, no. 9, 104323, **DOI:10.1016/j.engfailanal.2019.104323**.

[6] Lai, X., Xu, H., Shan, P., Wang, Y., Zeyand, Wu, X. (2020). Research on mechanism and control of floor heave of mining-influenced roadway in top coal caving working face. *Energies*, **DOI:10.3390/en13020381**.

[7] Wu, G., Yu, W., Zhang, J., Ning, Y. (2017). Control mechanism and support technology of soft coal roadway in the fully mechanized mining work face. *Geo-Resources Environment and Engineering*, vol. 2, p. 211-217, **DOI:10.15273/gree.2017.02.038**.

[8] Zhao, C.X., Li, Y.M., Liu, G., Meng, X. (2017). Mechanism analysis and control technology of surrounding rock failure in deep soft rock roadway. *Engineering Failure Analysis*, vol. 115, 104611, **DOI:10.1016/j.engfailanal.2020.104611**.

[9] Shi, L., Zhang, H., Wang, P. (2020). Research on key technologies of floor heave control in soft rock roadway. *Advances in Civil Engineering*, vol. 2020, 8857873, **DOI:10.1155/2020/8857873**.

[10] Lin, F., Mengjun, W., Guangdi, W., Peng, C. (2016). Comparative analysis on stress state of submerged floating tunnels in different anchor cable arrangement modes. *Procedia Engineering*, vol. 166, p. 279-287, **DOI:10.1016/j.proeng.2016.11.550**.

[11] Li, J., Li, L. (2016). Numerical analysis on a new pressure-type anchor cable with precast anchor head based on FLAC3d. *ICENCE*, p. 237-241, **DOI:10.2991/icence-16.2016.51**.

[12] Tao, Z., Zhu, Z., Han. W., Zhu, C., Liu, W., Zheng, X., Yin, X., He, M. (2018). Static tension test and the finite element analysis of constant resistance and large deformation anchor cable. *Advances in Mechanical Engineering*, vol. 10, no. 12, p. 1-13, **DOI:10.1177/1687814018810638**.

[13] Shi, K., Wu, X., Liu, Z., Dai, S. (2019). Coupled calculation model for anchoring force loss in a slope reinforced by a frame beam and anchor cables. *Engineering Geology*, vol. 260, 105245, **DOI:10.1016/j.enggeo.2019.105245**.

[14] Shi, K., Wu, X., Tian, Y., Xie, X. (2021). Analysis of re-tensioning time of anchor cable based on new prestress loss model. *Mathematics*, vol. 9, no. 10, 1094, **DOI:10.3390/math9101094**.

[15] Yang, Z., Li, S., Yu, Y., Liu, X., Hu, Y. (2020). Study on the variation characteristics of the anchor cable prestress based on field monitoring in a foundation pit. *Arabian Journal of Geosciences*, vol. 13, no. 23, **DOI:10.1007/s12517-020-06264-z**.

[16] Wang, S.R., Wang, Z.L., Chen, Y.B., Wang, Y.H., Huang, Q.X. (2020). Mechanical performances analysis of tension-torsion coupling anchor cable. *International Journal of Simulation Modelling*, vol. 19, no. 2, p. 231-242, **DOI:10.2507/IJSIMM19-2-512**.

[17] Sun, H.G., Li, G., Chen, G. (2021). Dynamic model of cable tension and configuration for vessel at anchor. *Journal of Marine Science and Technology*, vol. 26, no. 4, p. 1144-1152, **DOI:10. 1007/s00773-021-00802-4**.

[18] Kim, Y.-M. (2008). A granular motion simulation by discrete element method. *Journal of Mechanical Science and Technology*, vol. 22, no. 4, p. 812-818, **DOI:10.1007/s12206-008-0112-7**.

[19] Siegmann, E., Jajcevic, D., Radeke, C., Strube, D., Friedrich, K., Khinast, J.G. (2017). Efficient discrete element method simulation strategy for analyzing large-scale agitated powder mixers. *Chemie Ingenieur Technik*, vol. 89, no. 8, p. 995-1005, **DOI:10.1002/cite.201700004**.

[20] Mitsufuji, K., Nambu, M., Hirata, K., Miyasaka, F. (2018). Numerical method for the ferromagnetic granules utilizing discrete element method and method of moments. *IEEE Transactions on Magnetics*, vol. 54, no. 3, p. 3-6, **DOI:10.1109/TMAG.2017.2758799**.

[21] Lee, Y.S., Nandwana, P., Zhang, W. (2018). Dynamic simulation of powder packing structure for powder bed additive manufacturing. *International Journal of Advanced Manufacturing Technology*, vol. 96, no. 1-4, p. 1507-520, **DOI:10.1007/s00170-018-1697-3**.

[22] Wang, X., Li, B., Yang, Z. (2018). Analysis of the bulk coal transport state of a scraper conveyor using the discrete element method. *Strojniški vestnik - Journal of Mechanical Engineering*, vol. 64, no. 1, p. 37-46, **DOI:10.5545/sv-jme.2017.4790**.

[23] Yan, H., Li, Y., Yuan, F., Peng, F., Yang, X., H., X. (2020). Analysis of the Screening Accuracy of a Linear vibrating screen with a multi-layer screen mesh. *Strojniški vestnik - Journal of Mechanical Engineering*, vol. 66, no. 5, p. 289-299. **DOI:10554/sv-jme.2019.6523**.

[24] Wang, Z., Li, B., Liang, C., Wang, X., Li, J. (2021). Response analysis of a scraper conveyor under chain faults based on MBD-DEM-FEM. *Strojniški vestnik - Journal of Mechanical Engineering*, vol. 67, no. 10, p. 501-515, **DOI:10.5545/sv-jme.2021.7300**.

[25] Yang, Z., Sun, X.X., Meng, W.J. (2021). Research on the axial velocity of the raw coal particles in vertical screw conveyor by using the discrete element method. *Journal of Mechanical Science and Technology*, vol. 35, p. 2551-2560, **DOI:10.1007/s12206-021-0526-z**.

[26] Liu, H., Zhang, S.-H., Ding, Y.-P., Shi, G.-L., Geng, Z. (2021). A simplified formulation for predicting wrinkling of thin-wall elbow tube in granular media-based push-bending process. *International Journal of Advanced Manufacturing Technology*, vol. 115, p. 541-549, **DOI:10.1007/s00170-021-07168-2**.

[27] Gao, K., Liu, J., Wu, T., Zeng, Q., Sun, L., Zhang, X. (2022). Drilling study of bit in gravel environment based on DEM-MBD. *Engineering Reports*, vol. 4, no. 4, p. 1-21, **DOI:10.1002/eng2.12472**.

[28] Shi, S., Gao, L., Xiao, H., Xu, Y., Yin, H. (2021). Research on ballast breakage under tamping operation based on DEM-MBD coupling approach. *Construction and Building Materials*, vol. 272, 121810, **DOI:10.1016/j.conbuildmat.2020.121810**.

[29] Chen, Z., Xue, D., Wang, G., Cui, D., Fang, Y., Wang, S. (2021). Simulation and optimization of the tracked chassis performance of electric shovel based on DEM-MBD. *Powder Technology*, vol. 390, p. 428-441, **DOI:10.1016/j.powtec.2021.05.085**.

Strojniški vestnik - Journal of Mechanical Engineering 69(2023)1-2, 17-31
DOI:10.5545/sv-jme.2022.427
Original Scientific Paper
Received for review: 2022-10-27
Received revised form: 2022-12-30
Accepted for publication: 2023-01-09

Analysis of the Dynamic Characteristics of a Gear-Rotor-Bearing System with External Excitation

Risu Na – Kaifa Jia* – Shujing Miao – Weiguo Zhang – Quan Zhang
Inner Mongolia University of Technology, College of Mechanical Engineering, China

The dynamic response of the rotor system in a ring die granulator is complex and difficult to solve when it operates under joint external, support and gear mesh forces. To solve this problem, a finite element method and extrusion theory was applied in this study to develop a dynamic coupling model for a hollow overhung rotor with external load excitation. A Newmark-β numerical integration method was used to solve for the dynamic response of the overhung rotor under multiple excitation forces. The results included time-domain response diagrams, frequency-domain response diagrams, phase diagrams, Poincaré section diagrams, and bifurcation diagrams. The model and the method were verified by testing a ring die granulator. On this basis, the dynamic response of the system is predicted according to the influence of different parameters. As the bearing support distance increased, the roller eccentricity decreased, the bearing clearance decreased, the response of the rotor system was significantly optimized, and the system tended to stabilize gradually. Therefore, this paper provides a theoretical basis and experimental verification for the optimization of a pelleting machine transmission structure.
Keywords: rotor dynamics, external incentives, finite element method, bearing, gear

Highlights
- *Bearing clearance will affect the internal excitation of the bearing support of the system, so the influence law of different clearance parameters on the system is discussed.*
- *The clearance of a helical gear can affect the internal excitation of the system-bearing support, so the influence law of different clearance parameters on the system is discussed.*
- *Bearing support distance will affect the dynamic response of the system, so the influence law of different support distance parameters on the system is discussed.*
- *The external load model of a ring mold pelleting machine is established, and its dynamic characteristics are explored according to the important parameters of production and operation.*
- *The accuracy and correctness of the theoretical calculation are verified with experiments.*

0 INTRODUCTION

Ring die granulators are key components used in the granulation processing. They are not only used in the feed-processing industry but are also widely used in emerging biomass pellet fuel molding industries. The dynamic response of the rotor is complex, making it difficult to calculate and predict. The rotor system in a ring die granulator is prone to rotor instability due to the combination of the gear mesh force, the bearing support force, and the external load force. However, studies regarding the responses of rotor systems experiencing random extrusion external loads are rarely reported. To improve the stability of this type of rotor and the service life of its key components, the dynamic response of a hollow overhung rotor experiencing multiple external forces was investigated in this study, and the effect patterns of the key parameters were explored.

Schwarz et al. [1] and other research groups [2] to [3] used dynamic simulations and machine learning algorithms to study the impact of highly dynamic cage motion on the performance of rolling bearings. Smagala and Kecik [4] and Kurvinen et al. [5] used a two-degree-of-freedom nonlinear bearing model and the Hertz theory to study the effects of the number of balls and the rotational speed of the rotating axle on the dynamic response. Many scholars [6] to [9] have carried out extensive research on bearing failure dynamics and other aspects, and the results provide help for the ontology.

Chen et al. [10] proposed a dynamic model of spur gear with straight teeth, which takes into account the detailed deformation of a single tooth, including the flexible deformation of the tooth surface, the deformation of the tooth body, the contact deflection of the local tooth surface and the deformation due to its neighbouring loaded teeth. Zheng et al. [11] and Zhu et al. [12] focused on the centrifugal force in high-speed working conditions, developed an analytical finite element method (FEM) framework to integrate the centrifugal field into the mesh stiffness and nonlinear dynamics. Shi and Li [13] proposed a dynamics model for hypoid gears, considering mesh stiffness that is dependent on dynamic mesh force. Based on the spectral density of excitation and the frequency response function of the transfer path between the excitation point and measurement point, Hajnayeb

*Corr. Author's Address: Inner Mongolia University of Technology, College of Mechanical Engineering, China, 1642523516@qq.com

and Sun [14] proposed a new method to determine the influence of random manufacturing errors on vibration measurement on mating gear bearings. In the work of Liu et al. [15], mesh characteristics of the spur gear paired with the pitch deviation are studied in order to analyse the time-varying contact ratio and motion characteristics of the system. Xu et al. [16] used a loaded tooth contact analysis method and conducted quasi-static experiments to determine the coefficient matrix describing the relationship between the mesh force and the strain. Cirelli et al. [17] and [18] proposed an improved method to simulate the nonlinear dynamic response of spur gears. Mo et al. [19] and [20] discussed the effects of flexible support stiffness and floating components on the stability and reliability of a herringbone planetary gear system. Other researchers proposed a variety of accurate and effective time-varying mesh stiffness calculation methods, including the potential energy method, and discussed the effects of temperature and shock on the mesh stiffness [21] to [23]. In comparison, the calculation model of gear meshing stiffness and meshing error based on Fourier series is more widely used because of its representativeness.

Other researchers [24] to [27] proposed a Timoshenko beam consisting of a chain of masses and straight segments, accounting for the bending and shear deformations of the linear rotational and transverse springs. Zhan et al. [28] and Si et al. [29] studied the free vibrations of axially-loaded multi-cracked Timoshenko beams with different boundary conditions, such as hinged, cramped, clamped-hinged, and cramped-free. Based on the Timoshenko beam theory and using Hamilton's principle and Euler angles, Zhu et al. [30] and Zhang et al. [31] developed a novel mathematical model for a rotating axle with an efficient centrifugal term. The solution of rotor dynamic response based on discrete elements can not only deal with the influence of complex excitations but also has s high solving accuracy.

An extrusion mechanics model for a ring die was constructed as a function of vibration. Using a nonlinear deep groove ball bearing support mechanics model and a helical gear mesh mechanics model, the dynamic characteristics of the overhung rotor of a ring die granulator were analysed and used as a case study. The accuracy and validity of the theoretical model for coupled rotor dynamics were verified with experiments. This method takes into account the effects of complex load coupling and can provide guidance for solving and optimizing the dynamic response of irregular rotors.

1 COUPLED ROTOR MODEL WITH EXTERNAL EXCITATION

A ring die granulator rotor system consists of a hollow axle, a ring die, a gear, and a bearing, as shown in Fig. 1. Rotor vibration is an important cause of declining granulation efficiency and granulation quality. Multiple acting forces are significant factors affecting the stability of the rotor system. To improve the calculation efficiency and accuracy, the hoop-locking connection between the ring die and the hollow axle was simplified as a rigid connection, with the assumption that the material of the rotating axle was uniform, and the keyway and the chamfering effects were negligible. A system dynamics model was developed using the Timoshenko finite element analysis method and the lumped mass method. The differential principle was used to discretize the variable-segment rotor and to divide the rotor system into 20 axle segments and 21 nodes as shown in Fig. 2.

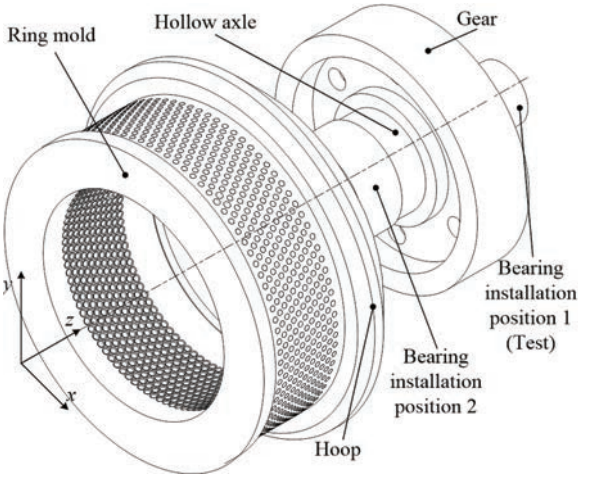

Fig. 1. *Drive rotor system of ring mold granulator*

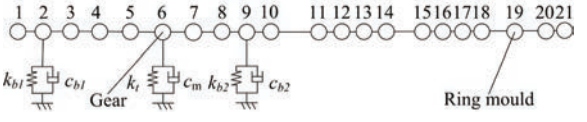

Fig. 2. *Finite element model of ring mold granulator rotor*

According to the rotor structure of the ring die granulator, the finite element rotor model with the radial translational displacement and bending displacement vectors contained displacement vectors for a total of 84 element nodes. The element displacement vector for each axle segment could be expressed by Eq. (1). The supporting forces for the left and right bearings, the mesh force of the helical gear, and the pressing force of the ring die acted

on the second, ninth, sixth, and nineteenth nodes, respectively.

$$\mathbf{u}_{si} = \left[x_A, y_A, \theta_{xA}, \theta_{yA}, x_B, y_B, \theta_{xB}, \theta_{yB} \right]^T. \quad (1)$$

In Eq. (1), x_A and y_A represent the x and y radial vibration displacements of the centre at the left end face, A, of the axle segment, respectively. θ_{xA} and θ_{yA} represent the radial angular displacements of the centre at the left end face, A, respectively. In a similar way, the displacements of the right end face, B, could be obtained. $\mathbf{u}_{si}$ represents the i^{th} element displacement vector of the rotor. The mass matrix, $\mathbf{M}_{si}$, the stiffness matrix, $\mathbf{K}_{si}$, the gyro matrix, $\mathbf{G}_{si}$, and the external force matrix, $\mathbf{F}_{si}$, could be obtained for the i^{th} element. The element matrices were assembled as shown in Fig. 3, and the rotor system's global mass matrix, **M**, global stiffness matrix, **K**, global gyro matrix, **G**, and global external force matrix, **F**, were obtained.

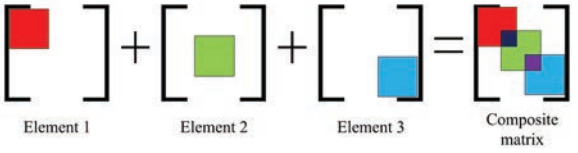

Fig. 3. *Timoshenko beam element matrix assembly*

By using Rayleigh damping to calculate the rotor viscous damping, matrix **C** could be expressed by Eq. (2):

$$\mathbf{C} = \alpha_o \mathbf{M} + \beta_o \mathbf{K}, \quad (2)$$

where α_o and β_o are the proportional Rayleigh damping coefficients. The nodal displacement vector of the rotor system can be expressed by $\mathbf{X} = [x_1\ x_2 \cdots x_{84}]$.

According to the energy method, the dynamic equation for the overhung hollow rotor with multi-force coupling in the ring die granulator was established as Eq. (3):

$$\mathbf{M}\ddot{\mathbf{X}} + (\mathbf{C} + \omega\mathbf{G})\dot{\mathbf{X}} + \mathbf{K}\mathbf{X} = \mathbf{Q}. \quad (3)$$

In Eq. (3), **Q** represents the assembled external force matrix for the coupled rotor system, which includes the gear mesh force matrix, $\mathbf{F}_g$, the bearing support force matrix, $\mathbf{F}_b$, the ring die extrusion force matrix, $\mathbf{F}_h$, and the axle external force matrix, **F**, $\ddot{\mathbf{X}}$, $\dot{\mathbf{X}}$, and **X** are the acceleration, velocity, and displacement vectors of the rotor system, respectively, and ω is the rotational angular velocity of the rotor.

The structural parameters of the hollow axle of the SZLH420 ring die granulator are listed in Table 1. The elastic modulus, E, was 210 GPa, the material density, ρ, was 7,850 kg/m^3, the Poisson's ratio, λ, was 0.3, α_o and β_o were both 0.05, and the axle rotational speed, n, was 300 r/min.

Table 1. *Structural parameters of the beam*

Element number	Outer diameter [mm]	Inner diameter [mm]	Length of element [mm]
1	120	80	45
2	120	80	45
3	150	80	45
4	150	80	45
5	150	80	45
6	150	80	45
7	190	80	60
8	200	80	50
9	200	80	50
10	230	80	110
11	560	210	10
12	600	240	10
13	640	300	10
14	680	420	20
15	666	420	8
16	652	420	8
17	640	420	8
18	580	420	85
19	580	420	85
20	600	420	30

2 MECHANICAL MODEL FOR THE COUPLED SYSTEM

2.1 Mechanical Model for the Deep Groove Ball Bearing Support

Bearings are a critical part of a rotor system, and they support and constrain the axles. The bearing parameters of the models of the two groups of deep groove ball bearings in the ring die granulator, Models 6412 and 6420, are listed in Table 2. The deep groove ball bearings consisted of an inner and an outer ring, balls, and a cage. It was assumed that the contacts between the balls and the inner and outer rings were point contacts, and the effect of centrifugal force during rotation was ignored when calculating the bearing support force. A schematic diagram of one of the deep groove ball bearings is shown in Fig. 4, in which ω_{in} represents the angular velocity of the balls on the inner ring and ω_{cage} is the rotational angular velocity of the cage. The outer ring and frame had an interference fit with a connection speed of zero. Assuming that the balls were evenly distributed in the inner and outer races, the nonlinear restoring forces in

the *x*- and *y*-directions of the deep groove ball bearing could be expressed by Eq. (4):

$$F_{\mathrm{b}}=\begin{cases}F_{\mathrm{b}x}=\sum_{j=1}^{N_{\mathrm{b}}}F_{jx}=\sum_{j=1}^{N_{\mathrm{b}}}F_j\cos\theta_j\\ F_{\mathrm{b}y}=\sum_{j=1}^{N_{\mathrm{b}}}F_{jy}=\sum_{j=1}^{N_{\mathrm{b}}}F_j\sin\theta_j\end{cases}. \quad (4)$$

In Eq. (4), $F_{\mathrm{b}x}$ and $F_{\mathrm{b}y}$ represent the supporting forces in the *x*- and *y*-directions of the bearing, respectively, N_{b} is the number of balls in the deep groove ball bearing, and θ_j is the rotation angle of the j^{th} ball at time *t* and can be expressed by Eqs. (5) and (6):

$$\theta_j=\omega_{\mathrm{cage}}\times t+\frac{2\pi}{N_{\mathrm{b}}}(j-1)\quad j=1,2,\cdots,N_{\mathrm{b}}, \quad (5)$$

$$\omega_{\mathrm{cage}}=\frac{\omega_{\mathrm{in}}\times r}{R_{\mathrm{b}}+r}. \quad (6)$$

In Eqs. (5) and (6) R_{b} is the inner radius of the outer ring of the bearing and *r* is the outer radius of the inner ring of the bearing. The contact deformations between the balls and the inner and outer rings in the deep groove ball bearing satisfy the Hertz contact theory. Therefore, the contact extrusion force, F_j, generated by the j^{th} ball on the race could be expressed by Eq. (7):

$$F_j=C_{\mathrm{b}}\times\delta_j^{3/2}\times H(\delta_j), \quad (7)$$

where C_{b} represents the Hertzian contact stiffness related to the material properties and δ_j represents the normal contact deformation between the j^{th} ball and the races. The interaction between the ball and the races can only generate a normal positive pressure. Therefore, a force exists when the normal contact deformation, δ_j, between the ball and the races is greater than zero. To determine the contact between the ball and the races, the Heaviside function was introduced:

$$H(\delta_j)=\begin{cases}1 & \delta_j>0\\ 0 & \delta_j<0\end{cases}. \quad (8)$$

For the bearing clearance, γ_0, and the *x* and *y* radial displacements, the normal contact deformation, δ_j, between the ball and the races could be expressed by Eq. (9):

$$\delta_j=x\cos\theta_j+y\sin\theta_j-\gamma_0. \quad (9)$$

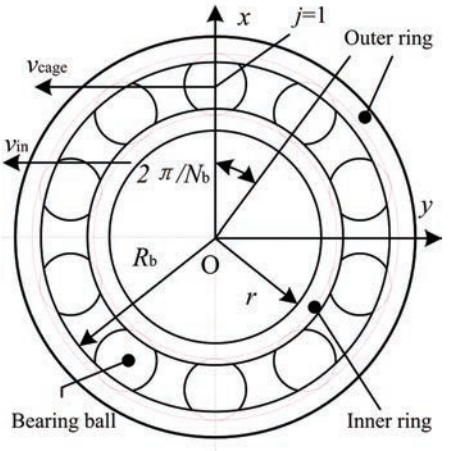

Fig. 4. *Bearing mechanical model*

Table 2. *Structural parameters of the support bearing*

Bearing i	1	2
Outer radius R_{b} [mm]	55.55	79
Inner radius r [mm]	40.65	62.4
Ball number N_{b}	19	25
Contact stiffness C_{b} [GN/m$^{3/2}$]	8.05	
Bearing clearance γ_0 [μm]	10	
Support stiffness k_i [N/m]	7×108	9×108
Brace damping C_i [Ns/m]	500	1000

2.2 Mechanical Model for the Helical Gear Mesh

The gear was treated as a thin hard disk using the lumped mass method. The mechanical model for the gear shown in Fig. 5 was developed by analysing the forces acting on the gear and decomposing them orthogonally. The mass eccentricity caused by the casting error and nonuniform gear material is represented by *e*. The geometric centre of the gear is at O_1 and the centre of mass is at O_g. The gravity of the gear itself is represented by *P*. The centrifugal force of the eccentricity of the gear rotating mass is expressed by F_e=Meω^2. At the beginning of operations, the line O_1O_g was parallel to the *x*-axis. For any *t*, the angle between O_1O_g and the *x*-axis was ωt. Since the meshing stiffness calculation based on the cumulative potential energy method and the meshing error calculation considering gear alignment and modification factors have a wide range of applications and practices **[21]** to **[23]**, the Fourier expansion calculated accordingly is as follows:

$$k(t)=k_{\mathrm{m}}+k_{\mathrm{a}}\sin(\omega t+\varphi), \quad (10)$$

where k_{m} represents the average mesh stiffness, k_{a} is the mesh stiffness variation amplitude, and

φ is the initial phase angle and is equal to 0. The comprehensive transmission error, $e(t)$, affected by the tooth profile and pressure angle errors in an external gear transmission could be expressed by Eq. (11):

$$e(t) = e_{\mathrm{r}} \sin(\omega t + \varphi), \tag{11}$$

where e_{r} is the comprehensive (general) transfer error amplitude. Then, the radial dynamic mesh force of the gear can be defined as the sum of the elastic restoring force and the damping force:

$$F_a = k(t)\, f\left(X(t), \mathrm{b}\right) + c_{\mathrm{m}} \dot{X}(t). \tag{12}$$

In Eq. (12), c_{m} represents the mesh damping and $f(X(t), \mathrm{b})$ is a nonlinear function. Assuming that the driving gear axle was a rigid axle and that its vibration angle displacement was negligible, the displacement function, $X(t)$, of the driven gear axle vibration and mesh error is expressed by Eq. (13):

$$X(t) = y + e(t). \tag{13}$$

The gear transmission had a certain one-sided backlash, b_0. When there were x and y vibration displacements during the gear operation, the corrected backlash, b, could be expressed by Eq. (14):

$$\begin{aligned} b &= b_0 + a_0 \cos\alpha_0 \left(\tan\alpha' - \tan\alpha_0 + \alpha_0 - \alpha'\right), \\ \alpha' &= \arccos\left(a_0 \cos\alpha_0 / a'\right), \\ a' &= \sqrt{\left(a_0 \cos\alpha_0 + x\right)^2 + \left(a_0 \sin\alpha_0 + y\right)^2}. \end{aligned} \tag{14}$$

In Eq. (14), a_0 and α_0 represent the initial centre distance and the pressure angle, respectively, and a' and α' are the centre distance and pressure angle in the actual meshing process, respectively. The nonlinear function in the dynamic mesh force equation could be expressed by Eq. (15):

$$f\left(X(t), b\right) = \begin{cases} X(t) - b & X(t) > b \\ 0 & \left|X(t)\right| \le b \\ X(t) + b & X(t) < -b \end{cases}. \tag{15}$$

The friction force of the tooth surface could be obtained from the dynamic mesh force of the gear meshing. The secondary friction force of the gear can be expressed by Eq. (16):

$$F_f = \lambda \mu F_a, \tag{16}$$

where μ is the static friction coefficient. For mesh points above a node, λ was assigned a value of 1, otherwise, it was assigned a value of 1. The gear forces, F_{gx} and F_{gy}, in the x- and y- directions were obtained from Eq. (17):

$$\begin{aligned} F_{gx} &= \mathrm{M} e \omega^2 \sin(\omega t) + F_f, \\ F_{gy} &= -\mathrm{M} e \omega^2 \cos(\omega t) + F_a - P. \end{aligned} \tag{17}$$

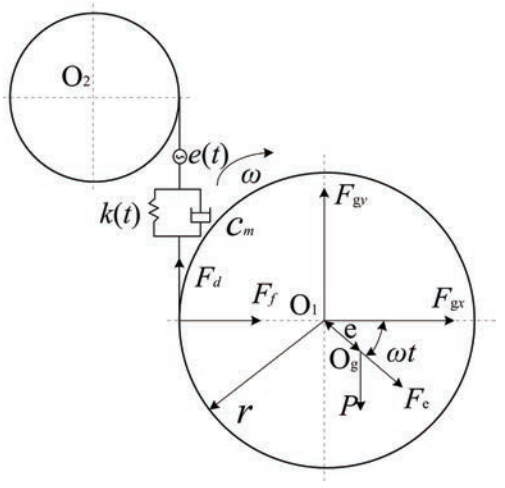

Fig. 5. *Gear mechanical mode*

The mass, M, of the ring die granulator gear was 113 kg, the initial one-sided backlash, b_0, was 10 μm, the static friction coefficient, μ, was 0.3, and the mass eccentricity, e, was 2 mm. The rest of the helical gear parameters are listed in Table 3.

Table 3. *Structure parameters of helical gear*

Gear i	1	2
Number of teeth z_i	23	120
The modulus m_{n} [mm]	4	4
Pressure angle α [°]	20	
Spiral angle β [°]	18	
Tooth width B [mm]	150	
k_{m} [N/m]	6.3×106	
k_{a} [N/m]	3.2×105	
e_{r} [mm]	2.2×10-5	
C_{m} [Nm/s]	117	

2.3 Mechanical Model for External Excitation

The extrusion force is an important cause of the vibration in a ring die granulator rotor. Developing an effective extrusion mechanical model is the key step for accurately analysing the dynamic characteristics of the ring die granulator rotor. As shown in Fig. 6, during relative motion of the ring die and the pressing roller, the material entered the gap between the die roller and the rotation of the ring die and was extruded to reach the extrusion density. The material extrusion area was

divided into a compression area and an extrusion area, which corresponded to the central angles, θ_t and θ_{max}, respectively. The extrusion force on the inner surface of the ring die increased as the extrusion density of the material increased, and it tended to be stable after reaching the extrusion density. The extrusion density of the material was largest at the location where the die-roller gap was a minimum, that is, the extrusion force was largest. Assuming that the frictional force generated by the extrusion of the material restrained the relative sliding between the pressure roller and the ring die, ignoring the rotational inertia force of the material, and treating the ring die and the pressure roller as rigid bodies, the force distribution diagram was obtained for the ring die, as shown in Figure 6. F_{hx} and F_{hy} represent the components of the extrusion force in the *x*- and *y*-directions, respectively, f_x and f_y are the components of the friction force in the *x*- and *y*-directions, respectively, *e* is the distance between the roller and the centre of the ring die, r_h is the inner diameter of the ring die, r_r represents the outer diameter of the roller, *d* is the thickness after compression and extrusion, and *h* is the thickness of the uncompressed material.

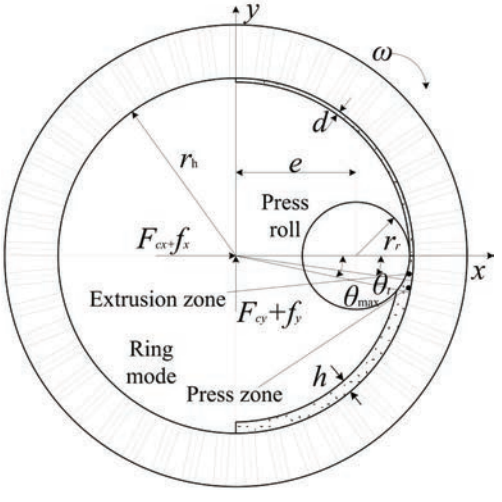

Fig. 6. *Mechanical model of ring mode*

In a ring die granulator, a gap is present between the pressing roller and the ring die to avoid rigid impacts caused by the vibration of the ring die. As the material is squeezed by the pressing roller, plastic deformation occurs in the extrusion area, and the density of the material is inversely proportional to the gap between the die and the roller. Because this gap exists, in addition to the material compressed into the die hole, an adhesion layer of the material is formed on the inner surface of the ring die after extrusion. Therefore, material extrusion occurs on the adhesion layer and the material density of the adhesion layer is equal to the theoretical discharge density. The relationship between the density of the material discharged from the ring die granulator and the ratio of the density of the initial material, $\gamma(\theta)$, and the central angle, θ, of the ring die can be expressed by Eq. (18):

$$\gamma(\theta)=\frac{\mathrm{h}}{\mathrm{r_h}+\mathrm{e}\cos\theta-\sqrt{\mathrm{r_r^2}-\mathrm{e^2}\sin^2\theta}-\mathrm{d}}. \quad (18)$$

During material extrusion, the extrusion force varies exponentially with the material density and can therefore be estimated according to the material properties. An exponential function can be used to describe the relationship between the extrusion force, *P*, and the material density with the central angle, θ, of the ring die:

$$P(\theta)=\lambda e^{k[\gamma(\theta)-1]}. \quad (19)$$

In Eq. (19), λ and *k* are constants. In an actual granulation process, the theoretical discharge density of the adhesion layer is less than the actual discharge density and the surface extrusion force of the ring die is greater than the extrusion force of the adhesion layer. Therefore, Eq. (20) was used in this study to correct the surface extrusion force of the ring die:

$$P'(\theta)=P(\theta)\frac{\mathrm{r_h}}{\mathrm{r_h}-\mathrm{d}}. \quad (20)$$

The external excitation force of the ring die was obtained from a definite integral of the extrusion force on the inner surface of the ring die at the extrusion angles θ_t and θ_{max}. Then, the orthogonal components, F_{cx} and F_{cy}, of the centre stress of the ring die could be expressed by Eq. (21):

$$\left.\begin{aligned}F_{cx}&=P_t\mathrm{b}\mathrm{r_h}\theta_t\cos\frac{\theta_t}{2}+\int_{\theta_t}^{\theta_{max}}\mathrm{b}(\mathrm{r_h}-\mathrm{d})P'(\theta)\cos\theta d\theta\\F_{cy}&=P_t\mathrm{b}\mathrm{r_h}\theta_t\sin\frac{\theta_t}{2}+\int_{\theta_t}^{\theta_{max}}\mathrm{b}(\mathrm{r_h}-\mathrm{d})P'(\theta)\sin\theta d\theta\end{aligned}\right\}. \quad (21)$$

According to the acting angle of the ring die extrusion zone and the cosine theorem, the central angle of the extrusion circle could be expressed by Eq. (22):

$$\theta_t = \arccos\left\{\frac{\left[r_h-\left(d+h/\gamma_t\right)\right]^2+e^2-r_r^2}{2\left[r_h-\left(d+h/\gamma_t\right)\right]e}\right\},$$
$$\gamma_t = \frac{\ln P'(\theta)-\ln\lambda}{k}+1. \quad (22)$$

When γ_t=1, the maximum extrusion central angle, θ_{max}, could be obtained. The static friction coefficient, μ, was used to describe the static friction between the material and the ring die, so the resultant external force acting on the position of the ring die could be expressed by Eq. (23):

$$\left.\begin{aligned}F_{hx} &= F_{cx}+\mu F_{cy}\\ F_{hy} &= F_{cy}+\mu F_{cx}\end{aligned}\right\}. \quad (23)$$

When the ring die had x and y vibration displacements, the dynamic eccentricity value of the die roller was as shown in Eq. (24). By substituting the dynamic eccentricity, e', into the theoretical derivation described above, the dynamic random extrusion force that varied with the vibration displacement was obtained.

$$e' = \sqrt{e^2+y^2}+x. \quad (24)$$

The eccentric distance, e, of the die roller of the ring die granulator was 0.1 m. The inner diameter, r_h, of the ring die was 0.21 m. The outer diameter, r_r, of the pressing roller was 0.103 m. The thickness, d, after molding and extrusion was 0.004 m. The thickness, h, of the uncompressed material was 0.02 m. The width, b, of the ring die was 0.12 m. The extrusion calculation parameters λ and k were 1,0000 and 3, respectively, and the static friction coefficient, μ, was 0.3.

3 EXPERIMENTAL VERIFICATION

To verify the accuracy and precision of the dynamic model, a SZLH420 ring die granulator was tested in actual production. Vibration at the ring die position was not easy to test because of overhang, rotation, and limited space. The test was conducted at the bearing position 1 (node 2). The test results were compared with theoretical calculation results. In the test, an A302 wireless acceleration measurement sensor from Beijing Bitron Co., Ltd. was used for signal acquisition, a BS951-T wireless gateway was used for data transmission, and a portable computer was used for data processing and analysis. The specific experimental scheme and the schematic diagram of the test setup are shown in Fig. 7.

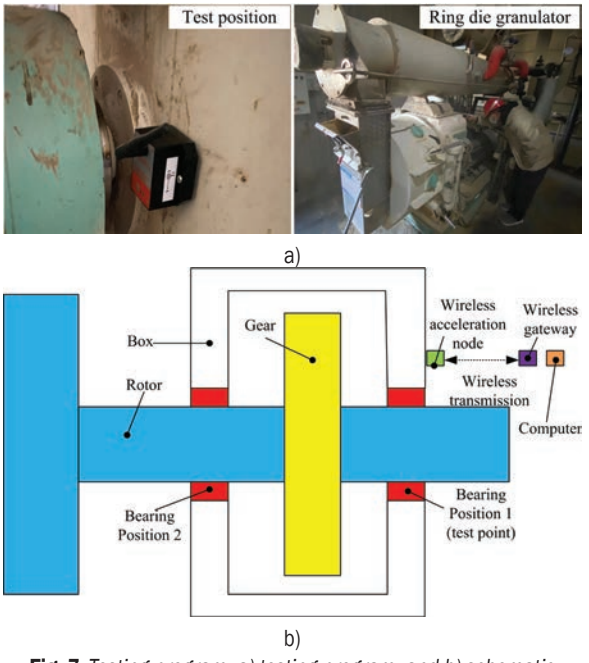

Fig. 7. *Testing program; a) testing program, and b) schematic diagram of test setup*

The acceleration data in the x- and y-directions were collected during the experiment. The vibration displacement, velocity, and acceleration curves in the time domain were obtained by processing the data with data analysis software, and the vibration curves in the frequency domain were obtained from fast Fourier transforms. The results are shown in Fig. 8a. The Newmark–β method was used to solve the nonlinear dynamics equation of the coupled system. The curves in the frequency and time domains for node 2 at the bearing position are shown in Fig. 8b. Using the stable data and comparing the experimental results and theoretical calculations, it was evident that the frequency errors and amplitudes at the peaks in the frequency-domain graphs between the experimental and theoretical results did not exceed 5 %, and the vibration amplitudes for the curves in the time domain did not exceed 10 %. The experimental results were affected by various excitation disturbances, such as those from the motor, feeder, and modulator. As a result, the experimentally measured time-domain and frequency-domain curves were more complex and the amplitudes were overestimated. The results show that the nonlinear dynamics model for the coupled overhung rotor established during this study is highly accurate and can be used for predicting system dynamic characteristics.

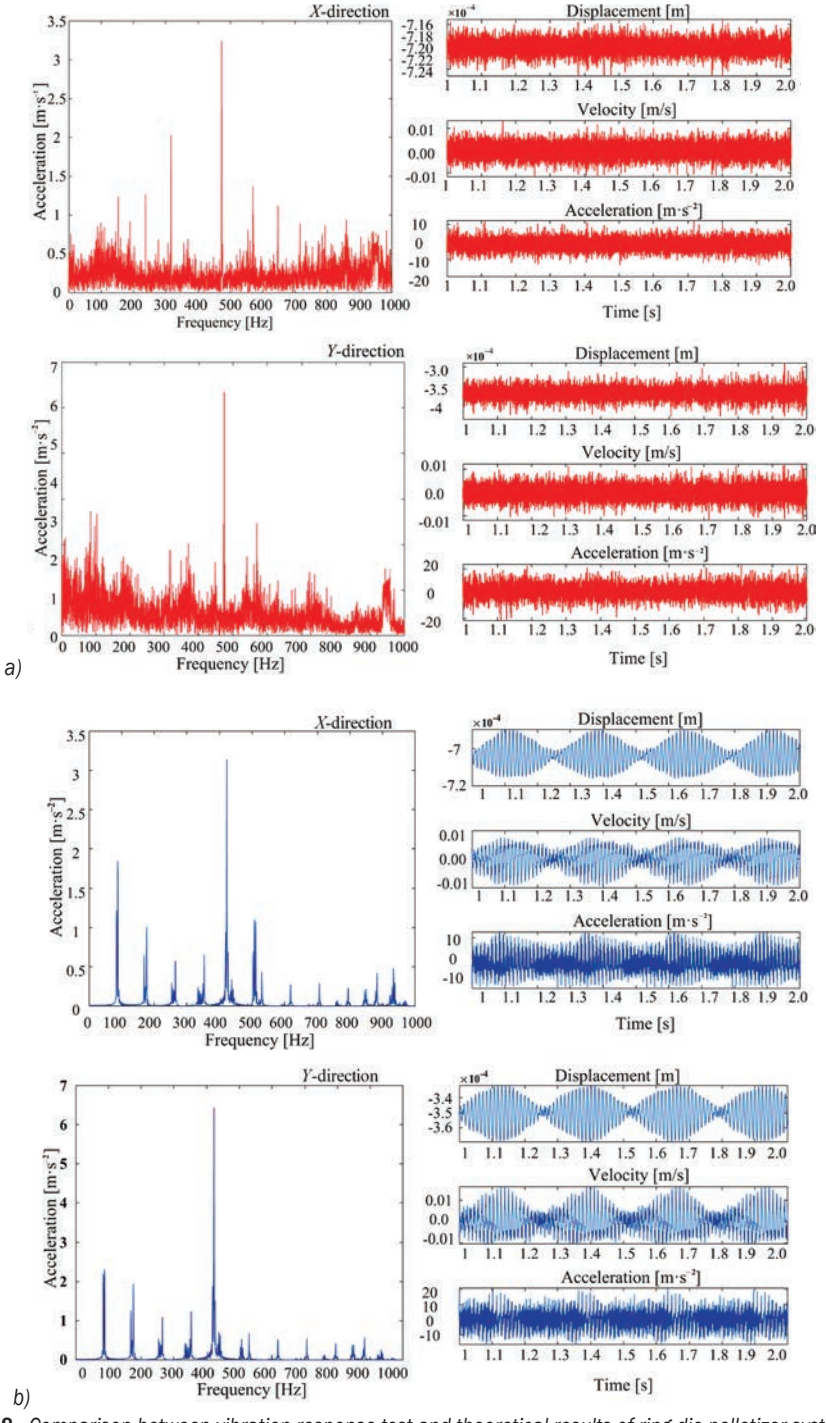

Fig. 8. *Comparison between vibration response test and theoretical results of ring die pelletizer system; a) test results, and b) theoretical results*

4 ANALYSES AND PREDICTIONS OF DYNAMIC CHARACTERISTICS OF THE COUPLED ROTOR MODEL

Ring dies in the rotor systems of ring die granulators are prone to wear. According to actual production field research, the replacement cost of a ring die accounts for more than 30 % of the production cost of the entire factory. Nonlinear vibrations at a ring die cause extreme extrusion or severe wear of the ring die, which can lead to damage of the ring die. Several

rotor parameters for the horizontal ring die granulator were selected for this study: a rotational speed of n = 300 r/min, a ring die roller eccentricity of e = 0.1 m, a bearing clearance of γ_0 = 10 μm, and a length of axle segment 7 of l_7 = 60 mm. Time-domain curves, frequency-domain curves, phase diagrams, and Poincaré section diagrams for the dynamic response in both directions at the ring mode position (node 19) are shown in Fig. 9. The figure shows that the maximum vibration displacement response in the x-direction was approximately 2.09 mm and the maximum vibration displacement response in the y-direction was 2.12 mm. These results occurred because the rotor system was subjected to the combined effects of gravity in the y-direction, the ring die force, the mesh force, and the bearing force. The time-domain curves were transformed into frequency-domain curves by fast Fourier transformation (FFT). The main vibration frequencies and amplitudes in both directions were the same, and the frequency division phenomenon caused by various external forces occurred near the low frequency. The phase diagrams were approximately closed circles and showed weak disorder and trends from quasi-periodic motion to chaotic motion. The Poincaré section was an approximate point system in a quasi-periodic motion. The current rotor system ran relatively smoothly.

4.1 Effect of the distance between the bearings on the system dynamics

For considerations of space and cost in the structural design of a granulator, the supporting distance between the two bearings of the overhung rotor should not be too large. The effect of changing the supporting distance between the two bearings,

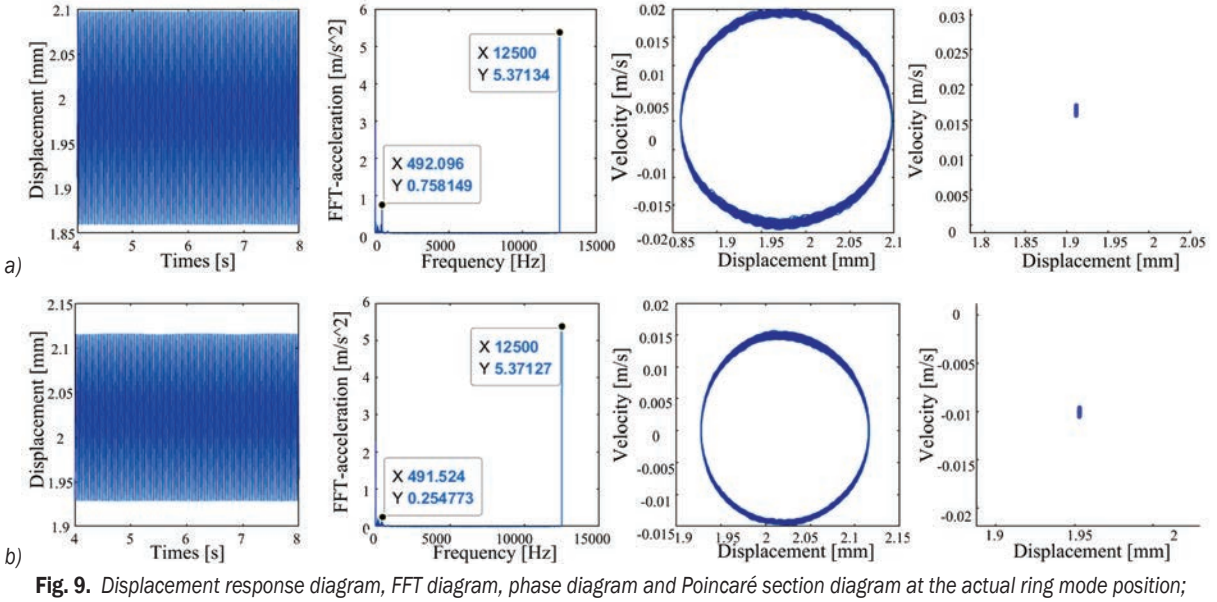

Fig. 9. *Displacement response diagram, FFT diagram, phase diagram and Poincaré section diagram at the actual ring mode position; a) x-direction, and b) y-direction*

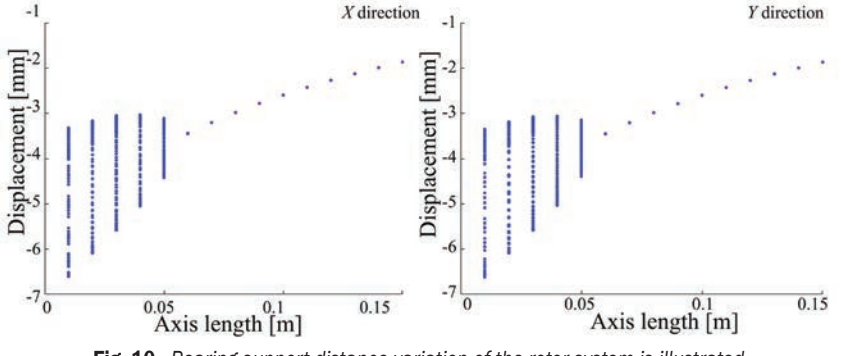

Fig. 10. *Bearing support distance variation of the rotor system is illustrated*

namely, the length of axle segment 7, on the dynamic response of the overhung rotor system is shown as a bifurcation diagram in Fig. 10. The diagram shows that as the distance between the two bearings increased, the system motion gradually changed from complex chaotic motion to quasi-periodic motion, and to period-1 motion at l_7 = 90 mm. Therefore, an appropriate increase in the bearing support distance is beneficial for optimizing the dynamic response of the system at the ring die location. Figs. 11a and b show that when l_7 = 120 mm, the maximum vibration displacement responses in the *x*- and *y*-directions were approximately 1.88 mm and 1.92 mm, respectively. The time-domain responses were significantly better than those in the actual granulator. The FFT curves show that the vibration amplitudes in both directions were significantly reduced, and the frequency division was weakened. The phase diagrams were

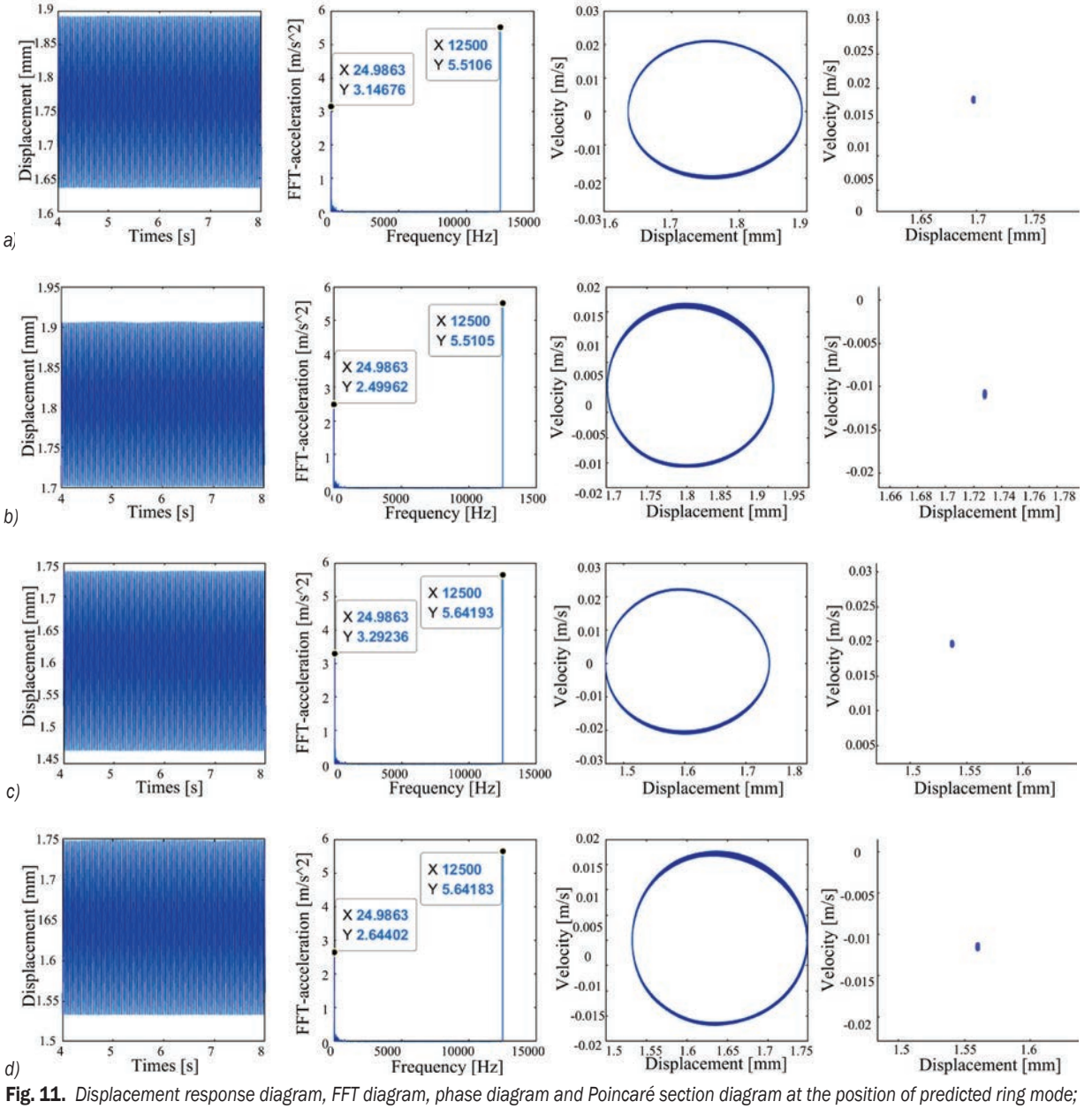

Fig. 11. *Displacement response diagram, FFT diagram, phase diagram and Poincaré section diagram at the position of predicted ring mode; a) axis segment element 7 is 90 mm in X-direction, b) axis segment element 7 is 90 mm in Y-direction, c) axis segment element 7 is 120 mm in X-direction, and d) axis segment element 7 is 90 mm in Y-direction*

approximately closed circles, the turbulence was reduced, and the periodic motion of the system tended to be stable. The Poincaré sections were point systems with quasi-periodic motion, and the current rotor system ran more smoothly. Figs. 11c and d show that the response of the rotor system was further optimized when l_7 = 80 mm. This phenomenon occurred because an appropriate increase in the bearing support distance was beneficial for optimizing the effect of the bending-torsional coupling of the system.

4.2 Effect of Roller Eccentricity on the System Dynamics

To avoid rigid collisions during the ring die assembly process, a gap is present between the die and the roller. The wear of the ring die during production operations leads to increases in the gap between the die and the roller, which causes decreases in the eccentricity of the press roller. When only the eccentricity of the rollers was varied, the effect of the roller eccentricity on the dynamic response of the overhung rotor system was predicted, and the resulting bifurcation diagrams are shown in Fig. 12. The figure shows that as the roller eccentricity increased, the system motion gradually changed from period-1 motion to quasi-periodic motion to chaotic motion. The eccentric distance affects the granulation efficiency. Appropriately reducing the eccentric distance of the roller is beneficial for optimizing the response of the rotor system. Figs. 13a and b show that when e = 0.099 m, the maximum vibration displacement responses were approximately 1.91 mm and 1.92 mm in the x- and y-directions, respectively. The time-domain responses were considerably better than those of the actual granulator. The FFT curves show that the vibration amplitudes in both directions were reduced, and the frequency division was weakened. The phase diagrams were approximately closed circles, the disorder phenomenon was reduced, and the periodic motion of the system tended to be stable. The Poincaré sections were point systems with quasi-periodic motion, and the current rotor system ran more smoothly. Figs. 13c and d shows that at e = 0.101 m, the response of the rotating system deteriorated, and the maximum vibration displacement responses were approximately 2.18 mm and 2.21 mm in the x- and y-directions, respectively. The time-domain responses were higher than the actual granulator amplitudes. The FFT curves show that the vibration amplitudes in both directions increased, the frequency division was more severe, the phase diagrams appeared severely disordered, and the system motion changed from quasi-periodic motion to mixed motion. The Poincaré sections were approximately closed cycles connected by points, representing quasi-periodic motion, and the current rotor system was unstable. This phenomenon was caused by the effect of eccentricity on the external extrusion load on the surface of the ring die and provides an important theoretical basis for adjusting the gap between the roller and the die during production operations.

4.3 Effect of Bearing Clearance on the System Dynamic Response

A strong nonlinearity exists in the bearing clearance during the bearing assembly process. The bearing clearance increases due to wear during operation. When only the bearing clearance was changed, the effect of the bearing clearance on the dynamic response of the overhung rotor system was predicated, and the resulting bifurcation diagrams are shown in Fig. 14. The figure shows that as the bearing clearance increased, the system motion changed from period-1 motion to quasi-periodic motion to chaotic motion. Regular bearing lubrication and replacement can ensure a small bearing clearance, which is conducive for optimizing the response of the rotor system. Figs. 15a and b show that when γ_0 = 40 μm, the maximum vibration displacement responses were approximately 2.19 mm and 2.22 mm in the x- and y-directions, respectively, and the time-domain response amplitudes were greater than those of the actual granulator. The FFT curves show that the vibration amplitudes in both directions increased, the low-frequency vibrations were noticeable, and the frequency division was strengthened. The phase diagrams were approximately closed ellipses, the turbulent phenomenon increased, and the periodic motion of the system tended to be chaotic. The Poincaré sections were approximately asymptotes, the system motion changed from quasi-periodic to chaotic motion, and the current rotor system operation gradually became unstable. Figs. 15c and d show that when γ_0 = 80 μm, the response of the rotating system deteriorated further, with maximum vibration displacement responses of approximately 2.32 mm and 2.34 mm in the x- and y-directions, respectively. This phenomenon was caused by the bearing clearance affecting the bearing support force of the rotor system, and it provides an important theoretical basis for equipment operation and maintenance as well as regular part and component replacement.

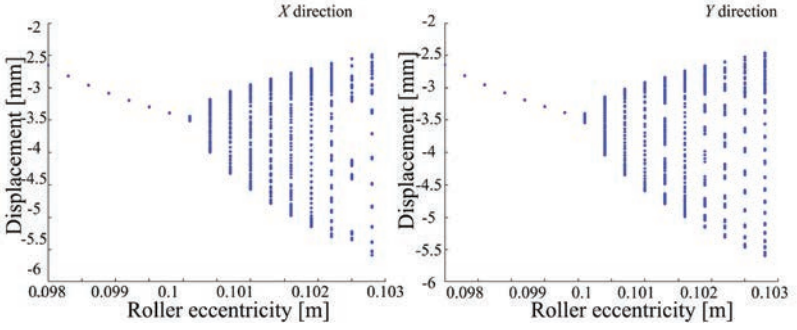

Fig. 12. *Die roll eccentricity distance variation of the rotor system is illustrated*

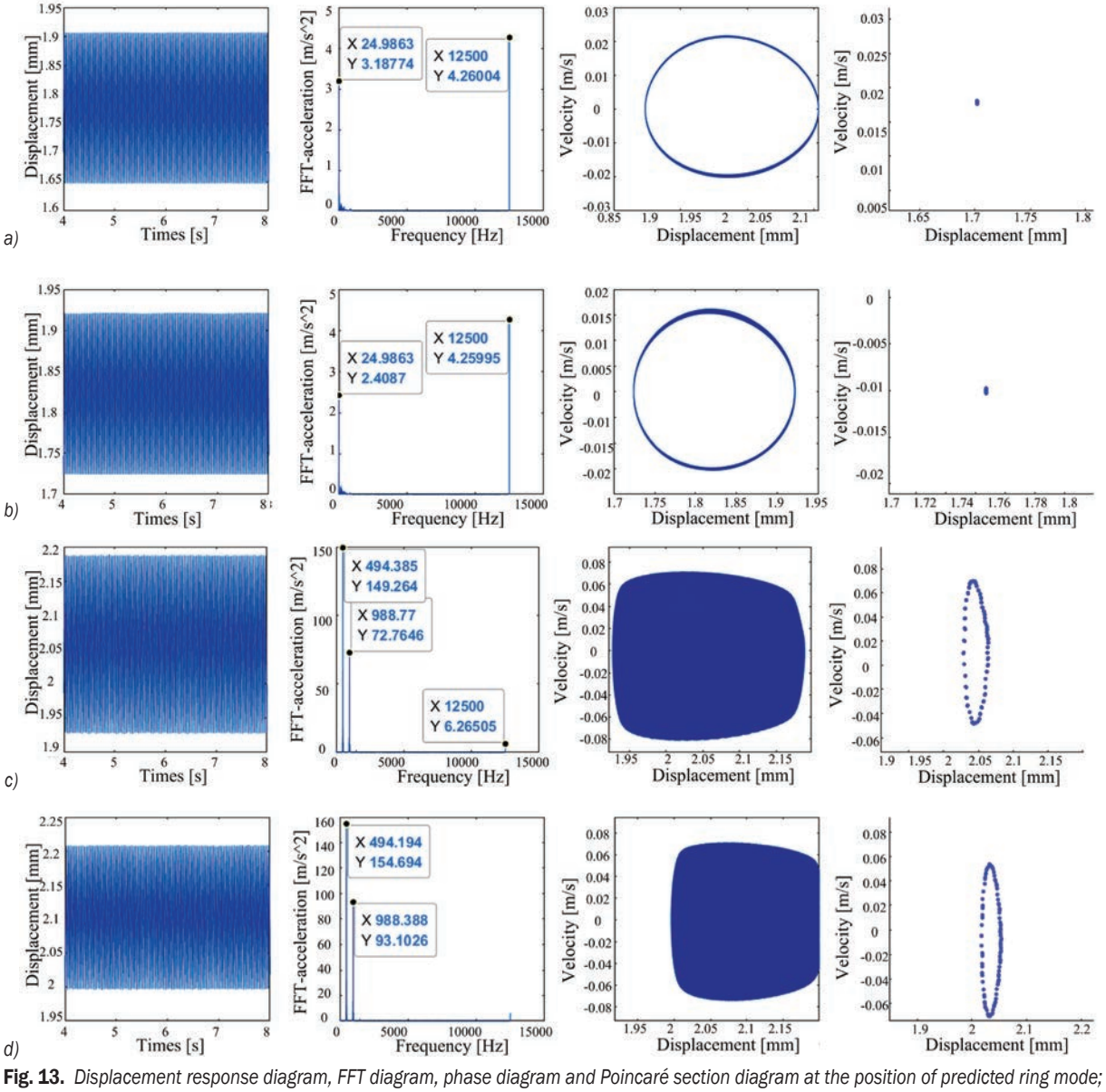

Fig. 13. *Displacement response diagram, FFT diagram, phase diagram and Poincaré section diagram at the position of predicted ring mode; a) ring roller eccentricity is 0.099 m in X-direction, b) ring roller eccentricity is 0.099 m in Y-direction, c) ring roller eccentricity is 0.101 m in X-direction, and d) ring roller eccentricity is 0.101m in Y-direction*

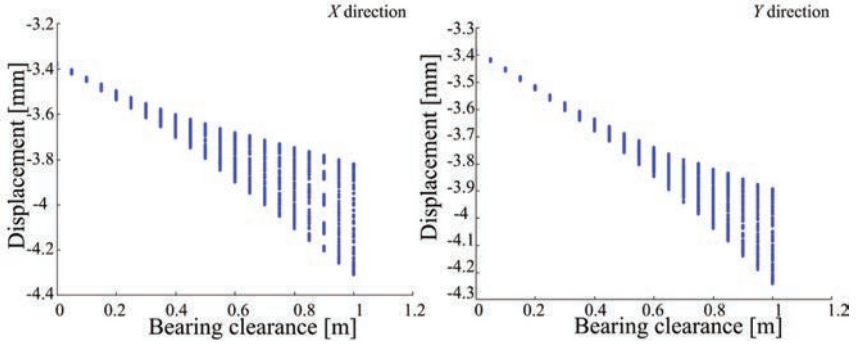

Fig. 14. *Bearing clearance variation of the rotor system*

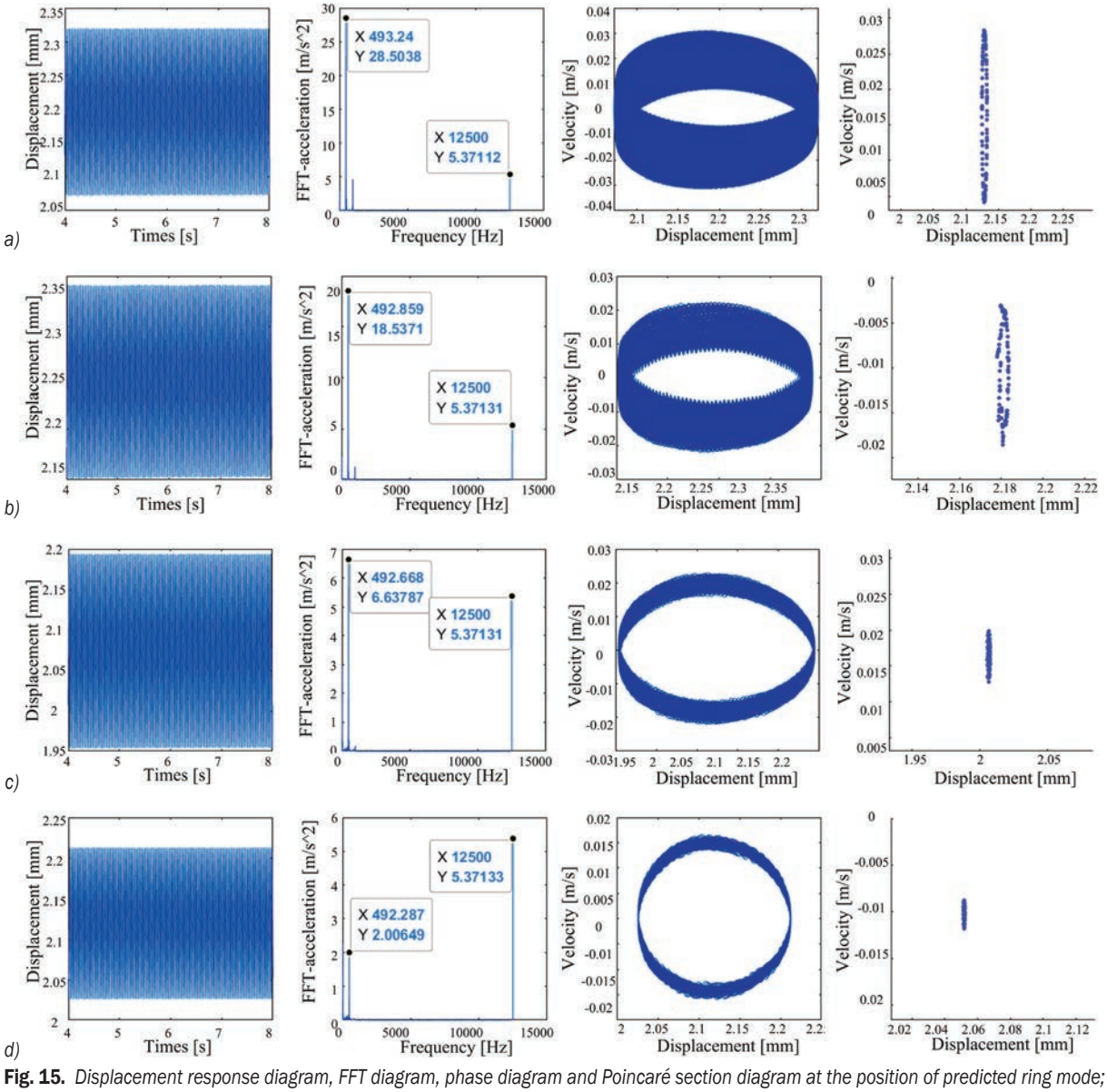

Fig. 15. *Displacement response diagram, FFT diagram, phase diagram and Poincaré section diagram at the position of predicted ring mode; a) bearing clearance is 40 μm in X-direction, b) bearing clearance is 40 μm in Y-direction, c) bearing clearance is 80 μm in X-direction, and d) bearing clearance is 80 μm in Y-direction*

5 CONCLUSIONS

In this paper, experimental verification was conducted using a real-world operating ring die granulator, and the experimental results were compared with the theoretical calculation results to verify the validity and accuracy of the theoretical model. At the same time, the correctness and practicability of the extrusion mechanics model, the gear meshing model, the bearing support model, and the multi-excitation coupling model of the rotor system are also verified. This is helpful when solving the dynamics of complex structure and excited rotor. Finally, according to the theoretical model, for the strong nonlinear factors, such as the bearing support distance, the roller eccentricity, and the bearing clearance variation, dynamic response analyses were performed using bifurcation diagrams and the effects of their parameters on rotor performance were determined. The results of this study can be summarized into three primary points:

1. The increase of bearing support distance is beneficial to the optimization of dynamic response characteristics of the system. When bearing support distance is short, the response becomes complicated and chaotic motion is easy to appear. When the bearing distance increases by 120 mm, the displacement amplitudes in *x*- and *y*- directions decrease by 0.35 mm and 0.37 mm, respectively, and the dynamic performance indexes of the system are optimized. Therefore, reasonable rotor structure design and bearing support distance selection are of great significance when optimizing system response and improving system stability.
2. The reduction of eccentricity of roll die is beneficial to the optimization of system response. Comparisons of the frequency-domain curves, the phase diagrams, and the Poincaré section diagrams showed that as the eccentric distance of the pressure roller decreased, the amplitude of the system response was reduced, the disorder phenomenon was weakened, and the dynamic performance indicators were optimized. The eccentric distance is a key factor affecting the granulation efficiency and quality. Therefore, it is important to select an appropriate eccentricity for the rollers to optimize the system response and improve the system productivity.
3. The reduction of bearing clearance is beneficial to the optimization of dynamic response characteristics of the system. Comparisons of the frequency-domain curves, the phase diagrams, and the Poincaré section diagrams showed that as the bearing clearance decreased, the amplitudes of the system response decreased, the disorder phenomenon was weakened, and the dynamic performance indicators were optimized. The bearing clearance is a key factor affecting the stability of the rotor system. Therefore, regular bearing maintenance and replacement is important for optimizing the response of the rotor system and improving the reliability of the system.

6 ACKNOWLEDGEMENTS

The authors acknowledge the financial support from the National Natural Science Foundation of China (Grant No. 52065050) & Basic research funds for universities directly under the Inner Mongolia Autonomous Region of China (Grant No. JY20220377).

8 REFERENCES

[1] Schwarz, S., Grillenberger, H., Tremmel, S., Wartzack, So. (2022). Prediction of rolling bearing cage dynamics using dynamic simulations and machine learning algorithms. *Tribology Transactions*, vol. 62, no. 2, p. 225-241, **DOI:10.1080/10402004.2021.1934618**.

[2] Cai, Z., Lin, C. (2017). Dynamic model and analysis of nonlinear vibration characteristic of a curve-face gear drive. *Strojniški vestnik - Journal of Mechanical Engineering*, vol. 63, no. 3, p. 161-170, **DOI:10.5545/sv-jme.2016.3859**.

[3] Cui, Y., Deng, S., Niu, R., Chen, G. (2018). Vibration effect analysis of roller dynamic unbalance on the cage of high-speed cylindrical roller bearing. *Journal of Sound and Vibration*, no. 434, p. 314-335, **DOI:10.1016/j.jsv.2018.08.006**.

[4] Smagala, A., Kecik, K. (2021). Nonlinear dynamics analysis of a rolling bearing. *Journal Européen des Systèmes Automatisés*, vol. 54, no. 1, p. 21-26, **DOI:10.18280/JESA.540103**.

[5] Kurvinen, E., Viitala, R., Choudhury, T., Heikkinen, J., Sopanen, J. (2020). Simulation of subcritical vibrations of a large flexible rotor with varying spherical roller bearing clearance and roundness profiles. *Machines*, vol. 8, no. 2, art. ID 28, **DOI:10.3390/machines8020028**.

[6] Luo, W, Yan, C., Yang, J., Liu, Y., Wu, L. (2021). Vibration response of defect-ball-defect of rolling bearing with compound defects on both inner and outer races. *IOP Conference Series: Materials Science and Engineering*, vol. 1207, no. 1, **DOI:10.1088/1757-899X/1207/1/012006**.

[7] Bavi, R., Hajnayeb, A., Sedighi, H.M., Shishesaz, M. (2022). Simultaneous resonance and stability analysis of unbalanced asymmetric thin-walled composite shafts. *International Journal of Mechanical Sciences*, vol. 217, art. ID 107047, **DOI:10.1016/J.IJMECSCI.2021.107047**.

[8] Wang, P., Xu, H., Yang, Y., Ma, H., He, D., Zhao, X. (2022). Dynamic characteristics of ball bearing-coupling-rotor system

with angular misalignment fault. *Nonlinear Dynamics*, vol. 108, p. 3391-3415, **DOI:10.1007/S11071-022-07451-1**.

[9] Liu, J., Ding, S., Wang, L., Li, H., Xu, J. (2020). Effect of the bearing clearance on vibrations of a double-row planetary gear system. *Proceedings of the Institution of Mechanical Engineers, Part K: Journal of Multi-body Dynamics*, vol. 234, no. 2, **DOI:10.1177/1464419319893488**.

[10] Chen, Z., , J., Wang, K., Zhai, W. (2021). An improved dynamic model of spur gear transmission considering coupling effect between gear neighboring teeth. *Nonlinear Dynamics*, vol. 106, p. 339-357, **DOI:10.1007/S11071-021-06852-Y**.

[11] Zheng X., Luo, W., Hu, Y., He, Z., Wang, Sg. (2022). Study on the mesh stiffness and nonlinear dynamics accounting for centrifugal effect of high-speed spur gears. *Mechanism and Machine Theory*, vol. 170, art. ID 104686, **DOI:10.1016/j.mechmachtheory.2021.104686**.

[12] Zhu, L.-Y., Shi, J.-F., Gou, X.-F. (2020). Modeling and dynamics analyzing of a torsional-bending-pendular face-gear drive system considering multi-state engagements. *Mechanism and Machine Theory*, vol. 149, art. ID 103790, **DOI:10.1016/j.mechmachtheory.2020.10.103790**.

[13] Shi, Z., Li, S. (2022). Nonlinear dynamics of hypoid gear with coupled dynamic mesh stiffness. *Mechanism and Machine Theory,* vol. 168, art. ID 104589, **DOI:10.1016/j.mechmachtheory.2021.104589**.

[14] Hajnayeb, A., Sun, Q. (2022). Study of gear pair vibration caused by random manufacturing errors. *Archive of Applied Mechanics*, vol. 92, p. 1451-1463, **DOI:10.1007/S00419-022-02122-4**.

[15] Liu, P., Zhu, L., Gou, X., Shi, J., Jin, G. (2021). Dynamics modeling and analyzing of spur gear pair with pitch deviation considering time-varying contact ratio under multi-state meshing. *Journal of Sound and Vibration*, vol. 513, art. ID 116411, **DOI:10.1016/j.jsv.2021.116411**.

[16] Xu, H.g, Yang, Y., Ma, H., Luo, Z., Li, X., Han, Q., Wen, B. (2022). Vibration characteristics of bearing-rotor systems with inner ring dynamic misalignment. *International Journal of Mechanical Sciences*, vol. 230, art. ID 107536, **DOI:10.1016/j.ijmecsci.2022.107536**.

[17] Cirelli, M., Valentini, P.P., Pennestrì, E. (2019). A study of the non-linear dynamic response of spur gear using a multibody contact based model with flexible teeth. *Journal of Sound and Vibration*, vol. 445, p. 148-167, **DOI:10.1016/j.jsv.2019.01.019**.

[18] Cirelli, M., Giannini, O., Valentini, P.P., Pennestrì, E. (2020). Influence of tip relief in spur gears dynamic using multibody models with movable teeth. *Mechanism and Machine Theory*, vol. 152, art. ID 103948, **DOI:10.1016/j.mechmachtheory.2020.103948**.

[19] Mo, S., Zhang, T., Jin, G.-G., Cao, X.-L., Gao, H.-J. (2020). Analytical investigation on load sharing characteristics of herringbone planetary gear train with flexible support and floating sun gear. *Mechanism and Machine Theory*, vol. 144, art. ID 103670, **DOI:10.1016/j.mechmachtheory.2019.103670**.

[20] Mo, S., Yue, Z., Feng, Z., Shi, L., Zou, Z., Dang, H. (2020). Analytical investigation on load-sharing characteristics for multi-power face gear split flow system. *Journal of Mechanical Engineering Science*, vol. 234, no. 2, **DOI:10.1177/0954406219876954**.

[21] Dai, H., Long, X., Chen, F., Xun, C. (2021). An improved analytical model for gear mesh stiffness calculation. *Mechanism and Machine Theory*, vol. 159, art. ID 104262, **DOI:10.1016/j.mechmachtheory.2021.104262**.

[22] Sun, Y., Ma, H., Huangfu, Y., Chen, K., Che, L.Y., Wen, B. (2018). A revised time-varying mesh stiffness model of spur gear pairs with tooth modifications. *Mechanism and Machine Theory*, vol. 129, p. 261-278, **DOI:10.1016/j.mechmachtheory.2018.08.003**.

[23] Chang-Jian, C.W. (2010). Strong nonlinearity analysis for gearbearing system under nonlinear suspension-bifurcation and chaos. *Nonlinear Analysis: Real World Applications*, vol. 11, no. 3, p. 1760-1774, **DOI:10.1016/j.nonrwa.2009.03.027**.

[24] Liu, J., Na, R., Cen, H. (2020). Modelling and simulation of extrusion force in biomass pelletisation by ring die pellet mill. *International Journal of Simulation and Process Modelling*, vol. 15, no.5, p. 484-490, **DOI:10.1504/ijspm.2020.110927**.

[25] Peter, S., Lammens, R.F., Steffens, K.-J. (2010). Roller compaction/Dry granulation: Use of the thin layer model for predicting densities and forces during roller compaction. *Powder Technology*, vol. 199, no. 2, p. 165-175, **DOI:10.1016/j.powtec.2010.01.002**.

[26] Lei, T., Zheng, Y., Yu, R., Yan, Y., Xu, B. (2022). Dynamic response of slope inertia-based Timoshenko beam under a moving load. *Applied Sciences*, vol. 12, no. 6, art ID 3045, **DOI:10.3390/APP12063045**.

[27] Gómez-Silva, F., Zaera, R. (2022). Dynamic analysis and non-standard continualization of a Timoshenko beam lattice. *International Journal of Mechanical Sciences*, vol. 214, art. ID 106873, **DOI:10.1016/J.IJMECSCI.2021.106873**.

[28] Zhan, D., Jiang, S., Niu, J., Sun, Y. (2020). Dynamics modeling and stability analysis of five-axis ball-end milling system with variable pitch tools. *International Journal of Mechanical Sciences*, vol. 182, art. ID 105774, **DOI:10.1016/j.ijmecsci.2020.105774**.

[29] Si, H., Cao, L., Li, P.. (2020). Dynamic characteristics and stability prediction of steam turbine rotor based on mesh deformation. *Strojniški vestnik - Journal of Mechanical Engineering*, vol. 66, no. 3, p. 164-174, **DOI:10.5545/sv-jme.2019.6283**.

[30] Zhu, H., Chen, W., Zhu, R:, Gao, J., Liao, M. (2020). Study on the dynamic characteristics of a rotor bearing system with damping rings subjected to base vibration. *Journal of Vibration Engineering & Technologies*, vol. 8, p. 121-132, **DOI:10.1007/s42417-019-00082-8**.

[31] Zhang, Y., Yang, X., Zhang, W. (2020). Modeling and stability analysis of a flexible rotor based on the timoshenko beam theory. *Acta Mechanica Solida Sinica*, vol. 33, p. 281-293, **DOI:10.1007/s10338-019-00146-y**.

Strojniški vestnik - Journal of Mechanical Engineering 69(2023)1-2, 32-48
DOI:10.5545/sv-jme.2022.331
Original Scientific Paper
Received for review: 2022-08-17
Received revised form: 2022-12-22
Accepted for publication: 2023-01-03

Angstrom-Prescott Type Models for Predicting Solar Irradiation for Different Locations in Zimbabwe

Cedrick Iradukunda[1] – Kudzanayi Chiteka[2,*]

[1] University of Zimbabwe, Department of Industrial and Mechatronics Engineering, Zimbabwe
[2] Gwanda State University, Faculty of Engineering and the Environment, Zimbabwe

Adequate assessment of solar radiation data is crucial for planning and designing solar energy systems. However, a major challenge facing solar energy technologies is the availability of solar radiation data at the specific area of interest. In this paper solar radiation and sunshine duration data from 29 stations in Zimbabwe were used to generate both monthly and annual Angstrom-Prescott (A-P) type coefficients, a and b, that are location based. The coefficients were developed using linear correlation between the clearness index and sunshine duration. The adaptation relationship between satellite and ground-measured irradiation had an R^2 of 0.6738. The correlation between the clearness index and the sunshine duration in most of the stations was fairly high with the highest coefficient of determination, R^2, of 0.9030. The A-Pregression coefficient, a, generated using the data from each station ranged between 0.2252 and 0.3976, whereas the regression coefficient, b, ranged between 0.3218 and 0.6265. The estimated and measured values of global solar radiation, H_e, and H_m, respectively from each station were compared using the mean absolute percentage error (MAPE), the root mean square error (RMSE), the mean absolute error (MAE) and the relative standard error (RSE). The MAE values for the models ranged from 0.5438 MJ/m² to 2.2845 MJ/m². The MAPE indicated a range between 2.5642 % and 10.334 %. The RSE ranged between 0.0346 % and 0.1537 % while the RMSE for the models ranged from 0.7360 MJ/m² to 2.9454 MJ/m². The statistical indicators showed results that were within the recommended range for solar radiation predicting models from similar studies.

Keywords: empirical coefficients, Angstrom-Prescott models, solar irradiation, sunshine duration

Highlights

- *Location-specific empirical coefficients from solar radiation data in Zimbabwe were generated.*
- *Angstrom-Prescott type models for solar irradiation prediction were developed.*
- *Analyzed model performance and validity using measured data.*

0 INTRODUCTION

The world has witnessed substantial negative effects of climate change on water resources, agriculture, biodiversity, human and animal health, forest systems, and socioeconomic sectors [1] and [2]. Global warming which is somewhat proportional to the increase in the concentration of greenhouse gases (GHG) in the atmosphere, is one of the major observable outcomes of climate change [3] and [4]. Increased use of fossil fuels in the energy and industrial sectors is considered one of the main causes of the growth in the concentration of GHG in the atmosphere, particularly carbon dioxide (CO_2) [5].

According to scientists, by the end of the current century, global warming may exceed an increase by 4 °C [6]. By limiting mean global warming to less than 2 °C above preindustrial levels (1850 to 1900) and pursuing efforts to keep the temperature increase to 1.5 °C, the Paris agreement was established to proffer a solution [7] to this challenge of global warming. To limit the amount of GHG released into the environment as a result of burning conventional fuels, the world's energy sector is currently concentrating on encouraging naturally replenished renewable energy sources particularly solar energy [8].

As a desirable replacement for fossil fuels, solar energy is viewed as a natural, sustainable, clean, and ample source of energy that has potential to meet the world's energy needs [9] and [10]. Many studies have been undertaken to explore this abundantly available sustainable energy source [11] and [12]. To fully and optimally deploy solar energy, there is need for accurate data to assist in the design and performance analysis of solar energy systems [13]. Over the years the need for accurate and readily available solar radiation data has led to great efforts in development of numerous methods of varying complexity by scientists to estimate solar radiation [14] and [15]. The various methods developed to forecast solar radiation include stochastic weather models, satellite imaging, linear interpolation, artificial neural networks, physical transfer processes and empirical relations using other meteorological variables [16] to [20]. For example, recent models have been developed to predict different solar radiation components using different techniques including; machine learning

*Corr. Author's Address: Gwanda State University, Faculty of Engineering and the Environment, Zimbabwe, tavakudzira@gmail.com

approach with physics-based models, statistical machine learning and numerical models [21] to [23].

Among prediction methods, the simple empirical models are still being used as the fundamental tool for estimating solar radiation, mainly due to low computation costs, accessibility of data and simplicity [24]. Many solar irradiation predictive models are data driven and hence classified as empirical. These empirical models are grouped into extensive categories according to their input meteorological parameters such as sunshine duration based models, cloud cover based models, latitude and temperature based models [25]. The main types of empirical models are based on sunshine, temperature and relative humidity [26] to [28].

Machine learning models have also been used in predicting solar radiation. These are trained artificial systems that combine various meteorological input variables like sunshine duration, temperature, relative humidity and cloud cover from both satellite imaging and ground measurements to predict solar radiation [29]. Robust linear regression, support vector machines, artificial neural networks, extreme gradient boosting (XGBoost), and random forests are some of the machine learning models that have recently emerged as sophisticated methods for constructing more precise correlations between inputs and outputs [30] to [34]. Machine learning models perform well when estimating solar irradiation, but their ease of use and transferability from the development site to the intended areas is totally dependent on the geographic and climatic condition [27]. ARIMA-GP evolutionary models were recently developed by Nwokolo et al. [21] and [22] and these were found to be sufficiently accurate in the prediction of solar irradiation in different locations.

Many other attempts have been made to develop models to predict solar irradiation. For example, Sabbagh et al. [35] proposed a model for use in dry arid or semi-arid regions, such as Iran, where the average sea level is higher. The model considered the effect of relative humidity (*RH*), and maximum temperature (T_{max}) on solar radiation. Kasten and Czeplak [36] developed a cloud cover based model that correlated the ratio of global solar radiation (*H*) to the total amount of cloud cover and global radiation at cloudless sky (H_o). Nwokolo [37] performed a comprehensive review of empirical models used for estimating global solar radiation in Africa and West Africa. The study indicated that hybrid models performed better than single-parameter based models in the prediction solar radiation. In a different study, Nwokolo and Ogbulezie [38] undertook a quantitative review and classification of empirical models used for predicting global solar radiation in West Africa. The study recommended the need to make use of soft computing as an alternative approach to estimating global solar irradiation with high precision in West Africa.

Temperature based models are also popular and some of these assume that the difference between the maximum and minimum temperature is directly linked to solar radiation received at the surface [39]. Bristow and Campbell [40] proposed a temperature based model that relates solar irradiation to maximum and minimum temperature cognisant of the transmissivity of the atmosphere. In a different study, Donatelli and Campbell [41] devised a model that takes into account the average air temperature and minimum temperature functions, as well as the atmosphere's transmissivity coefficient to predict solar radiation. A study by Nwokolo eand Ogbulezie [42] investigated a single hybrid parameter-based model for optimizing the Hargreaves-Samani coefficient in Nigeria. The study indicated that the same approach could also be applied in the prediction of global solar radiation.

Sunshine duration-based models have been found to be equally important and applicable to solar irradiation prediction. The Angstrom-Prescott (A-P) model is the first linear correlation relating solar radiation to sunshine duration and is the most commonly employed model for predicting global solar radiation as a result of availability and reliable sunshine duration measurements in most meteorological stations [43]. Many modifications of this model have been proposed in literature. For example, the Glover and McCulloch model which is a modification of the A-P model further incorporate the latitude into the linear A-P model [44]. Likewise, the modified A-P model established by Page [45] is considered a model that can be used anywhere in the world; however, it should be noted that it was developed for a latitude of 40 degrees, thus it is preferable to recalculate the correlation coefficients of, a and b, [27], [46] and [47].

The Bahel model is also based on sunshine duration and is a relationship between sunshine duration and solar radiation data obtained from 48 weather stations around the world, under various geographical and meteorological conditions [48]. On the other hand, Dehkordi et al. [49] developed modified coefficients of the A-P model for six meteorological stations across the arid and semi-arid regions of Iran. The study generated A-P models for each station using meteorological data recorded from 1992 to 2017.

Mostafazadeh et al. [50] developed two modified A-P models for predicting solar radiation using both sunshine duration and solar radiation data from Urmia and Tabriz stations in Iran from the period of 2014 to 2017. In order to evaluate the models' accuracy, the study employed root mean square error (*RMSE*), mean absolute bias error (*MABE*) and Nash-Sutcliffe efficiency indices. The statistical analysis of the models indicated that the modified models of Urmia and Tabriz stations produced very good prediction values. The conclusion was that since sunshine duration is an important variable for estimating solar radiation then the modified A-P models can be used to predict solar radiation in Iran [49] and [50]. Mejia et al. [51] developed an algorithm for predicting solar radiation in Ciudad Juarez Chihuahua, Mexico based on a modified A-P model. The modified prediction model was developed using data from NASA's World Energy Resources forecast database for Ciudad Juarez, Chihuahua, including daily average radiation and sunlight duration.

Lewis [52] used two empirical models to estimate solar irradiation over Zimbabwe using measured data from a station based in Harare. The first model was a correlation between clearness index and the fraction of sunshine hours based on the A-P model and the second model was based on a linear correlation between clearness index and maximum temperatures and *RH*. The study generated correlation coefficients for the first model and used similar data from Nigeria by Swartman and Ogunlade [53], then generated correlation coefficients for the second model and used similar data from Iran by Sabbagh et al. [35] to test and analyse the applicability of both models. The analysis concluded that the first model based on sunshine duration data was the better of the two models as it estimated solar radiation values that were close to the measured values. The study also concluded that the use of the first model to predict solar irradiation over Zimbabwe was less accurate as only data from Harare was used to generate the model, hence the study recommended the use of data from other stations across Zimbabwe to generate more location specific models which would perform much better than a model based on data from a single location.

Chagwedera and Sendezera [54] developed two correlation models of the Angstrom type to predict the monthly average daily global solar radiation incident on a horizontal surface using meteorological data from two locations (Bulawayo and Harare) in Zimbabwe. The study used the models to generate estimated solar radiation values which were compared to measured solar radiation data. The results showed good agreement between measured and predicted solar radiation values and the authors concluded from the findings that modifying the Angstrom type model to generate location-based models produces improved solar radiation predictions.

Chiteka and Enweremadu [55] developed an artificial neural network model for predicting horizontal irradiation for important sites in Zimbabwe, which included a seven input layer, one hidden layer, and a single output layer. The inputs of the neural network developed by the authors consisted of geographical data of altitude, latitude and longitude and meteorological data of humidity, pressure, clearness index and average temperature. The best predictive model of all the models studied was a network with 10 neurons and a tansig transfer function in both the input and output layers. The network had a coefficient of determination of 99.894 %, a *RMSE* of 0.223 kWh/m^2/day, a mean absolute error (*MEA*) of 0.17 kWh/m^2/day, and a mean absolute percentage error of 2.56 %, according to the evaluations.

The A-P model is an economic, meteorological and geographic empirical model that has been applied in different locations around the world to predict the proportion of solar irradiation incident on the horizontal surface in all sky conditions anywhere on the globe [27] and [39]. Studies agree on its simplicity and remarkable performance due to the strong correlation between sunshine duration and solar radiation. Despite its low performance compared to machine learning models, it is a powerful hybrid estimation technique, and this attribute gives the A-P model an advantage or preference over other linear and nonlinear functional forms to improve the accuracy of the model's performance, making it a reference model.

Understanding and measuring the solar radiation's spatial-temporal distribution is crucial for optimizing solar energy harvesting in many applications. At numerous meteorological stations and individual weather stations, measurements of solar radiation are taken on the ground using two different types of instruments i.e., a pyrheliometer and a pyranometer. Adequate assessment of solar radiation data is crucial for planning and designing solar energy systems [56]. However, a major challenge facing solar energy technologies is the availability of solar radiation data at the specific area of interest. There are three main ways in which this deficiency in solar radiation data manifests itself: low spatial coverage, a short record and a lack of both global radiation data and sunshine duration [57]. The shortage of solar radiation data arises as a result of a finite number of observation

stations mainly due to financial and technical limitations especially in developing countries [17].

In Zimbabwe station-based meteorological solar radiation data still remains scant as there are only a few weather stations that measure solar irradiation. At these stations data recording on solar irradiation is measured by pyranometers and is monitored by the Meteorological Services Department (MSD) [58]. Pyranometric measurements are difficult to obtain due to high costs of setting up the measuring equipment. This unavailability of measured solar irradiation data in developing countries is a major limitation when assessing solar energy potential in various areas [59]. As a result, a continual mapping of solar radiation via estimation is required [57].

Solar radiation at the surface of the earth is a complex parameter to accurately estimate due to varying weather conditions across the globe, therefore this limits the A-P model to a location specific model. The A-P model's accuracy can be enhanced by introducing into the initial model, site specific meteorological data and parameters [51]. It is against this background that models are developed based on the A-P model for predicting solar irradiation specific for the environment in Zimbabwe. In many studies in which the different empirical models have been compared, it has been observed that the sunshine duration based models perform better than the other empirical models and most of the sunshine based models generated to estimate solar radiation are modifications of the A-P model [60]. As such, the model has become a reference and fundamental model for estimating solar radiation in any location in the world.

Meteorological stations in Zimbabwe that measure, and record ground solar radiation are sparsely distributed over a landscape with dynamic climate and weather shifts. Furthermore, the solar radiation data available at the few stations in Zimbabwe is historical data ranging between 1975 to 1999, hence it is not applicable to current solar radiation research as the data does not incorporate atmospheric changes that have occurred over the years. Solar radiation data from solar resource maps and spatial solar radiation data sets is more consistent than the ground measured data but its limitation is that the data is less accurate due to exclusion of atmospheric impact on solar irradiation received on the ground. The use of outdated and/or less accurate solar data from the meteorological stations and satellite database results in overestimation or underestimation of both research and design outputs which can affect the financial decisions of solar radiation-based projects and research significantly. Moreover, geostationary satellites often have no coverage in some areas on the globe [61] and hence various authors have tried to overcome this drawback by correlating the satellite derived data with corresponding ground measurements, thus generating a correction factor for the satellite data.

It is therefore imperative to develop a solar irradiation predicting model adapted from the consistent satellite data and both current and historical ground measured solar radiation data specific to the environment in Zimbabwe. Developing a solar radiation predicting model based on the A-P model will reduce the need to establish expensive solar radiation measuring equipment since the solar irradiation will easily be estimated by the model. In this study, location-specific empirical coefficients were generated from solar radiation data from locations in Zimbabwe. This was followed by developing an A-P model for estimating solar irradiation. The model was analysed and validated for its applicability by comparing with measured data. The rest of this study is structured as follows; section 1 focuses on the materials and methods used in the study while section 2 outlines the results and discussion of the results. Section 3 highlights the major conclusions of the study.

1 METHODOLOGY

1.1 Study Location

Zimbabwe is a landlocked country in the Southern part of Africa surrounded by countries like Zambia in the north, South Africa in the south, Botswana in the west and Mozambique in the east. This country is located in the tropics between latitude 15.61 ˚ S to 22.42 ˚ S and longitude 25.24 ˚ E to 33.05 ˚ E [62]. The climate is subtropical in general, however, it may be divided into five distinct climatic zones according to the Koppen-Geiger classification [63]. The north and east are particularly warm and wet, and are classified as humid and subtropical, with a highland zone in the centre-east. In the shadow of the eastern highlands, the high elevation plateau in the west experiences milder temperatures and is protected from rain, resulting in a climate that is closer to semi-arid. This semi-arid zone stretches from the country's southernmost point to the southeast, where a tiny area of near-desert conditions exists [63].

1.2 Meteorological Datasets

The data sets used comprised of three different data sources including ground measurements from 29

meteorological stations in Zimbabwe, measurements from a University of Zimbabwe observation station as well as solar radiation satellite-based observational data obtained from NASA POWER Data Access [64]. Historical pyranometer measurements of monthly mean solar radiation measurements were obtained from the MSD. The data range was from January 1971 to June 2000 but only nineteen of the 29 stations measured monthly solar radiation. Recent ground measured monthly solar radiation data from 2006 to 2020 was also obtained from a mini-meteorological station at the University of Zimbabwe Physics Department.

Satellite-based global solar radiation data on a horizontal surface for the 29 stations over a period of 15 years (2006 to 2020) was also obtained from NASA POWER Data Access. These datasets are enhanced meteorological datasets developed with the Goddard Earth Observing System (GEOS) atmospheric model and Data Assimilation System (DAS) with a spatial resolution of 0.5° longitude and 0.5° latitude [28], [65] and [66]. The datasets have been used over the years in many studies where ground measurements are not available, to obtain daily global solar radiation data [67] and [68]. The monthly average sunshine duration measurements recorded by sunshine recorders was obtained from the MSD for the 29 meteorological stations in Zimbabwe from the period of 1971 to 2020.

1.3 Satellite Data Correction

The evaluation of satellite data performance has been found to possess significant biases, which can be attributable to potential errors in the satellite data measurements of ground parameters due to changes in tropospheric features and surface environmental conditions as well as measuring methods [69] to [72]. Hence, applying a correction factor to satellite-derived data in order to obtain corresponding ground based measurements results in a comprehensive solar radiation database [73] to [75].

The mini station at the University of Zimbabwe Physics Department was the only station with recently recorded monthly ground measurements of solar radiation from the year 2006 to 2020. Therefore, the ground measured data at the mini-station were used to calibrate the satellite-based measurements in order to make the data sets compatible through a correlation plot between ground-based and satellite-based solar radiation measurements.

1.4 Meteorological Parameters

The computation of the extra-terrestrial solar radiation (H_o) is shown in Eq. (1) as a function of the latitude (φ) [76].

$$H_o = \frac{24\times 3600}{\pi}\times I_{sc} \times E_o\left[\frac{\pi}{180}\omega_s \sin\varphi \sin\delta + \cos\varphi\cos\delta\sin\omega_s\right]. \quad (1)$$

The solar constant, I_{sc}, is the energy from the sun per unit time received on a unit area of a surface perpendicular to the direction of the radiation at the mean Earth-Sun distance outside the atmosphere and is given by 1367 W/m^2 as adopted by the World Meteorological Organisation [77]. E_o, is the relative earth-sun distance or the eccentricity correction factor of the earth's orbit and its value is given by the Eq. (2) where n is the day of the year starting from 1 to 365 and 366 on a leap year [78].

$$E_0 = 1 + 0.033\times\cos\frac{360n}{365}. \quad (2)$$

The solar declination angle, δ, and the sunset hour angle, ω_s, are computed using Eqs. (3) and (4), respectively [79].

$$\delta = 23.45\sin\left[360\left(\frac{284+n}{365}\right)\right], \quad (3)$$

$$\omega_s = \cos^{-1}\left(-\tan\delta\tan\varphi\right). \quad (4)$$

The maximum possible sunshine duration in hours is given by Eq. (5) [76]:

Table 1. *Computed meteorological parameters for selected locations*

Station	Latitude [°]	Elevation [m]	S_o [h]	S [h]	S/S_o	H [MJ/m^2]	H_o [MJ/m^2]	H/H_o
Beitbridge	-22.22	457	8.503	11.998	0.7135	21.319	33.774	0.6380
Grand Reef	-18.98	1019	8.193	11.998	0.6878	21.234	34.406	0.6529
Gweru	-19.45	1429	8.316	11.998	0.7001	22.301	34.318	0.6638
Mt Darwin	-16.78	953	8.209	11.998	0.6900	21.696	34.781	0.6383
Nyanga	-18.22	1679	7.675	11.998	0.6458	21.250	34.541	0.6288
Victoria Falls	-17.93	1062	8.890	11.998	0.7494	24.075	34.590	0.7107

$$S_o = \frac{2}{15}\omega_s. \quad (5)$$

H_o, and, S_o, where thus computed using Eqs. (1) and (5) respectively per station for each month and their averages per station are shown in Table 1.

1.5 Data Quality Control

The data for modelling was reliant on solar radiation and sunshine data and therefore it was imperative to check the quality of both ground and satellite-based data in order to minimise errors in the models. The scatter envelope technique was used to check the quality of data between the clearness index, H/H_o, and the fraction of the sunshine duration, S/S_o. The scatter envelope technique is a statistical method that quantifies the boundaries and number of data outliers using standard statistics such as standard deviations and averages [80]. The input data were the fraction of sunshine duration and the clearness index, therefore the clearness index was divided into ten equal bands, each with a fraction of sunshine duration value of 0.1. In each band, the standard deviation, σ, and mean value of the clearness index, H/H_o, shown in Fig. 1. were assessed, and the dispersion envelope was defined by the limits ($H/H_o \pm 2\sigma H/H_o$). The dispersion envelope is the area bordered by the two curves that represent the upper and lower bounds, with the higher limit representing ($H/H_o + 2\sigma H/H_o$) and the lower limit representing ($H/H_o - 2\sigma \mathrm{H/H}_o$) [81].

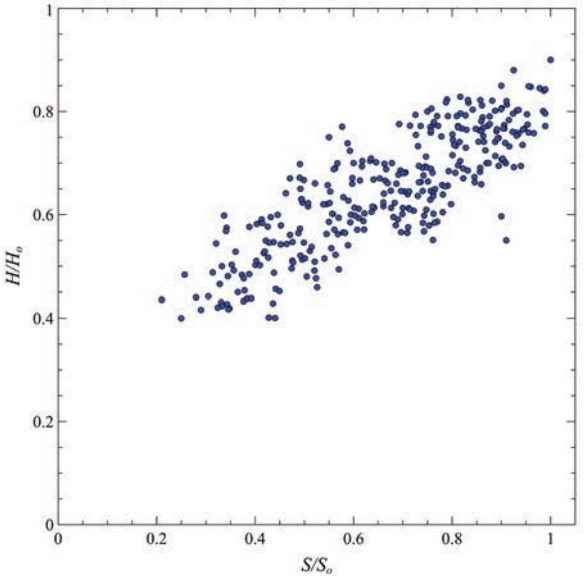

Fig. 1. *Data quality control of clearness index and sunshine duration fraction*

Outliers were defined as data points that were outside of the envelope and were rejected before the data was used in the study. After the analysis, 0.276 % of the data was rejected and deemed unsuitable. Similar studies including that of Nwokolo et al. [27] most government meteorological stations are unable to continuously set-up or measure this radiometric parameter in most metropolitan cities and remote villages where there is a severe need for electricity. This is because most locations are not connected to the national grid due to high cost implications. Global solar radiation (H) applied this technique on clearness index and sunshine duration fraction data from meteorological stations in Nigeria and observed a 0.34 % data reduction in the sample data.

1.6 Development of A-P Type Models

1.6.1 Computation of Regression Coefficients

The regression coefficient, a, in Eq. (6) indicates the fraction of extra-terrestrial radiation on a maximum overcast day, and the regression coefficient, b, represents the rate of increase of clearness index with respect to sunshine hours. Monthly and annual regression coefficients, a and b, were computed from the monthly values of clearness index, H/H_o, and sunshine duration fraction, S/S_o, by means of scatter plots.

Table 2. *Annual A-P coefficients for selected stations*

Station	A-P coefficients		R^2
	a	b	
Beitbridge	0.29 77	0.4770	0.6394
Grand Reef	0.2765	0.5108	0.9030
Gweru	0.2252	0.6265	0.8849
Mt Darwin	0.3066	0.4807	0.7986
Nyanga	0.2362	0.6080	0.8601
Victoria Falls	0.2677	0.5912	0.8391

Notes. The regression coefficients, a and b, represent the y-intercept and the gradient of the regression equation respectively and R^2 represents the coefficient determination for each station.

The monthly regression coefficients developed for selected locations are shown in Table 2 which were developed from monthly clearness index and sunshine duration fractions from each station. For the annual A-P coefficients linear regression lines were plotted for each station which expressed the regression coefficients, a and b, as the linear y-intercept and gradient of each line respectively.

$$\frac{H}{H_o} = a + b\frac{S}{S_o}. \quad (6)$$

The variations of the A-P type regression coefficients, *a* and *b*, with geographic variables like elevation, latitude and longitude were computed as shown in Table 5 in order to determine and illustrate the effect of these variables on the coefficients.

1.6.2 Generation of Estimated Solar Radiation Values

The developed monthly regression coefficients, *a* and *b*, together with the sunshine duration measurements, *S*, monthly extra-terrestrial solar radiation, H_o, and maximum sunshine duration values, S_o, from each station, were used to estimate monthly global solar radiation, H_e, using the A-P type models for each station. For the nineteen stations with both historical solar radiation data and current calibrated solar radiation data, both sets of data were combined to generate estimated values of, *H*, for the period of 1971 to 2000 (historical) and 2006 to 2020 (current). The remaining ten stations without ground measured historical solar radiation data, only the calibrated solar radiation data from 2006 to 2020 was utilised to generate estimated solar radiation values.

1.7 Model Validation and Statistical Analysis

1.7.1 Model Validation

To evaluate the model, estimated solar radiation values generated by the general model were compared with measured solar radiation values for each individual station. The estimated and measured values of global solar radiation, H_e and H_m, respectively from each station were compared using statistical analysis methods. The coefficients of Determination, R^2, obtained from the plots between measured and estimated solar radiation values were used to determine the relation between the two values. The relationship increases positively when the correlation coefficient increases from 0 to 1 [82] and [83].

1.7.2 Model Performance Analysis

Performance analysis of the models was done using the approaches which include the coefficient of determination R^2, mean absolute percentage error (*MAPE*), residual mean square error (*RMSE*), mean absolute error (*MAE*) and the relative standard error (*RSE*) respectively shown by Eqs. (7) to (11). The acceptable range for *MAPE* and *RSE* is between 0 % and 10 % and for *RMSE* and *MAE* is between 0 MJ/m^2 and 10 MJ/m^2 when comparing estimated and measured solar radiation values, and these statistical evaluation methods are the most commonly used to evaluate empirical models [27], [67], [68], [84] to [87]. *MAPE* values less than 10 % indicate a good precision model [17] and [88]. The closer the *RMSE* values are to zero the more accurate the model is and a value of *RMSE* equals zero is the ideal value [17], [51] and [89].

$$R^2 = \frac{RSS}{TSS}, \quad (7)$$

$$MAPE = \left| \left[\frac{\sum_{i=1}^{n} \left(\frac{H_{i,e} - H_{i,m}}{H_{i,m}} \right)}{n} \right] \times 100 \right|, \quad (8)$$

$$RMSE = \sqrt{\frac{\sum_{i=1}^{n} \left(H_{i,e} - H_{i,m} \right)^2}{n}}, \quad (9)$$

$$MAE = \frac{\sum_{i=1}^{n} \left| \left(H_{i,e} - H_{i,m} \right) \right|}{n}, \quad (10)$$

$$RSE = \sqrt{\frac{\sum_{i=1}^{n} \left(\frac{H_{i,e} - H_{i,m}}{H_{i,m}} \right)^2}{n}}, \quad (11)$$

where, *RSS* is the residuals sum of squares and *TSS* is total sum of squares, *i*, is the, i^{th}, value and, *n*, is the total number of measured or estimated values.

2 RESULTS AND DISCUSSIONS

2.1 Satellite Data Correction

Each satellite-based measurement was paired with a corresponding ground measurement for each month measured between the years 2006 to 2020. As a result, a correction equation was generated relating ground-measured data, H_{grn}, to satellite based data, H_{sat}, as shown by Eq. (12) and Fig 2.

$$H_{grn} = 3.7114 + 0.7568 H_{sat}. \quad (12)$$

In Fig. 2 the coefficient of correlation $r = 0.8209$ ($R^2 = 0.6738$) shows a high positive relationship between, H_{grn}, and, H_{sat}, hence, *r*, was regarded a high enough coefficient of correlation to support the use of Eq. (12). The satellite-based solar radiation

data is consistent in terms of measurement, hence the correction equation obtained from the mini-station was used to generate current ground-based values from corresponding satellite-based values for the other 29 meteorological stations.

2.2 Characterization of Meteorological Parameters

The averages of global solar radiation, H, extra-terrestrial solar radiation, H_o, sunshine duration, S, maximum sunshine duration, S_o, the clearness index, H/H_o, and fraction of sunshine duration, S/So, for selected stations are presented in Table 1. In Table 1, it can be seen that the, H, S, H/H_o, and, S/S_o, differ for each station and these variabilities can be attributed to the latitude, longitude and altitude of each location-based station. In Table 1, it can be observed that, H/H_o and S/S_o, reduce in magnitude as the longitude increase from the east to the west of Zimbabwe. According to the Koppen-Geiger classifications the western part of the country is semi-arid hence experiences much more solar radiation with increased sunshine hours and these variables reduce towards the eastern part of the country in the eastern highlands with subtropical highland climate. This then implies that locations based in the western part of Zimbabwe receive increased solar radiation than locations close or within the eastern highlands due to the atmospheric differences between the two regions.

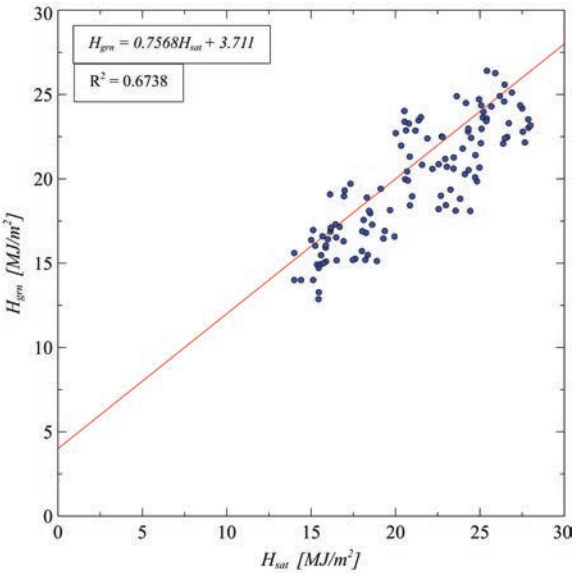

Fig. 2. *Ground and satellite measured data correlation, University of Zimbabwe (2006 to 2020)*

According to the World Meteorological Organization (WMO) [90], the fraction of sunshine duration (S/S_o) classifications are as follows: cloudy sky $0 \leq S/S_o < 0.3$, scattered clouds $0 \leq S/S_o < 0.7$ and clear sky $0.7 \leq S/S_o < 1.0$.

The locations under study show a mixture of scattered clouds and clear sky characteristics. Seventeen of the stations indicated scattered clouds predominance, whilst twelve of the stations indicated

Table 3. *Monthly A-P type regression coefficient, a, for selected locations*

a	Month											
Station	Jan	Feb	Mar	Apr	May	Jun	Jul	Aug	Sep	Oct	Nov	Dec
Beitbridge	0.31	0.29	0.27	0.32	0.33	0.42	0.59	0.32	0.38	0.26	0.31	0.33
Grand Reef	0.32	0.26	0.35	0.33	0.38	0.24	0.28	0.40	0.24	0.23	0.49	0.28
Gweru	0.32	0.29	0.24	0.20	0.27	0.25	0.39	0.42	0.29	0.21	0.28	0.29
Kutsaga	0.33	0.33	0.44	0.44	0.28	0.55	0.66	0.48	0.31	0.61	0.62	0.48
Mt Darwin	0.31	0.32	0.32	0.35	0.42	0.37	0.44	0.40	0.33	0.33	0.30	0.32
Nyanga	0.31	0.28	0.30	0.34	0.39	0.37	0.29	0.34	0.25	0.23	0.29	0.29
Victoria Falls	0.29	0.29	0.31	0.10	0.08	0.06	0.16	0.52	0.31	0.30	0.33	0.30

Table 4. *Monthly A-P type regression coefficient, b, for selected locations*

b	Month											
Station	Jan	Feb	Mar	Apr	May	Jun	Jul	Aug	Sep	Oct	Nov	Dec
Beitbridge	0.45	0.47	0.53	0.47	0.46	0.31	0.10	0.46	0.36	0.53	0.45	0.42
Grand Reef	0.43	0.52	0.40	0.46	0.41	0.57	0.53	0.37	0.54	0.54	0.13	0.50
Gweru	0.43	0.50	0.60	0.66	0.60	0.63	0.45	0.40	0.52	0.61	0.50	0.50
Kutsaga	0.37	0.35	0.22	0.27	0.52	0.20	0.07	0.27	0.43	0.02	0.12	0.04
Mt Darwin	0.47	0.44	0.47	0.45	0.38	0.45	0.34	0.37	0.41	0.39	0.44	0.45
Nyanga	0.44	0.49	0.49	0.47	0.44	0.49	0.58	0.49	0.56	0.56	0.46	0.48
Victoria Falls	0.55	0.56	0.54	0.81	0.83	0.95	0.72	1.45	0.51	0.52	0.49	0.55

clear sky predominance, which are mainly located in the semi-arid regions of the country. The least sunshine duration fraction was 0.1588 at Mukandi Meteorological Station located in the eastern highlands with subtropical highland climate, whilst the highest sunshine duration fraction was 0.7494 at Victoria Falls Meteorological Station located in the north-west part of the country with semi-arid climatic conditions. The World Meteorological Organisation [90] classifies the monthly clearness index, H/H_o, into three meteorological classifications as follows: very cloudy weather ($H/H_o \leq 0.4$), partially covered weather ($0.4 \leq H/H_o \leq 0.7$) and clear weather ($H/H_o \geq 0.7$). The generalised datasets shown in Table 1 indicated that for all the stations under study the predominant meteorological condition is partly cloudy with average clearness index between 0.5 and 0.7. The lowest clearness index was 0.3352 at Mukandi Meteorological Station and the highest was recorded at Victoria Falls Meteorological Station as 0.7107.

2.3 Relationships between H/H_o and S/D_o

To generate the A-P type regression coefficients, *a* and *b*, for each station plots between the clearness indexes, H/H_o, and the sunshine duration fractions, were generated as represented in Fig. 3. In Fig. 3, it can be observed that, H, and, H/H_o, increase with

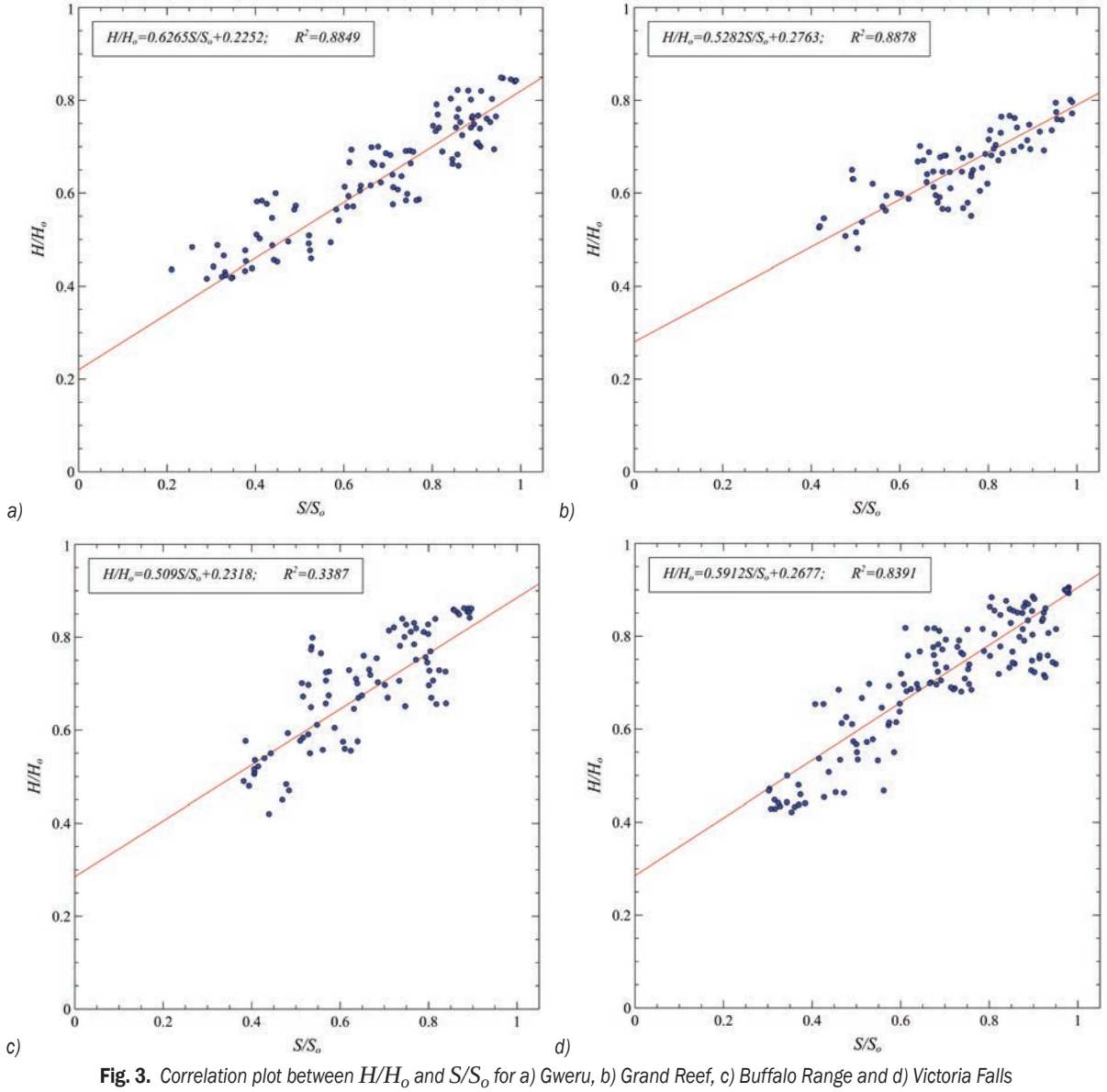

Fig. 3. *Correlation plot between H/H_o and S/S_o for a) Gweru, b) Grand Reef, c) Buffalo Range and d) Victoria Falls*

Table 5. *The variation of the annual A-P coefficients with meteorological and climatic variables*

Station	Latitude [°]	Longitude [°]	Elevation [m]	S/S_o	H/H_o	a	b
Beitbridge	22.22	29 .99	457.00	0.7135	0.6380	0.2977	0.4770
Grand Reef	18.98	32.45	1019.00	0.6878	0.6529	0.2763	0.5282
Gweru	19.45	29 .85	1429 .00	0.7001	0.6638	0.2252	0.6265
Kutsaga	17.92	31.13	1480.00	0.6996	0.6152	0.2855	0.4707
Mt Darwin	16.78	31.58	953.00	0.6900	0.6383	0.3066	0.4807
Nyanga	18.22	32.75	1679.00	0.6458	0.6288	0.2362	0.6080
Victoria Falls	17.93	25.85	1062.00	0.7494	0.7107	0.2677	0.5912

Note. H/H_o, is the clearness index, S/S_o, is the sunshine duration fraction, a and b, are the A-P regression coefficients.

increasing, S, and S/S_o, as expected for each station. Solar radiation received increases with increase in sunshine duration and the quantities can be attributed to the type of Koppen-Geiger climate classification of each location station [27]. The highest correlation between the clearness index and the sunshine duration fraction was 0.9030 as shown in Table 2 with 80 % of the stations having R^2, greater than 0.6. The lowest, R^2, is 0.3387 for Buffalo Range station in Chiredzi which can be considered a weak correlation, as it is evident by dispersed data showing a weak relationship between, H/H_o, and S/S_o, as shown in Fig. 3c.

2.4 A-P Regression Coefficients

In Tables 2, 3 and 4 it can be observed that both, a and b, are higher in the winter months of May to August and are lower in the summer and wet months of October to March. This can be attributed to the clear sky conditions during the winter and cloudy skies experienced in the summer in Zimbabwe. The plots in Fig. *3*, as well as Tables 2, 3 and 4 show the annual A-P type regression coefficients, *a* and *b*, which are the gradient and y-intercepts respectively for all the stations under study. The correlation coefficient, *a*, ranged from 0.2252 at Gweru Meteorological Station to 0.3976 at Chisengu Meteorological Station and the correlation coefficient, *b*, ranged from 0.3218 at Banket Meteorological Station to 0.6265 at Gweru Meteorological Station.

Table 5, shows the variations of regression coefficients, *a* and *b*, with respect to latitude, longitude, elevation, S/S_o and H/H_o. It can be seen that both the regression coefficient, *a* and *b*, do not possess a salient relationship with the variables particularly latitude and elevation. The above trends were also observed in other similar studies [49], [51], [91] and [92], where the outcomes showed that neither *a* nor *b*, varied with latitude and altitude in any systematic manner. This can be attributed to the lack of distribution between the stations across the whole Zimbabwe as the bulk of the stations are located in the North-Western and Western part of the country.

However there is a slight effect on both, *a* and *b*, with respect to the longitude. The value of, *a*, tends to reduce as the longitude increases, whilst the value of, *b*, increases with increase in longitude as shown in Table 5. This implies that the values of, *a*, are higher in the western parts of the country as seen in the stations like Victoria Falls (a = 0.2677, b = 0.5912) and Binga (a = 0.3222, b = 0.4795) and lower in the eastern parts in stations like Nyanga (a = 0.2362, b = 0.6080) and Mukandi (a = 0.2100, b = 0.5340) and vice versa for the values of *b*. Therefore, it can be assumed that the values of a and *b* at a location are dominantly affected by the climatic condition of the area. Particularly in Zimbabwe it can be observed that areas with semi-arid climates have high values of *a*, than those areas with a subtropical climate and vice versa for the values of *b*. Nwokolo et al. [27] deduced similar conclusions from a similar research, whereby the stations that are within the hot desert and the warm semi-arid climates of Nigeria showed higher coefficients of *a*, between 0.350 and 0.469 compared to the station that are within the tropical savannah and the tropical rainforest climates with *a*, values between 0.212 and 0.268. Nwokolo et al. [27] also obtained values of the A-P coefficient *b*, which increased from stations within the hot (arid) desert climate to those in the tropical rainforest climate.

The A-P type models for various areas in Zimbabwe based on individual station are shown in table 6. It can be observed that a few stations like Banket (a = 0.3356, b = 0.3218), Chisengu (a = 0.3306, b = 0.3333) and Triangle (a = 0.3223, b = 0.3287) exhibited values of *a* and *b*, that are off trend with a very small difference between the *a* and *b*, values. This can be attributed to the use of only satellite-based solar radiation data for these stations which had slightly higher values than ground-measured values used in other stations. The coefficient *a*, from literature indicates the proportion of H_o,

received on the surface on a very cloudy day when $S/S_o = 0$, whilst $a + b$, indicate the proportion of H_o, on a clear sky day when $S/S_o = 1$ [27]. This indicates that the higher intensity of H, received the greater the value of a, and the less the value of b. The variations mentioned above were also obtained by [28] and [87] in similar researches where both satellite and ground data were used interchangeably and the implication of these findings in both cases reduced the predicting power of the models slightly. In the case of [28] the predicting power of the models based on satellite data was reduced by 1.48 %.

The A-P type models obtained in table 5 show similarities in the regression coefficients of a and b, for stations in close proximity like MSD Belvedere with $a = 0.2886$ and $b = 0.4635$ and Kutsaga with $a = 0.2855$ and $b = 0.4707$ all located in Harare. The above regression coefficients for the stations based in Harare also showed similarities with the coefficients obtained by [52] for Harare with $a = 0.282$ and $b = 0.460$. Hove and Göttsche [74] also obtained similar coefficients for Gokwe and West Nicholson as ($a = 0.36$, $b = 0.47$) and ($a = 0.29$, $b = 0.49$) respectively as shown in Table 5.

2.5 Estimated Solar Radiation Values

The models in Table 6 were used to estimate monthly solar radiation values H_e, for each station and the values were compared to the monthly measured and extra-terrestrial solar radiation from individual stations H_{grn} and H_o respectively. Monthly H_e and H_{grn}, were plotted and a selected plot for Nyanga is shown in Fig. 4.

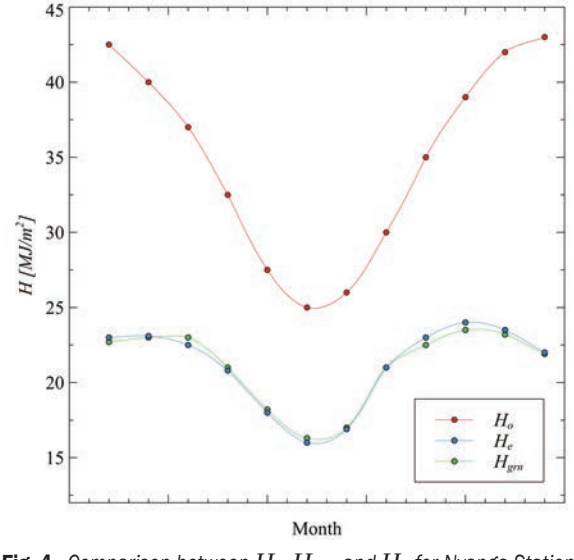

Fig. 4. *Comparison between H_e, H_{grn} and H_o for Nyanga Station*

The extra-terrestrial solar radiation H_o, maintained a similar trend in all the stations as shown in Fig. 4 with a steep U-shaped plot. H_o ranged between 23 MJ/m² and 44 MJ/m², with the lowest values observed in the months of June, July and August (winter season), and the highest in the months of October, November, December and January (summer season). In Fig. 4, it can be seen that both the estimated and measured monthly solar radiation values follow the same trend as the monthly Extra-terrestrial solar radiation values but with a gentle U-shaped slope which drops from the month of March to July and rises from August to October and drops slightly from November to December. In Zimbabwe the months of June and July are the coldest months, with August being windy and while the month of October is the hottest. The months of November, December and March are the wettest months and all these variations related to altitude [62]. H_e and H_{grn}, had values ranging between 12 MJ/m² and 27 MJ/m², with the lowest values observed in the months of June and July, and the highest in the month of October.

The slight drop in magnitude of the measured and estimated solar radiation values from the months of October to December can be attributed to effect of rain, with the rain season beginning in late October or early November [62]. Observing the values of both extra-terrestrial and measured global horizontal solar irradiation it can be concluded that just above 50 % of the extra-terrestrial solar irradiation from the sun is received on the ground and this can be attributed mostly to the effect of the atmosphere. The trends observed in Fig 4. are similar to the trends observed in other studies in countries surrounding Zimbabwe [82] and [92] to [94] in Mozambique, South Africa, South Africa and Malawi respectively. The estimated values H_e, show very small variations from the measured values H_{grn}, in most of the stations, except for Buffalo Range which exhibit slightly higher variations.

The estimated values H_e, for the general model were compared to ground measured values, H_{grn}, and extra-terrestrial H_o, solar radiation values from individual stations to assess the deviation from the measured values. It was noted that the general model estimated values, H_e, maintained the same trend as H_{grn}, for all the stations. Slight deviations between, H_e and H_{grn}, can however be observed in a few stations such as Banket, Chisumbanje, Chivhu, Gokwe, Kariba and Triangle. These slight deviations are attributed to the input solar radiation data used from these stations, which was ground corresponding values based on satellite measurements only.

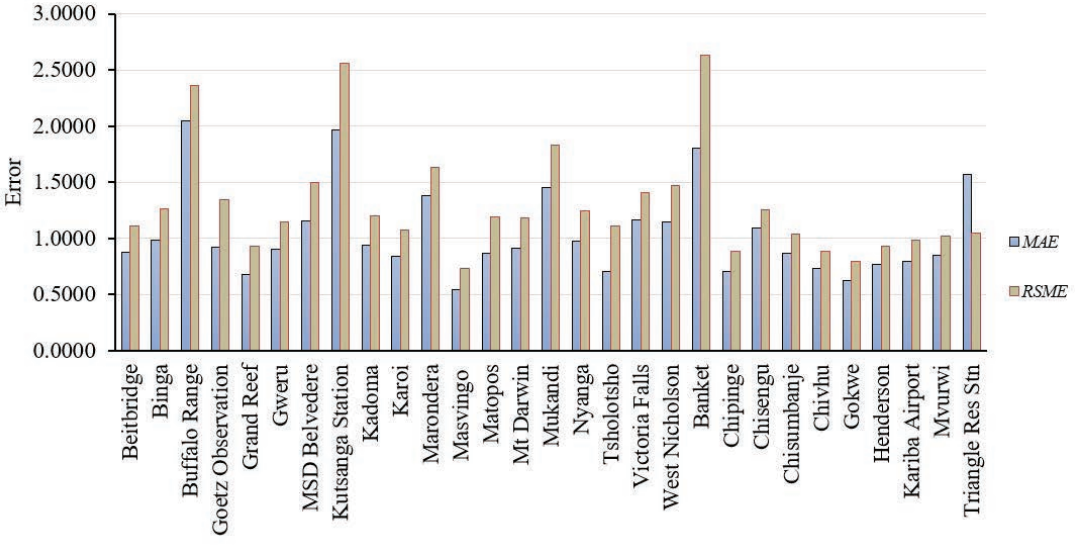

Fig. 5. *The MAE and RSME for each station*

Table 6. *A-P Type Models for each station*

Station	Model	Station	Model
Beitbridge	$H/H_o = 0.2977 + 0.4770\ S/S_o$	Nyanga	$H/H_o = 0.2362 + 0.6080\ S/S_o$
Binga	$H/H_o = 0.3222 + 0.4795\ S/S_o$	Tsholotsho	$H/H_o = 0.2389 + 0.5307\ S/S_o$
Buffalo Range	$H/H_o = 0.2763 + 0.5090\ S/S_o$	Victoria Falls	$H/H_o = 0.2677 + 0.5912\ S/S_o$
Goetz Obs	$H/H_o = 0.2808 + 0.4670\ S/S_o$	West Nicholson	$H/H_o = 0.2931 + 0.5003\ S/S_o$
Gweru	$H/H_o = 0.2252 + 0.6265\ S/S_o$	Chisengu	$H/H_o = 0.3306 + 0.3333\ S/S_o$
MSD Belvedere	$H/H_o = 0.2886 + 0.4635\ S/S_o$	Chipinge	$H/H_o = 0.3976 + 0.4866\ S/S_o$
Kutsaga	$H/H_o = 0.2855 + 0.4707\ S/S_o$	Chisumbanje	$H/H_o = 0.2559 + 0.4206\ S/S_o$
Kadoma	$H/H_o = 0.2785 + 0.5099\ S/S_o$	Chivhu	$H/H_o = 0.3479 + 0.5108\ S/S_o$
Karoi	$H/H_o = 0.3041 + 0.0569\ S/S_o$	Gokwe	$H/H_o = 0.3634 + 0.4864\ S/S_o$
Marondera	$H/H_o = 0.2658 + 0.5605\ S/S_o$	Henderson	$H/H_o = 0.3723 + 0.4923\ S/S_o$
Masvingo	$H/H_o = 0.2743 + 0.5054\ S/S_o$	Kariba Airport	$H/H_o = 0.3147 + 0.3244\ S/S_o$
Matopos	$H/H_o = 0.2562 + 0.5298\ S/S_o$	Mvurwi	$H/H_o = 0.3871 + 0.4667\ S/S_o$
Mt Darwin	$H/H_o = 0.3066 + 0.4807\ S/S_o$	Triangle	$H/H_o = 0.3223 + 0.3287\ S/S_o$
Mukandi	$H/H_o = 0.3100 + 0.5340\ S/S_o$	Harare	$H/H_o = 0.2820 + 0.4600\ S/S_o$

Note. The correlation coefficients, a and b, are the gradient and y-intercepts respectively.

2.6 Statistical Evaluation of the Models

The estimated and measured values of global solar radiation H_e and H_{grn}, respectively from each station were compared using statistical analysis methods in order to evaluate each model's potential to predict solar irradiation. The analytical methods used to evaluate the models were the *MAPE*, *RMSE*, *MAE RSE* and the results are shown in Table 7.

The *MAE* values for each model range from 0.5438 MJ/m² to 2.2845 MJ/m². The small values of *MAE* between the measured and estimated solar radiation values indicate very good long-term prediction capabilities of the models. The *MAPE* indicate a range between 2.5642 % and 10.3343 %. It was noted that only Buffalo Range Station out of the 29 stations had a *MAPE* greater than 10 % and this can be attributed to the low correlation coefficients value between the clearness index and the sunshine duration fraction expressed by the station. The low correlation coefficient was due to inaccurate sunshine duration data for the station obtained from MSD, which was mainly due to faulty measuring instruments. The rest of the stations indicated *MAPE* between estimated and measured solar radiation values to be lower than 10

%, hence showing very high predicting abilities as observed in other studies **[17]**, **[82]** and **[88]**.

Table 7. *Results of the Statistical evaluation of the A-P type models*

Station	R^2	*MAE* [MJ/m²]	*MAPE* [%]	*RMSE* [MJ/m²]	*RSE* [%]
Beitbridge	0.9154	0.8792	4.1974	1.1095	0.0528
Grand Reef	0.9329	0.6830	3.1807	0.9280	0.0425
Gweru	0.8793	0.8994	3.9684	1.1446	0.0501
Mt Darwin	0.8707	0.9106	4.229 0	1.1787	0.0549
Nyanga	0.8782	0.9789	4.6161	1.2444	0.0582
Victoria Falls	0.7612	1.1629	4.8627	1.4034	0.0583

The *RSE* for the models was found to be between 0.0346 % and 0.1537% showing very low values of the standard error relative to the estimated values, hence indicating high degrees of accuracy of estimation correlations in the models similar to values of *RSE* found in other studies by **[26]** and **[84]**. The *RMSE* for the models ranged from 0.7360 MJ/m² to 2.9454 MJ/m² and these values are within the recommended range for excellent solar predicting models from other similar studies **[51]** and **[89]**, hence indicating good short-term predicting capabilities for all the models. As shown in Fig. 5., Masvingo Station exhibited very low values of *MAE*, *MPE*, *RSE* and *RMSE* which can be attributed to the high correlation coefficient of r = 0.9531 between the estimated and measured solar radiation values. Triangle station in Chiredzi exhibited the highest values of *MAE*, *MPE*, *RSE*, *RMSE* and a low coefficient of determination R^2 = 0.6062 between the estimated and measured values of solar radiation.

The results of the statistical analysis for the general model which were compared to the results for the individual station-based models show very slight changes for *MAE*, *MAPE*, *RMSE* and *RSE* in most of the stations. This confirms the high predicting capabilities of the general model. Significant changes can be observed under *MAPE* statistical analysis particularly for the stations with satellite-based solar radiation data, but however the changes still remained within the required limit of 0 % < *MAPE* < 10 %.

3 CONCLUSION

The main aim of this study was to develop a general A-P type model for predicting solar irradiation in Zimbabwe. In the process of predicting solar irradiation using empirical coefficients, sunshine duration was deemed to have the greatest impact on the amount of solar radiation received on a horizontal surface.

The following notable results were reported.

- The highest correlation between the clearness index and the sunshine duration fraction was 0.9030 with 80 % of the coefficients of determination above 0.6.
- The results of the study showed no systematic trend between the regression coefficients with both latitude and elevation, however the value of, *a*, decreased as the longitude increases, whilst the value of, *b*, increased with increase in longitude, hence the values of, *a*, were higher in the western parts of the country and lower in the eastern parts and vice versa for the values of, *b*, and these results agreed with other results from similar researches.
- The *MAE* values for the models ranged from 0.5438 MJ/m² to 2.2845 MJ/m². The *MAPE* indicated a range between 2.5642 % and 10.334 % with only Buffalo Range Station having a *MAPE* greater than 10 % which was caused by a faulty sunshine recorder. The rest of the stations indicated *MAPE* values lower than 10 %, hence showing very high predicting abilities.
- The values of the regression coefficients, *a* and *b*, at a location are dominantly affected by the climatic condition of the area and that the more specific the coefficients are to a location the more accurate they become.
- Also, the general model developed in this study is considered to have good solar prediction abilities as proven by statistical results that are within the recommended range.
- The developed models can provide estimated solar irradiation data that is currently not available in the meteorological stations in Zimbabwe, hence filling the gap in terms of solar radiation data availability.

4 REFERENCES

[1] Syed, A., Raza, T., Bhatti, T.T., Eash, N.S. (2022). Climate impacts on the agricultural sector of Pakistan: Risks and solutions. *Environmental Challenge*s, vol. 6, art. ID 100433, **DOI:10.1016/j.envc.2021.100433**.

[2] Patel, R.V., Yadav, A., Winczek, J.A. (2021). Experimental Investigation and mathematical modelling of heat transfer coefficient in double slope solar still. *Strojniški vestnik - Journal of Mechanical Engineering*, vol. 67, no. 7-8, p. 369-379, **DOI:10.5545/sv-jme.2021.7156**.

[3] Leal Filho, W., Wall, T., Rui Mucova, S.A., Nagy, G.J., Balogun, A.-L., Luetz, J.M., Ng, A.W., Kovaleva, M., Safiul Azam, F.M., Alves, F., Guevara, Z., Matandirotya, N.R., Skouloudis, A., Tzachor, A., Malakar, K., Gandhi, O. (2022). Deploying artificial intelligence for climate change adaptation. *Technological*

Forecasting and Social Change, vol. 180, art. ID 121662, **DOI:10.1016/j.techfore.2022.121662**.

[4] Taghavipour, A., Alipour, A. (2021). HIL Evaluation of a novel real-time energy management system for an HEV with a continuously variable transmission. *Strojniški vestnik - Journal of Mechanical Engineering*, vol. 67, no. 4, p. 142-152, **DOI:10.5545/sv-jme.2020.7017**.

[5] Hargrove, A., Qandeel, M., Sommer, J.M. (2019). Global governance for climate justice: A cross-national analysis of CO_2 emissions. *Global Transitions*, vol. 1, p. 190-199, **DOI:10.1016/j.glt.2019.11.001**.

[6] New, M., Liverman, D., Schroder, H., Anderson, K. (2011). Four degrees and beyond: the potential for a global temperature increase of four degrees and its implications. *Philosophical Transaction of the Royal Society A*, vol. 369, no. 1934, p. 6-19, **DOI:10.1098/rsta.2010.0351**.

[7] Rhodes, C.J. (2019) Only 12 years left to readjust for the 1.5-degree climate change option - Says International Panel on Climate Change report: Current commentary. *Science Progress*, vol. 102, no. 1, p. 73-87, **DOI:10.1177/0036850418823397**.

[8] Bayrakçı, H.C., Demircan, C., Keçebaş, A. (2018). The development of empirical models for estimating global solar radiation on horizontal surface: A case study. *Renewable and Sustainable Energy Reviews*, vol. 81, p. 2771-2782, **DOI:10.1016/j.rser.2017.06.082**.

[9] Holechek, J.L., Geli, H.M.E., Sawalhah, M.N., Valdez, R. (2022). A global assessment: Can Renewable energy replace fossil fuels by 2050? *Sustainability*, vol. 14, no. 8, art. ID 4792, **DOI:10.3390/su14084792**.

[10] Tierney, S., Bird, L. (2020). *Setting the Record Straight About Renewable Energy*. World Resurce Institute, Washington.

[11] Felix, P.G., Rajagopal, V., Kumaresan, K. (2021). Applicability of MCDM algorithms for the selection of phase change materials for thermal energy storage heat exchangers. *Strojniški vestnik - Journal of Mechanical Engineering*, vol. 67, no. 11, p. 611-622, **DOI:10.5545/sv-jme.2021.7356**.

[12] Kittusamy, R.K., Rajagopal, V., Felix, P.G. (2022). Preparation and thermal characterization of nanographene- enhanced fatty acid-based solid-liquid organic phase change material composites for thermal energy storage. *Strojniški vestnik - Journal of Mechanical Engineering*, vol. 68, no. 7-8, p. 461-470, **DOI:10.5545/sv-jme.2022.148**.

[13] Bouchouicha, K., Hassan, M.A., Bailek, N., Aoun, N. (2019). Estimating the global solar irradiation and optimizing the error estimates under Algerian desert climate. *Renewable Energy*, vol. 139, p. 844-858, **DOI:10.1016/j.renene.2019.02.071**.

[14] Nunez Munoz, M., Ballantyne, E.E.F., Stone, D.A. (2022). Development and evaluation of empirical models for the estimation of hourly horizontal diffuse solar irradiance in the United Kingdom. *Energy*, vol. 241, art. ID 122820, **DOI:10.1016/j.energy.2021.122820**.

[15] Mohamad, N.B., Lai, A.-C., Lim, B.-H. (2022). A case study in the tropical region to evaluate univariate imputation methods for solar irradiance data with different weather types. *Sustainable Energy Technologies and Assessments*, vol. 50, art. ID 101764, **DOI:10.1016/j.seta.2021.101764**.

[16] AlKandari, M., Ahmad, I. (2020). Solar power generation forecasting using ensemble approach based on deep learning and statistical methods. *Applied Computing and Informatics, (ahead-of-print)*, **DOI:10.1016/j.aci.2019.11.002**.

[17] Djoman, M.A., Fassinou, W.F., Memeledje, A. (2021). Calibration of Ångström-Prescott coefficients to estimate global solar radiation in Côte d'Ivoire. *European Scientific Journal*, vol. 17, no. 37, p. 24-38, **DOI:10.19044/esj.2021.v17n37p24**.

[18] Jebli, I., Belouadha, F.-Z., Kabbaj, M.I., Tilioua, A. (2021) Prediction of solar energy guided by pearson correlation using machine learning. *Energy*, vol. 224, art. ID 120109, **DOI:10.1016/j.energy.2021.120109**.

[19] Wang, Y., Feng, B., Hua, Q.-S., Sun, L. (2021). Short-term solar power forecasting: A combined long short-term memory and Gaussian process regression method. *Sustainability*, vol. 13, no. 7, art. ID 3665, **DOI:10.3390/su13073665**.

[20] Ye, H., Yang, B., Han, Y., Chen, N. (2022). State-of-the-art solar energy forecasting approaches: Critical potentials and challenges. *Frontiers in Energy Research*, vol. 10, **DOI:10.3389/fenrg.2022.875790**.

[21] Nwokolo, S.C., Ogbulezie, J.C., Obiwulu, A.U. (2022). Impacts of climate change and meteo-solar parameters on photosynthetically active radiation prediction using hybrid machine learning with Physics-based models. *Advances in Space Research*, vol. 70, no. 11, p. 3614-3637, **DOI:10.1016/j.asr.2022.08.010**.

[22] Nwokolo, S.C., Obiwulu, A.U., Ogbulezie, J.C., Amadi, S.O. (2022). Hybridization of statistical machine learning and numerical models for improving beam, diffuse and global solar radiation prediction. *Cleaner Engineering and Technology*, vol. 9, art. ID 100529, **DOI:10.1016/j.clet.2022.100529**.

[23] Obiwulu, A.U., Erusiafe, N., Olopade, M.A., Nwokolo, S.C. (2022). Modeling and estimation of the optimal tilt angle, maximum incident solar radiation, and global radiation index of the photovoltaic system. *Heliyon*, vol. 8, no. 6, art. ID e09598, **DOI:10.1016/j.heliyon.2022.e09598**.

[24] Keshtegar, B., Bouchouicha, K., Bailek, N., Hassan, M.A., Kolahchi, R., Despotovic, M. (2022). Solar irradiance short-term prediction under meteorological uncertainties: survey hybrid artificial intelligent basis music-inspired optimization models. *The European Physical Journal Plus*, vol. 137, art. ID 362, **DOI:10.1140/epjp/s13360-022-02371-w**.

[25] Arslanoglu, N. (2022). Development of empirical models for estimation diffuse solar radiation exergy in Turkey. *Internarional Journal of Exergy*, vol. 37 no. 1, p. 24-39, **DOI:10.1504/IJEX.2022.120106**.

[26] Lare, Y., Sambiani, K., Amega, K., Kabe, M. (2021). Modeling of the global daily horizontal solar radiation data over Togo. *Energy and Power Engineering*, vol. 13, no. 12, p. 403-412, **DOI:10.4236/epe.2021.1312028**.

[27] Nwokolo, S.C., Amadi, S.O., Obiwulu, A.U., Ogbulezie, J.C., Eyibio, E.E. (2022). Prediction of global solar radiation potential for sustainable and cleaner energy generation using improved Angstrom-Prescott and Gumbel probabilistic models. *Cleaner Engineering and Technology*, vol. 6, art. ID 100416, **DOI:10.1016/j.clet.2022.100416**.

[28] Oyewola, O.M., Patchali, T.E., Ajide, O.O., Singh, S., Matthew, O.J. (2022). Global solar radiation predictions in Fiji Islands

based on empirical models. *Alexandria Engineering Journal*, vol. 61, no. 11, p. 8555-8571, **DOI:10.1016/j.aej.2022.01.065**.

[29] Caycedo Villalobos, L.A., Cortázar Forero, R.A., Cano Perdomo, P.M., González Veloza, J.J.F. (2021). Solar radiation prediction using machine learning techniques. *Applied Informatics*, vol. 1455, Springer International Publishing, Cham, p. 68-81, **DOI:10.1007/978-3-030-89654-6_6**.

[30] Deo, R.C., Şahin, M. (2017). Forecasting long-term global solar radiation with an ANN algorithm coupled with satellite-derived (MODIS) land surface temperature (LST) for regional locations in Queensland. *Renewable and Sustainable Energy Reviews*, vol. 72, p. 828-848, **DOI:10.1016/j.rser.2017.01.114**.

[31] Khatib, T., Mohamed, A., Sopian, K., Mahmoud, M. (2012). Solar energy prediction for malaysia using artificial neural networks. *International Journal of Photoenergy*, vol. 2012, art. ID 419504, **DOI:10.1155/2012/419504**.

[32] Kim, Y.S., Joo, H.Y., Kim, J.W., Jeong, S.Y., Moon, J.H. (2021). Use of a big data analysis in regression of solar power generation on meteorological variables for a Korean solar power plant. *Applied Sciences*, vol. 11, no. 4, art. ID 1776, **DOI:10.3390/app11041776**.

[33] Kor, H. (2021). Global solar radiation prediction model with random forest algorithm. *Thermal Science*, vol. 25, spec.issue 1, p. 31-39, **DOI:10.2298/TSCI200608004K**.

[34] Zhang, X., Zhang, M., Cui, Y., He, Y. (2022). Estimation of Daily ground-received global solar radiation using air pollutant data. *Frontiers in Public Health*, vol. 10, **DOI:10.3389/fpubh.2022.860107**.

[35] Sabbagh, J.A., Sayigh, A.A.M., El-Salam, E.M.A. (1977). Estimation of the total solar radiation from meteorological data. *Solar Energy*, vol. 19, no. 3, p. 307-311, **DOI:10.1016/0038-092X(77)90075-5**.

[36] Kasten, F., Czeplak, G. (1980). Solar and terrestrial radiation dependent on the amount and type of cloud. *Solar Energy*, vol. 24, no. 2, p. 177-189, **DOI:10.1016/0038-092X(80)90391-6**.

[37] Nwokolo, S.C. (2017). A comprehensive review of empirical models for estimating global solar radiation in Africa. *Renewable and Sustainable Energy Reviews*, vol. 78, p. 955-995, **DOI:10.1016/j.rser.2017.04.101**.

[38] Nwokolo, S.C., Ogbulezie, J.C. (2018). A quantitative review and classification of empirical models for predicting global solar radiation in West Africa. *Beni-Suef University Journal of Basic and Applied Sciences*, vol. 7, no. 4, p. 367-396, **DOI:10.1016/j.bjbas.2017.05.001**.

[39] Bautista-Rodrigez, G.M., Chacón-Cardona, C.A. (2021). Ångström-Prescott models of solar radiation over Earth surface. *Journal of Physics: Conference Series*, vol. 2135, art. ID 012005, **DOI:10.1088/1742-6596/2135/1/012005**.

[40] Bristow, K.L., Campbell, G.S. (1984). On the relationship between incoming solar radiation and daily maximum and minimum temperature. *Agricultural and Forest Meteorology*, vol. 31, no. 2, p. 159-166, **DOI:10.1016/0168-1923(84)90017-0**.

[41] Donatelli, M., Campbell, G.S. (1998). A simple model to estimate global solar radiation. *Proceedings of the 5th European Society of Agronomy Congress*, vol. 2, p. 133-134.

[42] Nwokolo, S.C., Ogbulezie, J. (2017). A single hybrid parameter-based model for calibrating hargreaves-samani coefficient in Nigeria. *International Journal of Physical Research*, vol. 5, no. 2, p. 49-59, **DOI:10.14419/ijpr.v5i2.8042**.

[43] Woldegiyorgis, T.A., Admasu, A., Benti, N.E., Asfaw, A.A. (2022). A comparative evaluation of artificial neural network and sunshine based models in prediction of daily global solar radiation of Lalibela, Ethiopia. *Cogent Engineering*, vol. 9, no. 1, art. ID 1996871, **DOI:10.1080/23311916.2021.1996871**.

[44] Glover, J., McCulloch, J.S.G. (1958). The empirical relation between solar radiation and hours of bright sunshine in the high-altitude tropics. *Quarterly Journal of the Royal Meteorological Society*, vol. 84, no. 359, p. 56-60, **DOI:10.1002/qj.49708435907**.

[45] Page, J.K. (1961). The estimation of monthly mean values of daily total short wave radiation on vertical and inclined surfaces from sunshine records for latitudes 40N-40S. *UN Conference on New Sources of Energy*.

[46] Abramczyk, J. (2022). Parametric building forms rationalizing the incident direct solar irradiation. *Building and Environment*, vol. 215, art. ID 108963, **DOI:10.1016/j.buildenv.2022.108963**.

[47] Sankarayogi, P., Annareddy, R.R., Awasthi, A., Gugamsetty, B., Pulla, S.N., Yadiki, N.A. (2022). Estimation of monthly mean global solar radiation over semi-arid region, Kadapa using meteorological parameter. *Preprint at Research Square*, **DOI:10.21203/rs.3.rs-1227717/v1**.

[48] Bahel, V., Bakhsh, H., Srinivasan, R. (1987). A correlation for estimation of global solar radiation. *Energy*, vol. 12, no. 2, p. 131-135, **DOI:10.1016/0360-5442(87)90117-4**.

[49] Dehkordi, S.N., Bakhtiari, B., Qaderi, K., Ahmadi, M.M. (2022). Calibration and validation of the Angstrom-Prescott model in solar radiation estimation using optimization algorithms. *Scientific Reports*, vol. 12, art. ID 4855, **DOI:10.1038/s41598-022-08744-6**.

[50] Mostafazadeh, S., Behmanesh, J., and Rezaverdinejad, V. (2022). Evaluating the effect of the atmospheric pollutants on the received solar radiation by ground surface using Angstrom-Prescott model (Case study: Urmia and Tabriz). *Water and Soil Science*, vol. 32, no. 1, p. 15-26.

[51] Mejia, J.R.R., Prieto, A.W., Chávez, A.V., Varela, R.V., López Monteagudo, F.E., Rivas, C.R. (2022). Estimation of solar radiation in Northwest Mexico based on the Angstrom model and polynomial regression. *Ingeniería Energética*, vol. 43, no. 1, p. 35-47.

[52] Lewis, G. (1983). Estimates of irradiance over Zimbabwe. *Solar Energy*, vol. 31, no. 6, p. 609-612, **DOI:10.1016/0038-092X(83)90177-9**.

[53] Swartman, R.K., Ogunlade, O. (1967). Solar radiation estimates from common parameters. *Solar Energy*, vol. 11, no. 3, p. 170-172, **DOI:10.1016/0038-092X(67)90026-6**.

[54] Chagwedera, S.M., Sendezera, E.J. (1991). Prediction of global solar radiation at two locations in Zimbabwe: a comparative analysis of three Ångstrom-type equations. *Renewable Energy*, vol. 1, no. 5, p. 811-814, **DOI:10.1016/0960-1481(91)90031-J**.

[55] Chiteka, K., Enweremadu, C.C. (2016). Prediction of global horizontal solar irradiance in Zimbabwe using artificial neural networks. *Journal of Cleaner Production*, vol. 135, p. 701-711, **DOI:10.1016/j.jclepro.2016.06.128**.

[56] Hoyos-Gómez, L.S., Ruiz-Muñoz, J.F., Ruiz-Mendoza, B.J. (2022). Short-term forecasting of global solar irradiance in tropical environments with incomplete data. *Applied Energy*, vol. 307, art. ID 118192, **DOI:10.1016/j.apenergy.2021.118192**.

[57] Dhass, A.D., Patel, D.R. (2022). thermodynamic analysis of reflected solar radiation on tilted PV module in South India. *FME Transactions*, vol. 50 no. 1, p. 158-167, **DOI:10.5937/fme2201158D**.

[58] Chanza, N., Musakwa, W. (2022). Indigenous local observations and experiences can give useful indicators of climate change in data-deficient regions. *Journal of Environmental Studies and Sciences*, vol. 12, p. 534-546, **DOI:10.1007/s13412-022-00757-x**.

[59] Sarr, A., Kebe, C.M.F., Ndiaye, A. (2022). Validation of Helioclim-3 irradiance with ground observations in Senegal using four typical climatic zones. *Materials Today: Proceedings*, vol. 51, p. 1888-1895, **DOI:10.1016/j.matpr.2022.01.164**.

[60] Cai, H., Qin, W., Wang, L., Hu, B., Zhang, M. (2021). Hourly clear-sky solar irradiance estimation in China: Model review and validations. *Solar Energy*, vol. 226, p. 468-482, **DOI:10.1016/j.solener.2021.08.066**.

[61] Paul, D., De Michele, G., Najafi, B., Avesani, S. (2022). Benchmarking clear sky and transposition models for solar irradiance estimation on vertical planes to facilitate glazed facade design. *Energy and Buildings*, vol. 255, art. ID 111622, **DOI:10.1016/j.enbuild.2021.111622**.

[62] Bailey, M., Heinrich, D., Kruczkiewicz, A. (2021). *Climate Profiles of Countries in Southern Africa: Zimbabwe*. Red Cross Climate Centre, RCRC, The Hague.

[63] Ingham, K., Sanger, C.W., Bradley, K. (2020). Zimbabwe. Encyclopedia Britannica, from *https://www.britannica.com/place/Zimbabwe,* accessed on 2022-08-17.

[64] POWER. Data Access Viewer. From *https://power.larc.nasa.gov/data-access-viewer/,* accessed on 2021-10-07.

[65] Rienecker, M.M., Suarez, M.J., Gelaro, R., Todling, R., Bacmeister, J., Liu, E., Bosilovich, M.G., Schubert, S.D., Takacs, L., Kim, G.-K., Bloom, S., Chen, J., Collins, D., Conaty, A., Silva, A. da, Gu, W., Joiner, J., Koster, R.D., Lucchesi, R., Molod, A., Owens, T., Pawson, S., Pegion, P., Redder, C.R., Reichle, R., Robertson, F.R., Ruddick, A.G., Sienkiewicz, M., Woollen, J. (2011). MERRA: NASA's Modern-Era Retrospective Analysis for Research and Applications. *Journal of Climate*, vol. 24, no. 14, p. 3624-3648, **DOI:10.1175/JCLI-D-11-00015.1**.

[66] Westberg, D.J., Paul W. Stackhouse, J., Crawley, D.B., Hoell, J.M., Chandler, W.S., Zhang, T. (2013). An analysis of NASA's MERRA meteorological data to supplement observational data for calculation of climatic design conditions. *ASHRAE Transactions*, vol. 119, no. 2, p. 210-222.

[67] Ghazouani, N., Bawadekji, A., El-Bary, A.A., Elewa, M.M., Becheikh, N., Alassaf, Y., Hassan, G.E. (2022). Performance evaluation of temperature-based global solar radiation models-case study: Arar city, KSA. *Sustainability*, vol. 14, no. 1, art. ID 35, **DOI:10.3390/su14010035**.

[68] Shrestha, G.K., Pandey, B., Joshi, U., Poudyal, K.N. (2021). Empirical model for estimation of global solar radiation at lowland region Biratnagar using satellite data. *BIBECHANA*, vol. 18, no. 1, p. 193-200, **DOI:10.3126/bibechana.v18i1.29689**.

[69] Cebecauer, T., Suri, M. (2016). Site-adaptation of satellite-based DNI and GHI time series: Overview and SolarGIS approach. *AIP Conference Proceedings*, vol. 1734, no. 1, art. ID 150002, **DOI:10.1063/1.4949234**.

[70] Fazelpour, F., Vafaeipour, M., Rahbari, O., Valizadeh, M.H. (2013). Assessment of solar radiation potential for different cities in Iran using a temperature-based method. *Sustainability in Energy and Buildings*, p. 199-208, **DOI:10.1007/978-3-642-36645-1_19**.

[71] Verhoelst, T., Granville, J., Hendrick, F., Köhler, U., Lerot, C., Pommereau, J.-P., Redondas, A., Van Roozendael, M., Lambert, J.-C. (2015) Metrology of ground-based satellite validation: co-location mismatch and smoothing issues of total ozone comparisons. *Atmospheric Measurement Techniques*, vol. 8, no. 12, p. 5039-5062, **DOI:10.5194/amt-8-5039-2015**.

[72] Zelenka, A., Perez, R., Seals, R., Renné, D. (1999). Effective accuracy of satellite-derived hourly irradiances. *Theoretical and Applied Climatology*, vol. 62, no. 3, p. 199-207, **DOI:10.1007/s007040050084**.

[73] Hove, T., Manyumbu, E., Rukweza, G. (2014). Developing an improved global solar radiation map for Zimbabwe through correlating long-term ground- and satellite-based monthly clearness index values. *Renewable Energy*, vol. 63, p. 687-697, **DOI:10.1016/j.renene.2013.10.032**.

[74] Hove, T., Göttsche, J. (1999). Mapping global, diffuse and beam solar radiation over Zimbabwe. *Renewable Energy*, vol. 18, no. 4, p. 535-556, **DOI:10.1016/S0960-1481(98)00782-4**.

[75] Yeom, J.-M., Seo, Y.-K., Kim, D.-S., Han, K.-S. (2016). Solar radiation received by slopes using COMS imagery, a physically based radiation model, and GLOBE. *Journal of Sensors*, vol. 2016, art. ID e4834579, **DOI:10.1155/2016/4834579**.

[76] Duffie, J.A., Beckman, W.A. (2013). *Solar Engineering of Thermal Processes*, John Wiley & Sons, Hoboken, **DOI:DOI:10.1002/9781118671603**.

[77] Gören, D., Taylan, O. (2020). Quality assessment of on-site solar radiation data and estimating global tilted irradiation in Middle East Technical University Northern Cyprus Campus. *2nd International Conference on Photovoltaic Science and Technologies*, p. 1-6, **DOI:10.1109/PVCon51547.2020.9757771**.

[78] Almorox, J., Voyant, C., Bailek, N., Kuriqi, A., Arnaldo, J.A. (2021). Total solar irradiance's effect on the performance of empirical models for estimating global solar radiation: An empirical-based review. *Energy*, vol. 236, art. ID 121486, **DOI:10.1016/j.energy.2021.121486**.

[79] Kumar, M., Kumar, P., Mukherjee, S., Priyadarshini, A., Biswas, S., Namrata, K. (2022). Comparison And validation of regression model for estimation of global solar radiation using Python. *IEEE International Students' Conference on Electrical, Electronics and Computer Science*, p. 1-6, **DOI:10.1109/SCEECS54111.2022.9740775**.

[80] Fan, C., Chen, M., Wang, X., Wang, J., Huang, B. (2021). A review on data preprocessing techniques toward efficient and reliable knowledge discovery from building operational data. *Frontiers in Energy Research*, vol. 9, **DOI:10.3389/fenrg.2021.652801**.

[81] Yang, J., Rahardja, S., Fränti, P. (2021). Mean-shift outlier detection and filtering. *Pattern Recognition*, vol. 115, art. ID 107874, **DOI:10.1016/j.patcog.2021.107874**.

[82] Mabasa, B., Lysko, M.D., Tazvinga, H., Mulaudzi, S.T., Zwane, N., Moloi, S.J. (2020). The Ångström-Prescott regression coefficients for six climatic zones in South Africa. *Energies*, vol. 13, no. 20, art. ID 5418, **DOI:10.3390/en13205418**.

[83] Uçkan, İ., Khudhur, K.M. (2022). Improving of global solar radiation forecast by comparing other meteorological parameter models with sunshine duration models. *Environmental Science and Pollution Research*, vol. 29, p. 37867-37881, **DOI:10.1007/s11356-022-18781-3**.

[84] Balli, Ö. (2021). Estimating global solar radiation from empirical models: An application. *European Mechanical Science*, vol. 5, no. 3, p. 135-147, **DOI:10.26701/ems.797177**.

[85] Joshi, U., Karki, I.B., Chapagain, N.P., Poudyal, K.N. (2021). Prediction of daily global solar radiation using different empirical models on the basis of meteorological parameters at Trans Himalaya Region, Nepal. *BIBECHANA*, vol. 18, no. 1, p. 159-169, **DOI:10.3126/bibechana.v18i1.29203**.

[86] Li, F., Wang, R., Mao, L., Zhu, D., She, X., Guo, J., Lin, S., Yang, Y. (2022). Evaluation of solar radiation models on vertical surface for building photovoltaic applications in Beijing. *IET Renewable Power Generation*, vol. 16, no. 8, p. 1792-1807, **DOI:10.1049/rpg2.12478**.

[87] Makade, R.G., Chakrabarti, S., Jamil, B. (2021). Development of global solar radiation models: A comprehensive review and statistical analysis for Indian regions. *Journal of Cleaner Production*, vol. 293, art. ID 126208, **DOI:10.1016/j.jclepro.2021.126208**.

[88] Zirebwa, F.S. (2014). *An Evaluation of the Performance and Subsequent Calibration of two Reference Evapotranspiration Estimation Models for Gweru, Zimbabwe*, p. 44-55.

[89] Hamza, B., Abdulmuminu, I. (2021). Statistical modelling of global solar radiation on horizontal surface using monthly means daily sunshine hours and some climatic variables for Zamfara state, Nigeria. *International Journal of Advances in Scientific Research and Engineering*, vol. 7, no. 5, p. 76-84, **DOI:10.31695/IJASRE.2021.34012**.

[90] WMO (2018). *Guide to Instruments and Methods of Observation (WMO-No. 8)*, WMO, Geneva.

[91] Liu, Y., Tan, Q., Pan, T. (2019). Determining the parameters of the Ångström-Prescott model for estimating solar radiation in different regions of China: Calibration and modeling. *Earth and Space Science*, vol. 6, no. 10, p. 1976-1986, **DOI:10.1029/2019EA000635**.

[92] Salima, G., Chavula, G.M.S. (2012). Determining angstrom constants for estimating solar radiation in Malawi. *International Journal of Geosciences*, vol. 3, no. 2, p. 391-397, **DOI:10.4236/ijg.2012.32043**.

[93] Fernando, D.M.Z., Calca, M.V.C., Raniero, M.R., Pai, A.D. (2019). Global solar irradiation for Maputo city - Mozambique: temporal evolution of measurements and statistical modeling. Energia na Agricultura, vol. 34, no. 1, p. 82-93, **DOI:10.17224/EnergAgric.2019v34n01p82-93**. (in Portuguese)

[94] Mulaudzi, T.S. (2019). *Evaluation of the Regression Coefficients for South Africa from Solar Radiation Data.* PhD Thesis, University of Venda, Venda, **hdl.handle.net/11602/1473**.

Strojniški vestnik - Journal of Mechanical Engineering 69(2023)1-2, 49-60
DOI:10.5545/sv-jme.2022.415
Original Scientific Paper
Received for review: 2022-10-15
Received revised form: 2022-12-21
Accepted for publication: 2023-01-11

Influence of the Side Branch Structure Pattern of the Imitation Cat's Claw Function on the Vibration and Noise of Tires

Guolin Wang[1] – Kexin Zhu[1] – Lei Wang[1] – Jian Yang[1,*] – Lin Bo[2]
[1] Jiangsu University, School of Automotive and Traffic Engineering, China
[2] KENDA Industrial Co., Ltd, China

To study the method of reducing the low-frequency vibration noise of tires, a passenger car tire (205/55R16) is taken as the research object. The dynamic grounding characteristics and vibration reduction mechanism of the cat's paw pad are analysed. The research showed that the swing deformation characteristics of paw pads during the walking process of cats are one of the main ways to reduce the impact from the ground and achieve vibration reduction and silencing. To analyse the influence of tire grounding on noise, tire grounding is divided into five areas, and the characteristics of ten tire grounding areas are analysed through tests. Pearson correlation analysis is used to obtain the characteristics of the eight most relevant grounding parameters with tire noise, and multiple linear regression is conducted between the characteristics of the eight grounding areas. The product of the correlation coefficient and the average value of the characteristics of the ground contact area shows that the central area of the tire tread contributes the most to the tire noise. The swing deformation characteristics of the bionic cat paw pad are realized by setting the staggered side branch pipe groove in the centre of the tire, and the vibration reduction characteristics of the bionic tire are analysed using the finite element method. The results showed that when the tire rolls, the amplitude and fluctuation range of the ground radial excitation force acting on the bionic tire are reduced compared with the original tire, and the vibration and noise characteristics of the tire are improved.

Keywords: bionics, vibration damping mechanism, vibration noise, tread pattern, structural design

Highlights

- *The swing deformation characteristics of paw pads during the walking process of domestic cats are one of the main ways of reducing the impact from the ground and achieving vibration reduction and silencing.*
- *The relationship between the tire grounding characteristic parameters and the measured noise is studied by region, and it is concluded that the tire tread centre area contributes the most to the tire noise.*
- *The dynamic and acoustic models of the tire are established and verified.*
- *The bionic design of the tread pattern in the centre of the tire tread was carried out, and the noise reduction mechanism of the bionic tire is analysed regarding the radial excitation force and noise of the tire.*

0 INTRODUCTION

Road traffic noise has become a significant source of noise pollution [1]. Studies have shown that when the driving speed of the car exceeds 70 km/h, the tire noise will become the main part of the vehicle's noise, accounting for more than 30 % of it [2]. In recent years, the tire labelling laws implemented in the European Union, the United States (US), and other countries and regions have put forward strict requirements on tire noise performance [3]. The vibration and noise of tires are one of the main reasons that affect the noise, vibration, and harshness (NVH) performance of vehicles [4] and [5]. How to reduce tire vibration and noise has always been the focus of major tire manufacturers. Ji and Bolton [6] analysed the relationship between tire vibration characteristics and radiated noise by using the structural modal analysis method. The results show that low-order modes have a greater impact on tire vibration radiated noise, and the frequency corresponding to the peak sound pressure is often near the natural frequency of the tire. Through simulation and experimental analysis, Zuo et al. [7] concluded that the periodic collision between tread blocks and the road surface is the main source of tire vibration noise, and the collision frequency is closely related to the number and size of blocks. Mohammadi and Ohadi [8] proposed a new method of reducing tire noise by using the multi-objective minimization method, optimized the structure and tread pattern parameters of patterned tires, reduced tire noise, and provided ideas for the research of low-noise tire patterns. Pei et al. [9] determined that the tread is the component with the greatest contribution to the tire by studying the contribution of each part of the tire's outer contour to vibration and noise and adding polyester damping materials to the tread and sidewall to suppress tire vibration. Zhang et al. [10] tested and compared the tire noise of different tire carcass structures. The results showed that the types and layers of carcass skeleton materials would change the vibration state of the carcass, thus affecting the tire noise. Although these noise reduction methods have achieved certain effects, in the finite element

*Corr. Author's Address: Jiangsu University, School of Automotive and Traffic Engineering, Zhenjiang, China, yangjian@ujs.edu.cn

analysis process, only smooth tires or tires with only longitudinal grooves are mostly used, and complex patterns are not considered. However, in the actual driving of passenger cars, most use complex tread patterns, and the vibration noise at low speeds is mainly caused by the tread patterns hitting the ground [11], so it is essential to study low-noise tread patterns.

In long-term biological evolution, animals have formed super-adaptive abilities to nature. The extremely strong vibration damping and muted effect of cats in the process of walking and running have long been a research focus of scholars. The paw pad of a domestic cat is the only body part that contacts the ground, which plays a very important role in the vibration reduction and silence of the domestic cat during walking, running, and jumping. Coulmance et al. [12] measured the forces exerted by the limbs of the cat during walking. The results showed that the front paw lift was preceded and accompanied by postural adjustment and that the front paws had a more important role in the cat's postural adjustment. Zhang et al. [13] established a mass-spring model to simulate the landing behaviour of domestic cats after jumping and used this model to analyse the cushioning characteristics of the domestic cat's paw rest. Kruger et al. [14] used a high-frequency camera to capture images of domestic cats and wild cats during normal walking, sprinting, and jumping from a height, and compared and analysed the cats' limb movements in different states.

With the deepening of research, the concept of bionics has been integrated into all walks of life and has been used as an important means of technological innovation. Wang et al. [15] applied the arc structure of the locust's foot in nature to the tread arc design of the tire, which reduces the tire wear and enhances the grip ability of the tire while reducing the vibration noise of the tire. The Gubo Tire Company and Polymer Research Center in Madison, Wisconsin, USA jointly developed a kind of non-pneumatic military honeycomb-like tire, which has good shock absorption and defence characteristics [16].

Chen et al. [17] can quickly disperse the boundary layer vortex with the help of the non-smooth structure of shark skin, so as to improve the principle of water flow speed. The non-smooth structure is set at the bottom and wall of the tire ditch to improve the tire's water-skiing performance. Zhang et al. [18] established a mathematical model of reindeer foot characteristics with the help of the reindeer's strong grip when walking on ice, and a bionic design was carried out for the tire tread. The bionic tire increased the contact area with ice and improved the anti-skid performance of the tire. Zhou et al. [19] were inspired by the strong adsorption capacity of octopus suction cups and established three bionic concave funnel suction cup tire patterns. Through simulation analysis, the bionic patterns have better tensile and compressive properties and better adsorption capacity on the ice surface, ensuring the anti-skid ability of the tire on the ice surface. With in-depth research on the mechanism of biological characteristics, such traits can be more reasonably applied to various industries. In order to apply the strong vibration reduction and mute effect of domestic cats when walking, running, and jumping to the design of a low-noise tread pattern structure, it is necessary to study the vibration reduction and mute mechanism of domestic cats to guide the structural design of low-noise tread pattern.

This paper takes the 205/55R16 tire as the research object and studies how to reduce the low-frequency vibration noise of the tire. The dynamic grounding characteristics and vibration reduction mechanisms of domestic cat paw pads are analysed, and the bionic noise reduction modification design of the tread pattern is carried out. The shock absorption characteristics of the imitation cat paw pad are realized by setting a staggering side branch pipe groove in the central area of the tire. On this basis, the noise reduction mechanism of imitation domestic cat paw pad pattern tires is studied.

1 A STUDY ON THE VIBRATION REDUCTION MECHANISM OF CAT PAW PADS

1.1 Mechanical Experiment of Contact Between Claw Pad and Ground

The purpose of the mechanical test on the contact between the paw pads of domestic cats and the ground is to obtain the vertical reaction force and strain characteristics of the paw pads of domestic cats in normal walking gait (v = 0.4 m/s to 0.8 m/s). The subjects are two healthy, defect-free domestic cats, aged 6 years, weighing 4.5 kg and 4.7 kg respectively. During the test, a pressure-sensitive channel (walkway A101; (Tekscan, USA)) is used to measure the vertical reaction force generated when the paw pads of domestic cats pass straight over the pressure plate at different speeds. To obtain the strain characteristics of the domestic cat on the ground, when the domestic cat walks in a straight line on the glass plate, grey speckles are added to its foot pads, as shown in Fig. 1. The motion of the paw pads was recorded by a high-speed camera (Olympus i-SPEED) installed under the glass plate, and then the images are digitized using the

VIC-2D of CSI Company (USA) to obtain the strain and related information of the paw pads in contact with the ground.

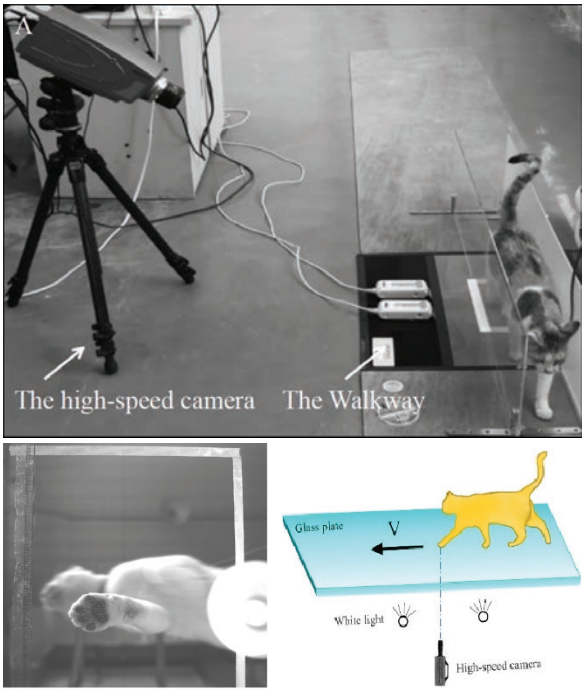

Fig. 1. *The contact tests of paw pads; a) contact pressure test; b) contact strain test*

1.2 Mechanical Analysis of Contact between the Claw Pad and the Ground

The contact strain magnitude and direction data information between the cat paw pad and the ground is obtained through VIC-2D digital processing. Relevant research **[12]** and **[20]** shows that when dogs and cats exercise, their front paw pads always play a more critical role than their rear paw pads in the process of realizing biological functions. Therefore, this paper mainly considers the front paws of cats. The three groups of effective tests are selected for analysis of the two domestic cats, and the strain characteristics with the same trend were obtained. This paper takes the centre group as an example to analyse the strain characteristics. The magnitude and direction of the contact strain between the palm pad and the toe pad are shown in Fig. 2. In the figure, the *X* direction is the forward direction of the cat, and the *Y* direction is the inner side of the cat's paw pad. From the principal strain direction, the deformation direction of the toe pad area has no change, and it is always tensile deformation in the *Y* direction. Before 0.180 s, the tensile deformation of the palm pad area is mainly in the *Y* direction, and after 0.180 s, the tensile deformation in the *X* direction is mainly in the *X* direction, which indicates that the swing deformation characteristics of the palm pad area exist in the *X* and *Y* directions. From the perspective of principal strain, the principal strain values of the four toe pads increase continuously during the whole contact process. The strain value of the pad increases first and then decreases alternately in the inner and outer regions. The maximum principal strain of the palm pad is significantly lower than that of the toe rest, which is caused by the change in the strain direction. This further illustrates that the palm pad area has the characteristics of swing deformation, vibration reduction, and noise reduction in the process of contacting the ground.

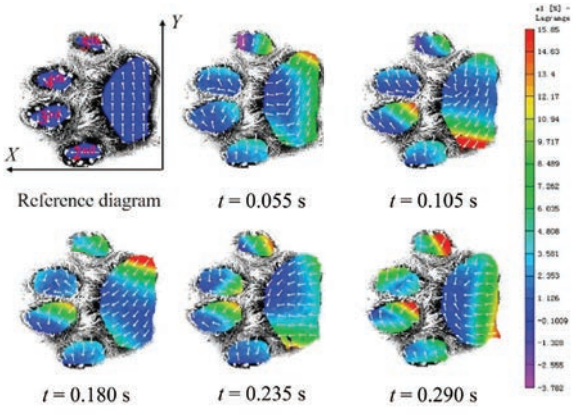

Fig. 2. *Strain magnitude and direction of contact between claw pad and ground*

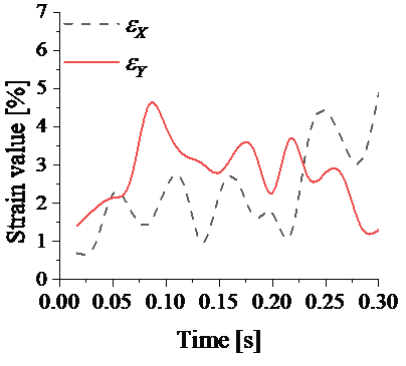

Fig. 3. *Time domain diagram of contact strain in X and Y directions of palm pad area*

To further clarify the attenuation of the strain value during the contact between the palm pad and the ground, the strain values in the *X* and *Y* directions of the palm pad area during the entire grounding process are extracted and plotted as a curve of the

strain value changing with time, as shown in Fig. 3. During the whole grounding process, the strain value of the palm pad area reflects a fluctuation change law with the opposite trend in *X* and *Y* directions, and the strain value of the palm rest is attenuated during the fluctuation process, which further proves that the impact load on the palm rest area during the grounding process can realize some dissipation with the swing deformation in *X* and *Y* directions.

2 TIRE GROUNDING DEFORMATION CHARACTERISTICS TESTING AND ANALYSIS

2.1 Tire and Ground Pressure Distribution Testing

Fig. 4 is a physical map of 205/55R16 PCR tires produced by 10 different manufacturers and used in this experiment. Table 1 lists the noise-related information of 10 test tires. The noise values are derived from the tire performance test data published in the literature [21]. In this paper, the noise performance of the tire is evaluated with the pass-by noise, which is the noise value measured by the test tire when the vehicle's engine is turned off and the vehicle passes through the measurement area at a speed of 80 km/h.

Fig. 4. *Physical drawing of 205/55R16 test tire*

Table 1. *Test tire information and noise value*

Number	Type	Through noise value [dB]
1	Turanza ER 300	71.5
2	PROXES C100 PLUS	71.5
3	LS388	71.0`
4	MARMONIC M220	70.4
5	ADVAN dB DECIBEL V551	71.1
6	SPORT SA-37	72.1
7	Primacy 3 ST	70.6
8	N'FEAR SU4	70.8
9	Efficient Grip Performance	70.7
10	Conti Max Contact MC5	72.4

As shown in Fig. 5, the American Tekscan pressure test system is used to obtain the grounding marks and pressure distribution of 10 test tires. The inflation pressure of the tires during the test is 0.24 MPa of the rated pressure, and the load is 4821 N of the rated load.

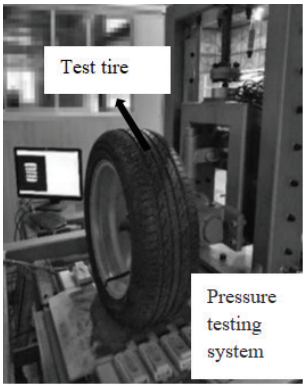

Fig. 5. *Ground pressure deformation*

2.2 Grounding Area Division and Grounding Parameters

Most of the 10 tires used in the test have asymmetric tread patterns and are divided into five areas by four longitudinal grooves. Therefore, the tread is divided into five areas by taking the groove wall of four longitudinal grooves as the boundary: the outer shoulder area (I), the outer transition area (II), the central area (III), the inner transition area (IV), and the inner shoulder area (V).

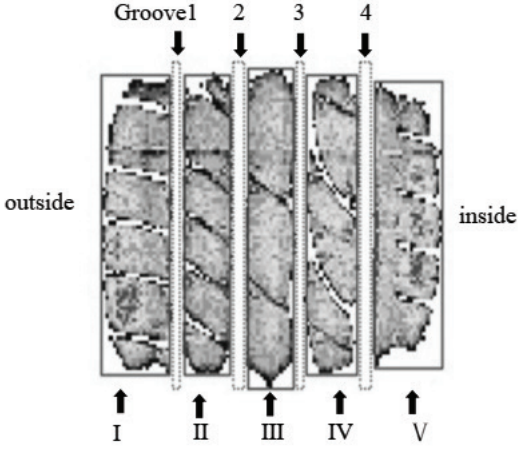

Fig. 6. *Tread grounding area division*

The ground deformation parameters are mainly divided into grounding geometric parameters and grounding pressure parameters. The geometric parameters are the grounding area, imprint area, grounding area ratio, grounding length, grounding

width, grounding aspect ratio, and rectangle ratio. The pressure parameters are average grounding pressure and grounding pressure skewness. Liang [22] defines the grounding geometric parameters and grounding pressure parameters of tires in detail. Through the test, the grounding geometric parameters and grounding pressure parameters of the whole area of the grounding footprint, the outer tire shoulder area (I), the outer transition area (II), the central area (III), the inner transition area (IV), and the inner tire shoulder area (V) are divided into 54 grounding deformation characteristic parameters.

2.3 Analysis of Grounding Deformation Parameters

Due to the limited number of test tires and the need to find evaluation indexes related to high noise value, the Pearson correlation analysis method is used to eliminate the ground deformation parameters with poor correlation with noise value; it is calculated as follows:

$$r = \frac{\sum_{i=1}^{n}(x_i - \bar{x})(y_i - \bar{y})}{\sqrt{\sum_{i=1}^{n}(x_i - \bar{x})^2 \sum_{i=1}^{n}(y_i - \bar{y})^2}}. \quad (1)$$

In the formula, n is the number of samples. y_i, $\bar{y}$, x_i, and $\bar{x}$ are the tire noise value, the average tire noise value, the tire grounding parameters, and the average grounding parameters, respectively.

The correlation level is evaluated by the significant coefficient. The formula of the significant coefficient is:

$$t = \frac{r\sqrt{n-2}}{\sqrt{1-r^2}}, \quad (2)$$

where t obeys the t distribution with $n - 2$ degrees of freedom.

When $|r| > 0.5$ and $t < 0.05$, the ground deformation parameter is highly correlated with the noise values. Through the analysis of 54 grounding deformation characteristic parameters mentioned in Section 2.2, the grounding deformation characteristic parameters ($|r| > 0.5$ and $t < 0.05$) related to high noise value are obtained, as shown in Table 2.

Table 2. *Grounding parameters related to high pass-through noise*

Area	Grounding parameters	Noise value	
		r	t
the overall area	Rectangle ratio (x_1) [%]	–0.674	0.033
	Average ground pressure (x_2) [kPa]	0.855	0.002
	Deviation value of grounding pressure (x_3) [kPa]	0.677	0.031
the outer shoulder area (I)	Grounding length (x_4) [mm]	–0.853	0.002
the central area (III)	Average ground pressure (x_5) [kPa]	0.750	0.012
the inner transition area (IV)	Average ground pressure (x_6) [kPa]	0.788	0.007
	Deviation value of grounding pressure (x_7) [kPa]	0.705	0.023
the inner shoulder area (V)	Grounding length (x_8) [mm]	–0.744	0.014

The quantitative relationship between the grounding deformation characteristic parameters and the noise value can be obtained through multiple linear regression, and the contribution of each parameter and region to the noise value can be clearly obtained through the formula. Table 3 shows the ground deformation characteristic parameter values related to high noise corresponding to 10 tires. Taking Table 3 as the multiple linear regression sample, the relationship between the noise value and the grounding deformation characteristic parameters obtained through multiple linear regression is:

Table 3. *Sample scheme by noise value*

i	x_1	x_2	x_3	x_4	x_5	x_6	x_7	x_8	Noise value, y [dB]
1	0.868	376.368	183.461	118.667	364.899	396.095	188.851	112.667	71.5
2	0.891	365.712	181.264	115.667	349.691	411.347	174.922	112.000	71.5
3	0.919	379.622	192.799	124.000	354.681	381.658	188.859	116.000	71.0
4	0.871	350.895	166.829	132.000	348.677	383.964	177.211	124.667	70.4
5	0.925	375.085	186.990	131.667	365.922	411.568	163.246	115.000	71.1
6	0.867	394.792	179.938	113.000	416.636	428.593	182.123	109.333	72.1
7	0.909	342.809	160.781	125.333	319.412	382.447	172.136	113.333	70.6
8	0.909	373.652	176.752	124.000	382.872	413.290	173.031	113.667	70.8
9	0.916	363.632	163.403	123.667	359.806	412.076	164.007	115.000	70.7
10	0.837	398.657	194.303	113.000	402.456	452.066	221.015	110.333	72.4

$$y = 82.238 - 15.078x_1 + 0.034x_2 + 0.007x_3 - 0.004x_4 - 0.015x_5 + 0.006x_6 - 0.014x_7 - 0.047x_8. \quad (3)$$

The R^2 of constructed multiple linear regression equation is the error caused by linear fitting. The closer this value is to 1, the more accurate the prediction is. The R^2 of this multiple linear regression equation is 0.984, which indicates that this equation has high prediction accuracy.

It can be seen from Eq. (3) that the noise of the tire is determined by the absolute value a_i of the polynomial coefficient and the average value of the grounding characteristic parameters $\overline{x}_i$. When analysing the contribution of grounding characteristic parameters to noise, both of them should be considered together. Therefore, this paper evaluates the contribution of noise value by the product of the coefficients of different grounding regions (polynomial coefficients) of the regression equation and the average value of the corresponding grounding characteristic parameters. The results are shown in Table 4.

Table 4. *Contribution of ground deformation parameters*

I	II	III	IV
$a_4 \cdot \overline{x}_4$	$a_5 \cdot \overline{x}_5$	$a_6 \cdot \overline{x}_6 + a_7 \cdot \overline{x}_7$	$a_8 \cdot \overline{x}_8$
0.49	5.50	4.96	5.36

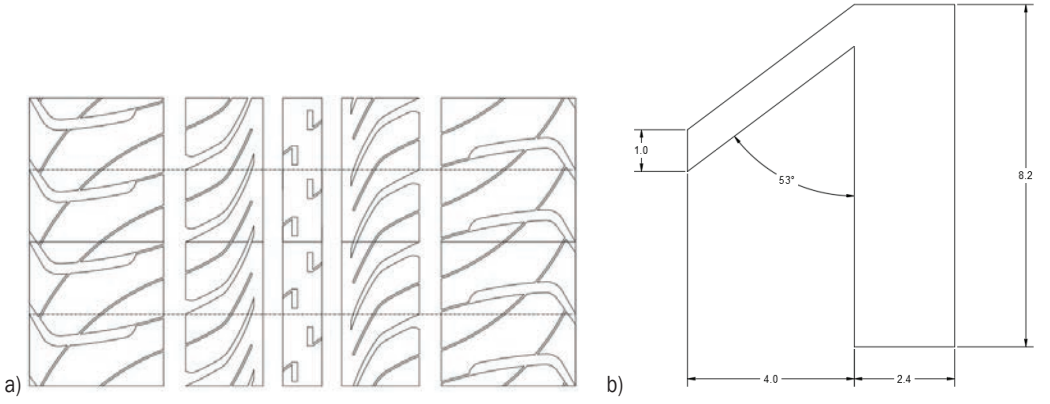

Fig. 7. *Tire pattern bionic variant; a) tread pattern; and b) side branch structure and parameters*

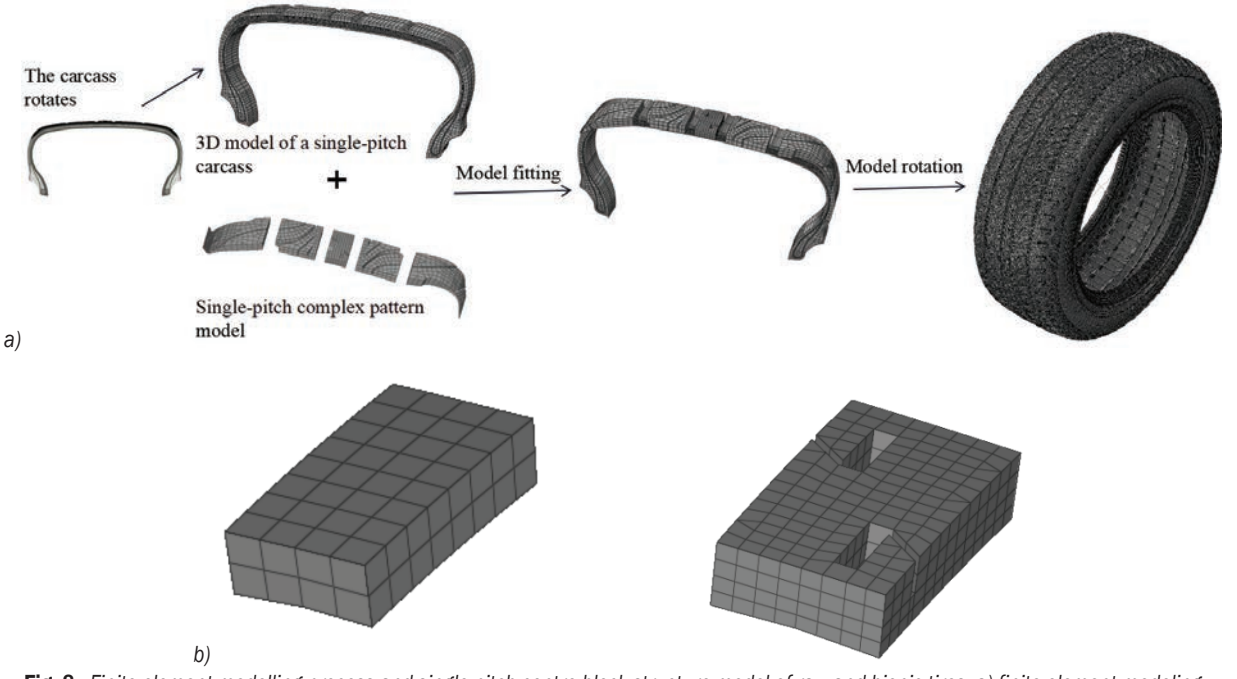

Fig. 8. *Finite element modelling process and single-pitch centre block structure model of raw and bionic tires; a) finite element modeling process; and b) model of the structure of the centre block of the single pitch of the original and bionic tires*

As shown in Table 4, it can be seen that the contribution degree to tire noise is from high to low, and the centre area (III), inner tire shoulder area (V), inner transition area (IV), and outer tire shoulder area (I). Therefore, in order to reduce noise, we can start with the pattern design in the central area.

3 DESIGN AND ANALYSIS OF TIRE PATTERN BIONIC VIBRATION AND NOISE REDUCTION

3.1 Tire Pattern Bionic Vibration and Noise Reduction Design

The vibration characteristics of tires are an important part of the NVH performance of vehicles. Inspired by the domestic cat's paw pad to weaken the impact from the ground through swinging deformation, reducing the radial vibration characteristics of tires is an important means of vibration and noise reduction of vehicles. Moreover, through the previous research of the research group, the side branch pipe structure has a certain weakening effect on the pipe resonance noise of the pattern, can simultaneously improve the anti-skid performance of the tire, and can synergistically improve the comprehensive performance of the tire [23].

As shown in Fig. 7, the 205/55R16 passenger car tire is taken as the research object, and the dislocation side branch pipe groove pattern is arranged in the central area of the tread, so as to achieve the characteristics of vibration reduction by imitating the swing deformation of the cat palm pad. Therefore, the finite element analysis model of the tire is established as shown in Fig. 8. During modelling, the Yeoh model is used for rubber material, Rebar is used for cord description, and there are 2141 nodes and 1998 units in a two-dimensional matrix. See Zhou et al. [24] and Chen et al. [25] for specific material properties and finite element type settings.

3.2 Verification of the Finite Element Model

3.2.1 Tire Static Ground Pressure Distribution Test

The modelling method of the finite element analysis model in this paper has been verified by a large number of experiments [24] and [25]. To verify the validity of the finite element model in this paper, the pressure distribution test system is used to test the grounding pressure when the tire is inflated to 0.21 MPa and loaded to 3800 N. Fig. 10 shows the pressure comparison between the test and simulation analysis results; it can be seen that the distribution of the test and simulation grounding pressure has a good consistency.

3.2.2 Tire Stiffness Test

An MTM-2 comprehensive strength tester is used to test the stiffness of the 205/55R16 radial passenger car tire in accordance with GB/T23663-2009 [26]. The test and simulation results of tire squat, static loading radius, and radial stiffness under different test conditions are shown in Tables 5 and 6, from which it can be seen that the subsidence, static loading radius, and radial stiffness of the test and simulation have good consistency.

3.2.3 Tire Modal Test

To further verify the validity of the finite element model, the mode tests are carried out on tires using dynamic testing equipment from LMS 24-Channel Data Source Collector. The sampling frequency of the instrument is 25600 Hz. The modal analysis software is LMS Test. Lab. Acceleration sensor for the US PCB company triaxial acceleration sensor 356A34. The impact hammer is the US PCB 086C02 impact hammer. The test tire is put in the free suspension state, and 24 measuring points are evenly arranged on the tire surface. The physical diagram of the tire test is shown in Fig. 9.

Fig. 9. *Actual pattern of the modal test*

In this test, the hammer method is used for excitation, point-by-point excitation is used, and the

acceleration sensor is used to measure the response signal. The excitation and response signals are amplified and input into the dynamic analyser, and the transfer function in the range of 0 Hz to 320 Hz is obtained through analysis and processing. Each measuring point is hammered three times, and the transfer function of this point is obtained after a linear average, and then the first six radial natural frequencies and vibration modes of the tire under a free mounting state are obtained.

The Lanczos method in Abaqus is used in the tire free mode finite element analysis to calculate the first six radial natural frequencies and vibration modes in the free state of the tire and compare them with the test mode. The results are shown in Table 7.

It can be seen from Table 7 that the relative error between the first six natural frequencies of the tire obtained from simulation and the first six natural frequencies of the tire obtained from testing is less than 10 %. Its error meets the analysis requirements. s can be seen from Fig. 11, the simulation and test of the first sixth-order modal mode of the tire have strict symmetry and good consistency, which further verifies the accuracy of the finite element model.

The main reasons for the error are as follows:

1. A variety of rubber materials and steel wire materials are used in the tire, and the distribution of the materials in the simulation analysis is slightly different from that of the actual tire.

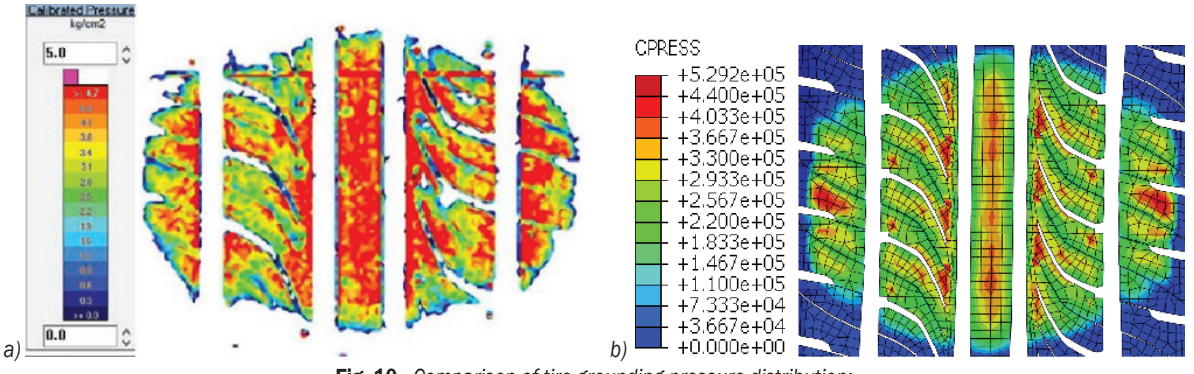

Fig. 10. *Comparison of tire grounding pressure distribution; a) test the ground pressure distribution; and b) simulate the ground pressure distribution*

Table 5. *Comparison of test and simulation results of tire squat and static loading radius under different test conditions*

Test conditions	Test value				Simulation value			
	210 kPa		250 kPa		210 kPa		250 kPa	
	Squat [mm]	Static loading radius [mm]	Squat [mm]	Static loading radius [mm]	Squat [mm]	Static loading radius [mm]	Squat [mm]	Static loading radius [mm]
123 kg	6.01	308.14	5.49	309.01	6.48	309.47	5.98	309.97
246 kg	12.28	301.87	11.13	303.37	12.17	303.78	11.62	304.33
369 kg	18.06	296.09	16.29	298.21	18.28	297.67	16.99	298.96

Table 6. *Comparison between test value and simulation value of tire stiffness*

	Load [kg]	210 kPa			250 kPa		
		Test value [N/mm]	Simulation value [N/mm]	Error [%]	Test value [N/mm]	Simulation value [N/mm]	Error [%]
Radial stiffness	123	200.57	186.02	7.25	219.56	201.57	8.19
	246	196.32	198.09	-0.90	216.60	207.47	4.22
	369	200.23	197.82	1.20	221.99	212.84	4.12

Table 7. *Comparison of tire natural frequency test and simulation results*

Order	1	2	3	4	5	6
Test value [Hz]	59.625	100.102	110.391	138.711	165.304	191.455
Simulation value [Hz]	64.442	90.894	113.06	135.64	158.46	181.09
Error [%]	7.47	9.2	2.42	2.21	4.14	5.41

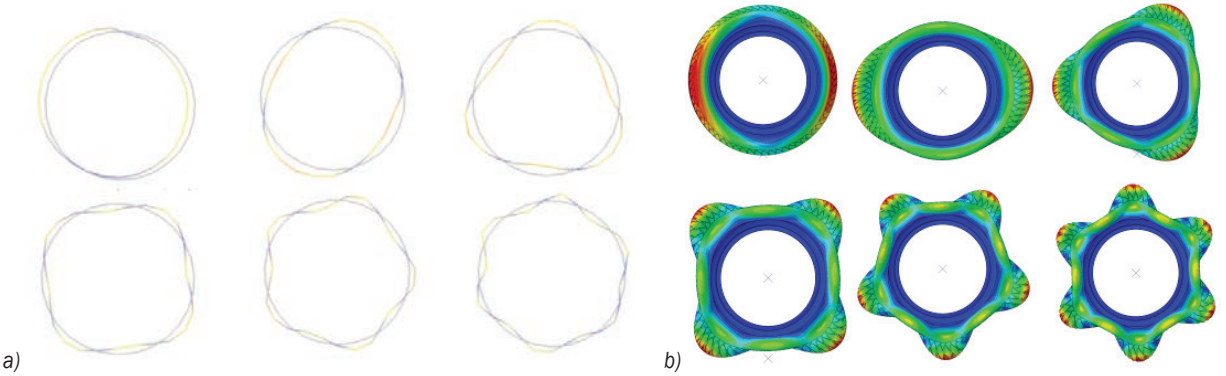

Fig. 11. *Test test and numerical calculation of the first 6th order modal mode of the tire; a) test results; and b) simulation results*

2. The simulation analysis simplified some of the small tread grooves and simplified the rim of the tire, resulting in a different stiffness and mass of the simulated tire than the actual tire.
3. While the modal analysis is based on linear assumptions, the tire material is highly nonlinear.

3.3 Development of a Model for Analysing Tire Vibration and Noise

The tire vibration and noise simulation model are shown in Fig. 12. The observation points for the arranged sound pressure measurement refer to GB/T3767-2016. A semi-circular bell jar with a radius of one metre is built around the tire. Nineteen acoustic observation points are defined on the semi-circular bell jar, and a plane is built at the bottom of the tire to simulate the road surface sound reflection. Through analysis and calculation, it can be concluded that the curve trends in the frequency band obtained from the 19 acoustic observation points are roughly the same, but the sound pressure values are different. The total sound pressure level of tire vibration noise is obtained by the A-weighted superposition of the 19 acoustic observation points, and this value is used as the evaluation index of tire vibration noise.

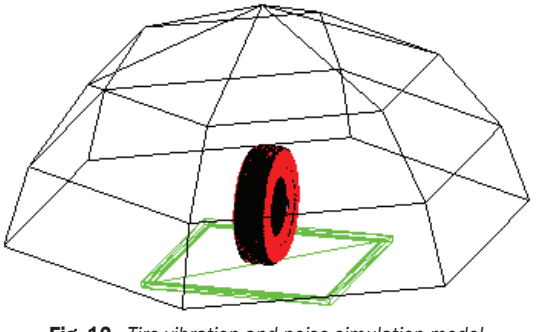

Fig. 12. *Tire vibration and noise simulation model*

4 RESULT ANALYSIS AND DISCUSSION

4.1 Comparison and Analysis of Tire Ground Strain

The strain distribution of the original tire and the bionic tire in *X* and *Y* directions under 70 km/h steady state rolling is obtained through finite element analysis, and the results are shown in Fig. 13, from which it can be seen that the bionic tire with staggered branch pipe pattern in the central area of the tread changes the symmetry of the strain distribution in the *X* and *Y* directions compared with the original tire, and the asymmetric deformation will form the swinging deformation in the *X* and *Y* directions during the rolling process of the tire. Therefore, the swing characteristics of the grounding deformation of the cat's paw pad can be achieved by arranging the misplaced side branch pipes in the central area of the tire pattern.

4.2 Results and Analysis of the Radial Excitation Force

The 70 km/h display rolling calculation is carried out for the tire, and the radial excitation force of the tire after steady rolling is extracted. The comparison of the radial excitation force between the original tire and the bionic tire in the time domain is shown in Fig. 14. Through the comparison, it can be seen that the peak radial excitation force of the bionic tire is reduced, and the range of radial excitation force fluctuations is reduced, thereby reducing the vibration phenomenon during the driving of the tire. It shows that the misplaced side branch pipe structure on the tire tread realizes the function of the bionic cat claw and reduces the radial excitation force to the tire from the ground.

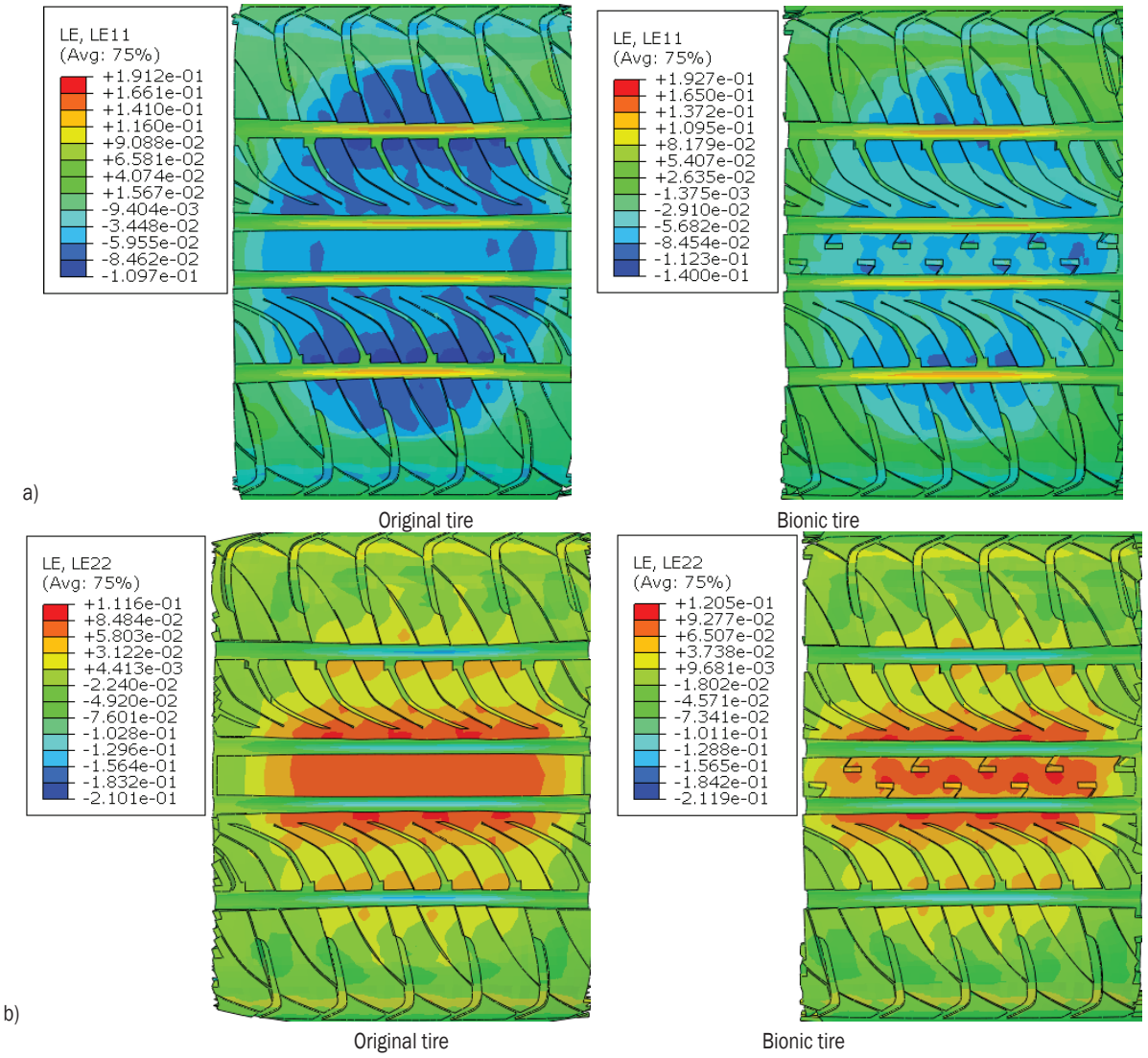

Fig. 13. *Strain distribution in the X and Y directions of the ground area when the two tires are rolling steadily; a) strain distribution in the X direction of both tire; and b) strain distribution in the Y direction of the two tires*

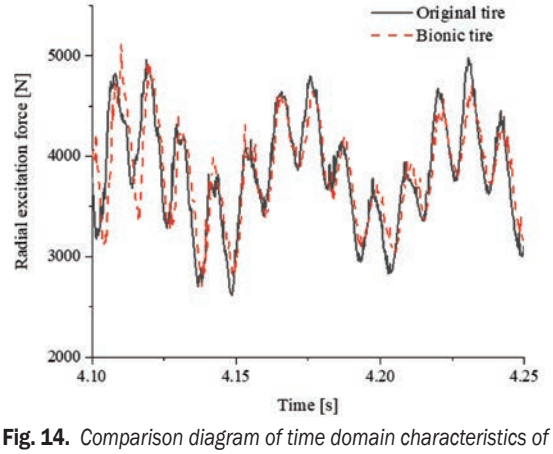

Fig. 14. *Comparison diagram of time domain characteristics of two types of tires subjected to ground radial excitation forces*

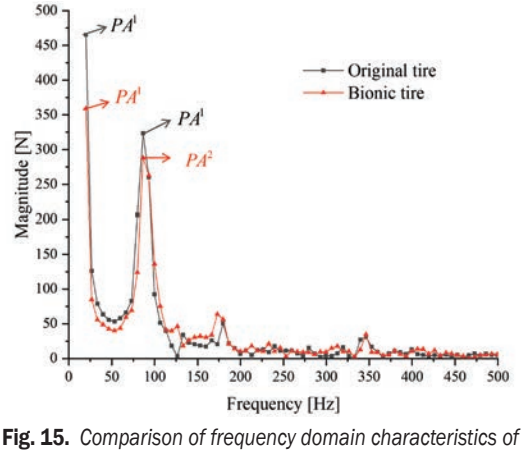

Fig. 15. *Comparison of frequency domain characteristics of amplitude of ground radial excitation force on two types of tires*

To further clarify the difference between the radial excitation force of the original tire and the bionic tire, fast Fourier transform (FFT) is performed on the radial excitation force in the time domain to obtain the amplitude-frequency characteristics of the radial excitation force in the frequency domain. The results are shown in Fig. 15. As the sound below 20 Hz cannot be heard by human ears, and the tire vibration noise is mainly concentrated below 500 Hz **[27]** and **[28]**, this paper takes 20 Hz to 500 Hz as the frequency range for analysis. In Fig. 15, PA^1 is the peak amplitude 1, and PA^2 is the peak amplitude 2. At PA^1 (20 Hz), the amplitude value of the radial excitation force on the bionic tire is 22.16 % lower than that on the original tire, and at PA^2 (87 Hz) it is 8.53 % lower. It shows that the tread pattern tire with cat claw function has an obvious vibration reduction effect.

4.3 Numerical Analysis of Vibration and Noise and Discussion of Results

In order to analyse the vibration and noise characteristics of bionic tires with misaligned side branch structures in the tread centre, the vibration and noise analysis model established in this paper and the analysis process in literature **[9]** and **[24]** are used to analyse the tire vibration and noise. The vibration noise of the original tire and the bionic tire at 20 Hz to 500 Hz is shown in Fig. 16.

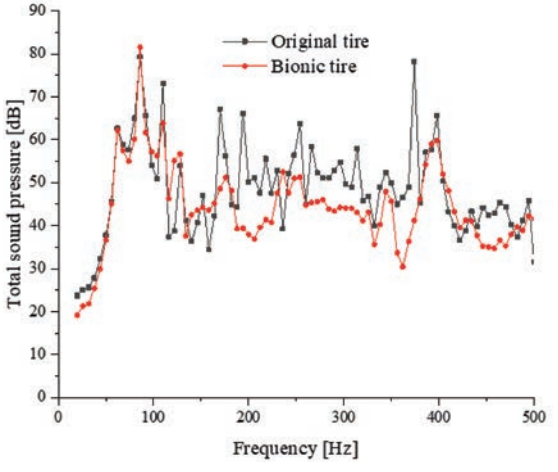

Fig. 16. *Comparison of the total sound pressure level of the two types of tires*

The sound pressure level of the bionic tire is lower than the total sound pressure level of the original tires in the whole frequency band, especially at 374 Hz, which is reduced from 78.25 dB to 41.20 dB, which is 47.35 %. The total noise value of the original tire is 64.02 dB and the noise value of the bionic tire is 62.86 dB by A-weighted superposition of the noise value in the 20 Hz to 500 Hz frequency band, which further shows that the bionic tire with misaligned sidewall structure has a good noise reduction effect.

It can be seen from Table 8 that in the comparison of the vibration and noise characteristics between the original tire and the bionic tire, the bionic tire has a better inhibition effect on the impact load from the ground during driving. This pattern design has a good effect on the vibration and noise reduction of the tire, which verifies the feasibility of bionic vibration and noise reduction.

Table 8. *Comparison of amplitude and noise values of the two types of tires*

Tire type	PA^1	PA^2	Total sound pressure level [dB]
Original tire	465.37	323.65	64.02
Bionic tire	362.24	296.05	62.86

5 CONCLUSION

1. Through the grounding mechanical test on the paw pad of the domestic cat, it is found that the left and right swing grounding characteristics of the paw pad of the domestic cat during walking is one of the main ways to achieve the effect of vibration reduction and silence during walking.
2. By analysing the grounding characteristic parameters of ten tires, it is concluded that the tire centre area has the greatest impact on tire noise. On this basis, combined with the vibration reduction principle of the left and right swing of the cat paw pad during walking, the staggered side branch pipe groove is set in the centre of the tire to achieve the vibration reduction characteristics of the swing of the cat paw pad.
3. The bionic tire can significantly reduce the amplitude and fluctuation range of the ground radial excitation force, thereby effectively reducing the vibration noise in the low frequency band, and improving the vibration noise characteristics of the tire.

5 ACKNOWLEDGEMENTS

This study was financially supported by the National Natural Science Foundation of China (52072156,52272366) and the Postdoctoral Foundation of China (2020M682269).

8 REFERENCES

[1] Sandberg, U., Ejsmont, J.A. (2002). *Tyre/Road Noise Reference Book*. INFORMEX, Kisa.

[2] Diaz, C.G., Kindt, P., Middelberg, J., Vercammen, S., Thiry, C., Close, R., Leyssens, J. (2016). Dynamic behaviour of a rolling tyre: Experimental and numerical analyses. *Journal of Sound and Vibration*, vol. 364, p. 147-164, **DOI:10.1016/j.jsv.2015.11.025**.

[3] EUR-Lex (2014). European Parliament and Council, Regulation (EU) no 540/2014 on the sound level of motor vehicles and of replacement silencing systems and amending directive 2007/46/EC and repealing directive 70/157/EEC, *Official Journal of the European Union*, L 158/131, p. 131-195.

[4] Sen, H. (2013). Present status and prospect on vehicle NVH technology. *Automobile Parts*, vol. 7, p. 78-81, **DOI:10.19466/j.cnki.1674-1986.2013.05.019**. (in Chinese)

[5] Abouel-Seoud, S. (2019). Tire and engine sources contribution to vehicle interior noise and vibration exposure levels. *Archives of Acoustics*, vol. 44, no. 2, p. 201-214, **DOI:10.24425/aoa.2019.126366**.

[6] Ji, L., Bolton, S.J. (2015). Coupling mechanism analysis of structural modes and sound radiations of a tire tread band based on the S-mode technique. *Applied Acoustics*, vol. 99, p. 161-170, **DOI:10.1016/j.apacoust.2015.06.013**.

[7] Zuo, S.G., Xin, T.I., Zeng, X., Xu-Dong, W. U. (2014). Analysis of structural vibration noise characteristics of rolling tire. *Journal of Jiamusi University (Natural Science Edition)*, vol. 32, no. 2, p. 161-165. (in Chinese)

[8] Mohammadi, S., Ohadi, A. (2021). A novel approach to design quiet tires, based on multi-objective minimization of generated noise. *Applied Acoustics*, vol. 175, art. ID 107825 **DOI:10.1016/j.apacoust.2020.107825**.

[9] Pei, X., Wang, G., Zhou, H., Zhao, F., Yang, J. (2016). Influence of tread structure design parameters on tire vibration noise. *Proceedings of SAE-China Congress 2015: Selected Papers. Lecture Notes in Electrical Engineering*, vol. 364, p. 325-338, **DOI:10.1007/978-981-287-978-3_30**.

[10] Zhang, D., Zhu, Z. H., Jian, L., Chen, H., Chen, X. (2012). Effect of carcass structure on noise of semi-steel radial tire. *The 16th China Tire Technology Seminar*, p. 138-140.

[11] Ling, S., Yu, F., Sun, D., Sun, G., Xu, L. (2021). A comprehensive review of tire-pavement noise: Generation mechanism, measurement methods, and quiet asphalt pavement. *Journal of Cleaner Production*, vol. 287, art. ID 125056, **DOI:10.1016/j.jclepro.2020.125056**.

[12] Coulmance, M., Gahéry, Y., Massion, J., Swett, J.E. (1979). The placing reaction in the standing cat: a model for the study of posture and movement. *Experimental Brain Research*, vol. 37, p. 265-281, **DOI:10.1007/BF00237713**.

[13] Zhang, X., Yang, J., Yu, H. (2012). Mechanical buffering characteristics of feline paw pads. *Journal of Biomedical Engineering*, vol. 29, no. 6, p. 1098-1104. (in Chinese)

[14] Kruger, K.M., Graf, A., Flanagan, A., McHenry, B. D., Altiok, H., Smith, P.A., Krzak, J.J. (2019). Segmental foot and ankle kinematic differences between rectus, planus, and cavus foot types. *Journal of Biomechanics*, vol. 94, p. 180-186, **DOI:10.1016/j.jbiomech.2019.07.032**.

[15] Wang, G., Tong, X., Dong, Z., Haiqing, X.U. (2016). Study on relationship between grounding characteristics and crown temperature field of radial tire. *China Rubber Industry*, vol. 63. (in Chinese)

[16] Su, B. (2009). Cooper bionic honeycomb tire. *Rubber Technology Market*, vol. 7, no. 10, p. 14. (in Chinese)

[17] Chen, L., Zhao, F., Wang, G.L., Yang, J., Zhou, H.C. ,Wan, Z.J. (2019). Tire vibration noise study of radial truck tire based on a new non-natural equilibrium design. *Journal of Vibration Engineering*, vol. 37, no. 1, p. 23-31, **DOI:10.16731/j.cnki.1671-3133.2019.01.005**.

[18] Zhang, R., Li, G., Qiao, Y., Jiang, L., Li, J. (2019). Analysis for effect of tire tread element of imitation reindeer plantar morphology on tire anti-skid performance. *Transactions of the Chinese Society of Agricultural Engineering*, vol. 35, no. 7, p. 47-53, **DOI:10.11975/j.issn.1002-6819.2019.07.006**.

[19] Zhou, L., Wang, H. (2013). Imitation octopus sucker-type tire tread pattern design and finite element analysis. *Journal of Xi'an University of Technology*, vol. 29, no. 2, p. 228-232, **DOI:10.19322/j.cnki.issn.1006-4710.2013.02.021**.

[20] Morris, A., Erles, K., Maddox, T.W. (2018). Displacement of an ununited medial humeral condylar ossification centre in the cat. *Veterinary and Comparative Orthopaedics and Traumatology*, vol. 31, no. 2, p. 153-157, **DOI:10.3415/VCOT-17-06-0084**.

[21] Zhang, Z.Y. (2016). 2016 China Tire German Test [J/OL], from *https://www.autohome.com.cn/drive/201608/891160-2.html*, accessed on 2020-09-10.

[22] Liang, C. (2013). Research on evaluation system and method of comprehensive grounding performance of radial tire. *Jiangsu University*. (in Chinese)

[23] Wang,G. L., Zhou, H.C.,Yang, J. (2014). Simulation analysis of the influence of branch pipe on tire noise and anti-water skiing performance. *Journal of System Simulation*, vol. 26, no. 3, p. 675-681, **DOI:10.16182/j.cnki.joss.2014.03.005**. (in Chinese)

[24] Zhou, H., Li, H., Liang, C., Zhang, L., Wang, G. (2021). Relationship between tire ground characteristics and vibration noise. *Strojniški vestnik - Journal of Mechanical Engineering*, vol. 67, no. 1-2, p. 11-27, **DOI:10.5545/sv-jme.2020.6946**.

[25] Chen, L., Zhao, F., Wang, G.L. , Yang, J., Zhou, H.C., Wan, Z.J. (2015). Tire vibration noise study of radial truck tire based on a new non-natural equilibrium design. *Journal of Vibration Engineering*, vol. 28, no. 05, p. 800-808, **DOI:10.16385/j.cnki.issn.1004-4523.2015.05.016**.

[26] GB/T 23663-2009. Test method of automobile tyre longitudinal and lateral stiffness from *https://www.auto-testing.net/news/show-105200.html*, accessed on 2021-03-10. (in Chinese)

[27] Heckl, M. (1986). Tyre noise generation. *Wear*, vol. 113, no. 1, p. 157-170, **DOI:10.1016/0043-1648(86)90065-7**.

[28] Bai, S., Xu, X., Liu, X. (2013). Vehicle panel acoustic contribution analysis and tests for noise reduction. *Journal of Vibration and Shock*, vol. 32, no. 24, p. 204-208, **DOI:10.13465/j.cnki.jvs.2013.2**.

Strojniški vestnik - Journal of Mechanical Engineering 69(2023)1-2, 61-72
DOI:10.5545/sv-jme.2022.238
Original Scientific Paper
Received for review: 2022-06-16
Received revised form: 2022-10-10
Accepted for publication: 2022-11-03

The Application of Neural Networks to Modular Arrangements of Predetermined Time Standards

Emmanuel Basitere[1] – Ilesanmi Daniyan[1,*] – Khumbulani Mpofu[1] – Adefemi Adeodu[2]

[1] Tshwane University of Technology, Department of Industrial Engineering, South Africa
[2] University of South Africa, Department of Mechanical Engineering, South Africa

Modular arrangements of predetermined time standards (MODAPTS) is an effective and efficient method to measure work and the activities associated with it. The time standard is used all over the world in different industries, but the method is old, slow, and difficult for first-time users to work with. This study applied neural networks (NN) to MODAPTS. Primary training data in the form of MODAPTS keywords were employed. The training data were acquired as raw data in the form of MODAPTS time studies. These data however was then broken and processed to extract the keywords for the training of the NN. The NN was also trained with the data collected using the TensorFlow algorithm assisted by the Keras library. This was achieved by first learning the fundamentals of creating a NN. Thereafter, consolidating several tools, such as the Python programming language and the Keras library, were used to implement the artificial neural network (ANN). The results obtained indicated that 94.7 % of successful predictions were made by the NN while only 5.3 % were manually entered codes to correct the ANN chatbot. The mean difference between the two methods is 0.25 minutes; the t-test was calculated at 95 % confidence level (0.05) and produced a P-value of 0.9663. The computed P-value was greater than 0.05, showing that there is no significant difference between the two generated studies. The MODAPTS-ANN technique demonstrated in this study possesses great potential to improve and refine work measurement.

Keywords: artificial neural network, modular arrangement of predetermined time standard, TensorFlow algorithm

Highlights

- *Implementation of the ANN using the combination of Python programming language and the Keras library.*
- *Coupling of the MODAPTS with NN to further extend the use of MODAPTS for work measurement and motion analysis.*
- *Work measurement and motion prediction using the integrated tool of MODAPTS and ANN.*

0 INTRODUCTION

Modular arrangements of predetermined time standards (MODAPTS) is a highly reliable method of conducting timekeeping, process planning, and formulating workplace efficiencies with ease and pace in application [1]. According to Cho and Park [2], MODAPTS was authored by Heyde in 1966, and its core components are still used today to define work and its activities. MODAPTS has been defined as the most popular time standard amongst its closest counterparts [2].

Conducting a MODAPTS analysis usually involves several components that would allow for a successful feasibility study; this includes but is not limited to understanding an activity by video analysis or continuous observation, analysing possible efficiencies from that observation and, most importantly, in-depth knowledge of the MODAPTS time standard and its principles to prove those efficiencies. Mastering the MODAPTS time standard can be somewhat challenging and rather complicated for the engineer, as mentioned by Mallembakam [3]. The total time it takes to conduct a MODAPTS study may be too long due to the nature of the observed activity and converting those activity tasks to MODAPTS code. This may reduce producing reputable studies and may hinder achieving set targets.

MODAPTS is regarded as one of the most popular time standards, widely used in the manufacturing, healthcare, service, and garment industries [4]. However, constructing a reputable MODAPTS time study consumes too much time. According to Mallembakam [3], it takes approximately two hours to accurately conduct, analyse, and present the findings of a designated feasibility study. Furthermore, MODAPTS requires great care and focus with regard to implementation. Therefore, a thorough understanding of the time standard is required to avoid any errors or mistakes and may prove challenging to a novice engineer [5]. The significance of this study is that the time to conduct a MODAPTS study can be significantly reduced. Furthermore, applying MODAPTS principles will be significantly easier, as the MODAPTS code will be automatically generated.

0.1 Artificial Neural Networks (ANN)

According to Graupe [6], artificial neural networks (ANN) are computational networks that attempt to stimulate, in a gross manner, the decision process in networks of nerve cells (neurons) of the biological

*Corr. Author's Address: Tshwane University of Technology, Department of Industrial Engineering, South Africa, afolabiilesanmi@yahoo.com

(human or animal) central nervous system. ANNs mimic the human brain by making use of different algorithms, which allow a computer to be trained and learn by taking new information. One way in which a NN is trained is accomplished by using supervised training. Supervised training or a multi-layered feedforward (MLF) NN is when the NN knows the desired output and the adjusting of weight coefficient is done in such a way that the outputs are as close as possible [7].

The basic processing components of a NN are called artificial neurons or nodes [8]. These nodes are layered into groups of three that construct a MLF NN structure, which include: the input layer, hidden layer(s), and the output layer [7]. The input(s) are the data that are fed into the artificial intelligence (AI) and attached to the hidden layer making use of a random initial weight [8]. The hidden layer is the sum of all weights multiplied by inputs. A bias value is then added to the final equation [8]. The bias is a value that is used to shift the result of an activation function towards the positive or negative side of an output value [8].

0.2 Natural Language Processing (NLP)

MODAPTS activities are described making use of the English language. Applying machine learning to that language requires incorporating a field called natural language processing (NLP) [9]. NLP is a subfield of AI and linguistics devoted to make computers understand statements or words written in human languages [10]. Brownlee [11] simplifies the definition by stating that they are automatic manipulations of natural language, like speech and text by software.

For any NN training to take place for which the inputs consist of text, an encoding must take place to convert the text to digits so that the NN can understand it. There are two ways to encode text in preparation for a NN: one-hot encoding and word embedding [12].

Word embeddings (WE) have been proposed to represent words as dense vectors that are derived by various training methods inspired from neural-network language modelling [13]. WE are a type of word representation that allows words with similar meanings to have a similar word representation [14]. The advantage of this technique is that it allows for words to be represented as vectors in a real vector space [13].

One-hot encoding allows each word to be represented singularly, so that no two words will have the same one hot vector representation. Additionally, a one-hot vector is much simpler and high dimensional than the word embedding technique, which is dense, low dimensional, and complex [12].

0.3 Chatbots

Chatbots are machine agents that serve as natural language user interfaces for data and service providers [15]. Chatbots agents anticipate a given input (voice, text) and attempt to give a favourable response to the intended user. A simpler explanation would be a program that simulates a natural human conversation [16].

According to Lishchynska [16], there are three types of chatbots:

1. Rule-based; this is the simplest mechanism that a chatbot can use as its structure is predefined each time an interaction takes place with a user. This type of approach is favourable for small noncomplex scenarios and often requires longer interactions to give correct and relevant answers to the user.
2. Intellectually independent chatbots make use of Machine Learning (ML) to interact with a user. This is done by the chatbot learning a set of keywords or phrases to generate a response. The chatbot becomes more precise as it learns more keywords and phrases, and through continuous use by the user over time.
3. AI-powered chatbots, make use of the best practices followed by rule-based and intellectual independent approaches in that they understand language and have predefined mechanisms to solve a problem. They make use of NLP and can understand a given context to emulate a conversation as accurate as possible.

Data must be presented in a particular manner such that the bot can easily interpret and process it to create meaningful and interactive conversations [17]. Fig. 1 shows a flow chart structure of a typical ML chatbot setup.

Five phases are involved when raw input is passed into the chatbot [17]. The first phase is called tokenisation and is the process of breaking down text into simple more manageable units [18]. This is usually the first process in any NLP task [19], and it involves breaking down raw text or sentences into individual words for the training of the NN [17].

The second phase is called text processing and is the method of cleansing the tokenized words. This includes removing any punctuation marks, digits (if not needed) and stop words (words that are meaningless to the NN) [17]. The third phase would be to categorise the purified tokens into distinct groups

of classes based on the theme of the chatbot, the method is called named entity recondition [17]. The fourth phase is called intent classification and is the process of understanding what the user wants so that an intent is clearly established; this is usually done by training a NN to classify requests into intents [17]. The final phase is developing a response based on the given intent. The response must suit the theme of the chatbot.

The recurrent neural networks (RNN) are a type of an ANN and are powerful tools for modelling sequences; there are flexibly extensible and can incorporate various types of information including temporal order [20]. RNNs have the ability to remember previous inputs from previous layers as opposed to a normal NN. RNNs are not only dependant on weights and previous outputs but they are also dependant on the context from the previously derived inputs and outputs [20]. This further echoed by Donkers et al. [20] who highlighted that they are capable of incorporating input from past consumption events to derive sequence to sequence mappings.

The context approach will be very useful specifically in remembering MODAPTS activities during the experiment. However, consistent iterations of the NN will accumulate a series of inputs, which will begin to degrade the network [12]. A special RNN technique called long-short term memory (LSTM) can be used to compensate for the memory shortfall. LSTM has complicated dynamics that allow it to easily "memorize" an extended number of time steps. Fig. 1 displays the LSTM NN [21].

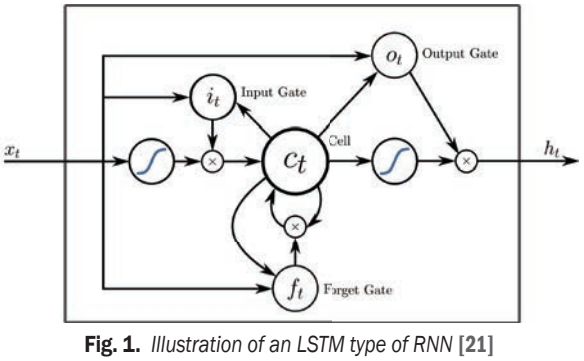

Fig. 1. *Illustration of an LSTM type of RNN* [21]

The MODAPTS is an effective method of conducting work measurement, which is due to its minimalistic coding mechanism and framework compared with other time standards such as Maynar's operations sequence technique and methods time measurement. The time standard has been applied in many industries globally and its methodology has been extended to analyse supporting factors, such as ergonomics and fine/gross motor skills.

Although the MODAPTS is versatile in application, its methodology has become dated and rather complicated, particularly when seeking to help engineers understand full systems in the present day [22]. Producing reputable time studies using MODAPTS requires a significant understanding of the many codes and rules that governs the time standard. A slight deficiency in knowledge of the time standard may lead to human error and unwanted mistakes during the observation process [3].

The time standard can be coupled with the NN to further extend its use and make it practical for an engineer to use and quickly understand for work measurement and motion analysis. This is a significant knowledge gap that has not been sufficiently explored by the existing literature. This study seeks to take advantage of the data constantly getting emitted during each MODAPTS study observation and pair that with the ML concept ANN to make the MODAPTS time standard relatable and accessible.

1 METHODOLOGY

The study employs a quantitative research approach with the overall aim of conducting an experiment to measure the total time it takes to conduct a MODAPTS time study making use of the conventional paper-based method versus the ANN approach. The focus of this methodology was extracting data from the research participants to prove that machine learning could be used to advance MODAPTS. The choice of the machine-learning approach, particularly the NN, stems from the fact that it can iteratively train the data and store information on the entire network to make predictions in a time-effective manner [23] and [24].

The testing the chatbot involved creating a Python file that would access the saved model, submit the user query, and give the prediction. Each prediction was assessed based on the intents file. If an error occurred, the intents file was then adjusted, and the model was re-trained. The chatbot was built by making use of the Python programming language, it used an ML module called Keras to train and implement the NN. The Python code was executed using an integrated development environment called PyCharm. The choice of the Python programming is due to the fact it is simple to implement, compatible, and has many libraries, such as the Keras library employed in this study, with in-built data structures [17] and [25].

The participants who took part in the research were four logistics engineers (LEs) and were selected

based on the material handling knowledge and experience that the LEs had attained. A questionnaire was given to the participants to collect information on their experience and skill level when using the MODAPTS time standard.

Data produced during a MODAPTS study is usually analysed, presented, and left as is [4]. This research method seeks to make meaningful computations out of that data, such that it becomes easier for the next engineer to implement a MODAPTS study. A large part of this research method focuses on how an engineer describes (by writing it) an observed activity. There are usually many words, lines, and sentences involved when describing an activity, and that can mean a lot of data. Introducing ANN allows for that data to be quickly organised and quantified to produce patterns and predictions [26].

ML allows for continuous improvement so that it can take a problem that has been traditionally solved and employ techniques such as genetic algorithms to improve its output [27]. This is true when looking at frameworks used to conduct MODAPTS as they have been tried and tested to produce results. The data collected from those frameworks may be used together with ML to improve the time standard. ML is vast in application and contains many fields and algorithms to solve a given problem. NLP makes it possible for the computer to learn the English language and is pivotal in teaching it MODAPTS [10].

The study used a chatbot to test interactions between the research participant and the MODAPTS NN. The chatbot was programmed to accept user input in the form of text, specifically a MODAPTS activity description. The activity descriptions were then separated into manageable smaller sentences delaminated either using a full stop or a comma.

The delaminated sentence or activity description was then fed into a trained NN to produce a prediction or response in the form of a MODAPTS code. If the prediction was successful, the code was then passed into a MODAPTS function, which converted it into the appropriate number of mods. The user would be prompted to enter the correct MODAPTS code if the prediction was incorrect, the code would also subsequently be passed into the MODAPTS function to extract the total number of modular arrangements.

1.1 Disposing of Empty Box

A material handler collects an empty box from a return chute; the material handler walks five steps to the racking location and bends below the knees to obtain the box. The material handler then walks ten steps to the waste bin and deposits the box into the waste bin. The material handler then walks back to the racking location.

Table 1 highlights the steps involved in collecting and disposing an empty box.

1.2 Line Feeding

A material handler walks five steps to the picking trolley and obtains it; the material handler then proceeds to the auto-call trolley five steps away pushing the picking trolley. The material handler then obtains two boxes (one at a time) from the auto-call trolley and places the boxes on the picking trolley beneath the knees. The material handler then takes the picking trolley to a racking location (10 steps away); he then cuts each box and position them individually to a rack position. The line feeding activities is depicted in Table 2.

1.3 Picking a Pick-to-Light (P2L)

A material handler starts by collecting a pick sheet from the printer, then checks if the sequence number on the picking sheet matches with the sequence on the display board. The material handler then takes five steps to the empty bin trolley and obtains the bin. The material handler then takes another five steps to the start of the P2L cell and positions the bin onto the picking conveyor. The material handler then proceeds to take 10 more steps while picking a total of eight

Table 1. *Disposing of an empty box*

	Collecting empties from plant 1 sequential											
1	Step to the racking location (10 steps)	5	W	5								25
2	Obtain empty box from return chute and bring to self	M	7	G	1	M	7	P	0	0	0	15
3	Step to the waste bin	10	W	5								50
4	Aside box to waste bin	M	2	P	0							2
5	Step back to racking location	10	W	5								50
											TOTAL	142

parts (pressing lights) for that zone. The material handler then returns to the printer walking 20 steps (Table 3).

1.4 Supplying P2L Bins

A material handler obtains six bins from a P2L roller conveyor and asides them onto a supply trolley. The trolley is then taken to the production line ten steps away and the material handler repacks the production trolley with the six bins. The material handler then takes the six empty bins from the return chute and places them on the supply trolley. The trolley is then taken back to the start of the P2L cell fifteen steps away (Table 4).

1.5 Sequencing a Part

A material handler walks ten steps to the printer and obtains picking list, the material handler sorts the

Table 2. *Line feeding*

	Collecting empties from plant 1 sequential												
1	Take 5 steps to the picking trolley	5	W	5									25
2	Obtain trolley	M	2	G	1								3
3	Take 5 steps to the autocall trolley	5	W	5									25
4	Obtain first box, bring to self and aside to trolley below knees	M	2	G	1	M	3	P	0	M	7	P	0	13
5	Obtain second box, bring to self and aside to trolley below knees	M	7	G	1	M	3	P	0	M	7	P	0	18
6	Obtain trolley	M	4	G	1									5
7	Take 10 steps to racking location	10	W	5										50
8	Obtain safety knife and remove from pocket	M	4	G	1	M	4	P	0					9
9	Obtain box from trolley and bring to self	M	7	G	1	M	7	P	0					15
10	Aside knife to box	M	3	P	0									3
11	Cut box on the three sides (total of 5 moves)	M	3	P	0									15
12	Obtain box flap opens it (opens all 4 sides)	M	3	P	0	M	3	P	0					24
13	Remove inner card box layer and aside box to racking location	M	3	G	1	M	3	P	0	M	3	P	2	12
14	Obtain box from trolley and bring to self	M	7	G	1	M	7	P	0					15
15	Aside knife to box	M	3	P	0									3
16	Cut box on the three sides (total of 5 moves)	M	3	P	0									15
17	Obtain box flap opens it (opens all four sides)	M	3	P	0	M	3	P	0					24
18	Remove inner cardboard box layer and aside Box to racking location	M	3	G	1	M	3	P	0	M	3	P	2	12
												TOTAL		286

Table 3. *Pick-to-light picking*

	Collecting empties from plant 1 sequential												
1	Obtain picking list from printer and bring to self	M	3	G	1	M	3	P	0				7
2	Check both digital information screen and pick sheet for sequence number	2	R	3									6
3	Take 5 steps to picking trolley with bins	5	W	5									25
4	Obtain bin and bring bin to self	M	2	G	1	M	4	P	0				7
5	Take 5 steps to conveyor at start of P2L	5	W	5									25
6	Aside bin to conveyor	M	2	P	2								4
7	Position pick sheet inside bin	M	4	P	2								6
8	Obtain and engage first light button	M	3	G	0	M	1	P	0				4
9	Wait time as system starts	T	15.4										15.4
10	Take 10 steps for the total zone	10	W	5									50
11	Obtain and engage 8 light buttons	M	3	G	0	M	1	P	0				32
12	Obtain box simo obtain part	M	4	G	1	M	4	P	0				9
13	Aside part to bin	M	4	P	0								4
14	Obtain bin and prepare to move to next light	M	3	G	1								4
15	Step back 20 steps to the printer	20	W	5									100
												TOTAL	298.4

Table 4. *Supplying pick-to-light bins*

	Collecting empties from plant 1 sequential											
1	Obtain bin from conveyor and aside onto supply trolley (×6)	M	4	G	1	M	4	P	2			66
2	Obtain trolley	M	3	G	1							24
3	Step to the production line	10	W	5								50
4	Obtain bin and pack onto roller conveyor lineside	M	2	G	1	M	4	P	2			9
5	Obtain bin and pack onto roller conveyor lineside (5 remaining picks)	M	2	G	1	M	4	P	2			45
6	Obtain and repack empty grey bins onto the supply trolley(×6)	M	4	G	1	M	4	P	2			66
7	Obtain supply trolley	M	3	G	1							4
8	Step back to the P2L cell	15	W	5								75
											TOTAL	339

Table 5. *Supplying a sequenced part*

	Collecting empties from plant 1 sequential																	
1	Walk 10 steps to the printer	10	W	5														50
2	Obtain sequence sheets from printer and bring to self	M	2	G	1	M	3	P	0									6
3	Sort them (3× sheets)	M	3	P	0	M	3	P	0	M	3	G	1	R	2			36
4	Step back to the trolley	10	W	5														50
5	Obtain tape from pocket and bring to self	M	4	G	1	M	4	P	0									9
6	Cut tape and stick on page	M	3	G	3	M	3	P	0	M	1	P	0	M	3	P	0	13
7	Aside page to trolley	M	3	P	2													5
8	Obtain scanner from pocket and scan barcode to commence picking	M	4	G	1	M	4	P	2	M	1	P	0	M	1	P	0	13
9	Check the part indicated on screen	1	R	2														2
10	Step 5 steps to part and collect it and bring to self	5	W	5														25
11	Scan part barcode	M	4	P	2	M	1	P	0	M	1	P	0					40
12	Step back to the trolley	5	W	5														25
13	Scan slot position	M	2	P	2	M	1	P	0	M	1	P	0					6
14	Aside part into scanned position	M	3	P	2													5
																	TOTAL	285

picking list until the designated list is found. The material handler steps back to the sequence trolley and obtains tape. The material handler tears off a section of the tape and sticks it to the sequence sheet and then pastes the page onto the trolley. The material handler then obtains a scanner and scans the trolley to see the first part to be picked. The material handler then walks five steps to the part and obtains it. The material handler then scans the part and walks five steps back to the trolley. The material handler then scans the trolley and deposits the part onto the slot of the trolley (Table 5).

1.6 Data Preparation for the Chatbot NN

The following code was adapted from the work created by Pykes **[25]** on his implementation of a chatbot. A "training.py" file was created to hold all subroutines needed to train the chatbot.

The first step was to obtain the "intents.js" file and cycle through all intents to get access to each pattern. The patterns were then tokenized, and each token was added to a words list followed by the pattern and tag getting added to their own list. The tokenisation process is presented as follows:

```
# This will get use the stem of the word
Lemmatizer= WordNetLemmatizer ()
Data=json.loads(open('intents.json').read())
# list to hold all of the tokenized words
words = []
# list to hold all of the tags from the json string
classes = []
# associated inputs
doc_x = []
# associated outputs
doc_y = []
for intent in data["intents"]
for pattern in internt["intents"]:
tokens=nltk.word_tokenized(pattern)
words.extend(tokens)
doc_x.append(pattern)
doc_y.append(intent["tag"])
```

The next phase was to lemmatize the tokenised words to find all inflected words for that token. The

words were then converted to lowercase for each word that did not appear on the punctuation list. The words list and tags (classes list variable) were then sorted into alphabetical order ignoring any duplicated values. The code for the lemmatizing process is presented as follows:

```
words = [lemmatizer.lemmatize(word.lower()) for word
    in words if word not in string.punctuation]
words = sorted(set(words))
classes = sorted(set(classes))
```

1.7 Training the Chatbot NN

The NN was expected to be fed numerical values to train the chatbot, hence the word list made use of the "bag of words" technique to achieve that requirement. Once the bag of words was attained then the X and Y (features and target labels) parameters needed to feed the NN were defined. Fig. 2 shows a code snippet to establish the "X" and "Y" parameter.

```
# creating the bag of words model
for idx, doc in enumerate(doc_x):
    bow = []
    text = lemmatizer.lemmatize(doc.lower())
    for word in words:
        bow.append(1) if word in text else bow.append(0)
    # mark the index of class of class that the current pattern is associated
    # to
    output_row = list(out_empty)
    output_row[classes.index(doc_y[idx])] = 1
    # add the one not encoded Bow and associated classes to training
    Training.append([bow, output_row])
# shuffle the data and convert it to an array
random.shuffle(training)
training = np.array(training, dtype=object)
# split the features and target labels
train_x = np.array(list(training[:, 0]))
train_y = np.array(list(training[:, 1]))
```

Fig. 2. *Code snippet of the features and targets generation*

The NN was structured to predict a given response based on the associated tag when feeding features as inputs [25]. The NN model was a sequential model with three primary layers (input-hidden-output) and two dropout layers that randomly adjusted the inputs to 0. The input layer was dense and contained 128 neurons and used an activation function called the rectified linear unifier (ReLU). The next layer was a hidden dense layer with 64 neurons also using the ReLU as its activation function. The last layer was a dense output layer using the SoftMax as its activation function.

The model used an Adam optimiser with a learning rate of 1 % and was trained for 200 cycles (epochs). Fig. 3 shows the dense NN structure of the chatbot.

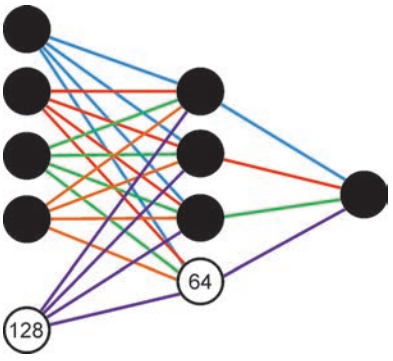

Fig. 3. *Dense structure of the NN*

The model was trained and then saved under the name "chatbot2.h5". Fig. 4 shows a code snippet of the training process.

```
input_shape = (len(train_X[0]),)
output_shape = len(train_y[0])
epochs = 200
# the deep learning model
model = Sequential()
model.add(Dense(128, input_shape=input_shape, activation="relu"))
model.add(Dropout(0.5))
model.add(Dense(64, activation="relu"))
model.add(Dropout(0.3))
model.add(Dense(output_shape, activation = "softmax"))
adam = tf.keras.optimizers.Adam(learning_rate=0.01, decay=1e-6)

model.compile(loss='categorical_crossentropy',
              optimizer=adam,
              metrics=["accuracy"])

hist = model.fit(x=train_X, y=train_y, epochs=200, verbose=1)
model.save('chatbot2.h5', hist)
print("Done")
```

Fig. 4. *Code snippet of the NN chatbot training phase*

1.8 Chatbot Application

The chatbot application was a simple webpage that captured user input in the form of MODAPTS activities. An initial signup or login screen was needed to gain access to user data and select the scenario. The selected scenario was represented by a button on the main screen interface. Pressing the scenario button would bring up a dialog box containing scenario data. This action could be accessed anytime during the experiment for scenario reference. The main interface also consisted of a prediction button and an input field that was used by the research participant to submit the query to the chatbot NN. A single input field was used to key in user data and was required to be entered each time the prediction button was pressed. The application would present a dialog box with the predicted MODAPTS code when the prediction button was pressed. The user would then select the code if

the prediction was true or manually input the correct code if the chatbot NN presented a false prediction. Each prediction was summarized at the main screen interface shown as a scrollable list. Each list item showed the MODAPTS code, activity description, MODS for that activity, and the total duration taken for that list item. Each MOD from the list items were collectively added together and shown on the main screen and changes each time an activity was added or removed from the list.

The application made use of several timestamps to track movement done by the user and the performance of the chatbot during the experiment.

The chatbot NN was programmed to expect a structured user query from the research participant. The activity was done first by describing a terminal action, then followed by the movement class and then finally the level of difficulty to perform the action.

2 RESULTS AND DISCUSSION

This section discusses the research results and analysis of the quantitative data obtained from the four research participants. The section is divided into two parts, the first part interpreted results from the questionnaire in relation to all participants while the second part focuses on the results and analysis obtained when conducting a traditional MODAPTS study.

The third part focused on the results and analysis of the Machine Learning approach of conducting the same MODAPTS study. The last part compared the two approaches in relation to the final duration with aid of a t-test analysis.

2.1 Questionnaire Results

The following tables show results obtained from the questionnaire, a total of seven questions were presented to the research participants to understand their work experience and their role in using MODAPTS.

Table 6 shows the current industry in which the research participants are working.

Table 6. *Work industry*

Industries	Score
Automotive	4
Energy, utilities, and mining	0
Government and public sector	0
Technology	0
Other	0

The research participants all work currently for the automotive industry. Their focus is on material handling activities affecting people, the production line, and their customer overall.

Table 7 describes the work experience in years each research participant possesses in the selected work environment.

Table 7. *Research MODAPTS experience*

Experience	Score
Less than 3 years	1
Less than 6 years	2
Greater than 6 years	1

There was only one research participant with less than three years of experience using MODAPTS, the remaining participants were highly qualified with more than three years of experience.

Table 8 describes the work measurement techniques that each participant used at the workplace.

Table 8. *Work measurement techniques*

Work measurement	Score
General estimation	1
Stopwatch analysis	2
Predetermined motion time systems	4

Each research participant made use of predetermined motion time systems (PMTS) to conduct daily time studies. Half the research participants made use of stopwatch analysis to become familiar with the process before applying PMTS. Only one research participant made use of general estimation but that was done as a forethought with regards to planning an activity.

Table 9 shows certification status of each research participant.

Table 9. *Work measurement certification*

Certification	Score
Yes	3
No	1

Three out of the four research participants had been trained and certified to use MODAPTS. The remaining research participant had yet to be trained and learned from stored MODAPTS company user manuals.

Table 10 shows the total duration taken to conduct a MODAPTS time study.

There was a total of two people who conducted MODAPTS studies in four hours; the remaining

participants took a day or more to complete the studies. The extended length in conducting a MODAPTS study was due to the need for accuracy rather than inexperience.

Table 10. *Duration of study*

Duration of time study	Score
2 hours	0
4 hours	2
1 day	1
more than 1 day	1

Table 11 shows the uses of the MODAPTS time standard employed.

Table 11. *MODAPTS study usage*

Time study function	Score
Efficiencies	4
Rebalancing of work	4
Time keeping	2
Other	0

Each research participant uses MODAPTS for efficiencies and to rebalance workload as part of customer requirements and managing resources. Only two research participants used MODAPTS for time keeping.

Table 12 shows for whom the MODAPTS time study is intended.

Table 12. *MODAPTS study designation*

Time study designation	Score
Top management	2
Middle management	4
Shop floor staff	0

Table 13. MODAPTS presentation format

Time study presentation	Score
Raw Data	2
Graphical	3
Key performance indicators	1
Other	1

The majority of the research participants chose middle management to present their findings. Presenting to this level was due to middle management needing to prove validity of resources to the customer or top management. There were only two people that selected the top management. Three out of the four research participants selected graphical presentation as it was easier and quicker to convey the intended message. Raw data were also used, mostly to show variance in a process activity element by element. Table 13 shows the presentation format used by the research participants.

2.2 MODAPTS Chatbot Analytics

A series of measurements were collected from the research participants while using the chatbot. These measurements were used to establish interaction between the research participant and the NN chatbot. Each measurement was captured and sent to a unique database table on the created server. The measurements included: prediction accuracy, progressive rate, activity formulation, error accumulation and total duration.

2.3 Prediction Accuracy

Prediction accuracy measures the performance of the trained NN application, focusing on the number of successful predictions against the total number of incorrect predictions. The application does this by keeping a count of keypresses each time the prediction and manual buttons are pressed.

Table 14. *Predictions table*

Scenario	Manual	Predictions	Total
SC1	1	18	19
SC2		52	52
SC3	4	50	54
SC4		84	84
SC5	9	44	53
Total	14	248	262

Source: Researcher's synthesis

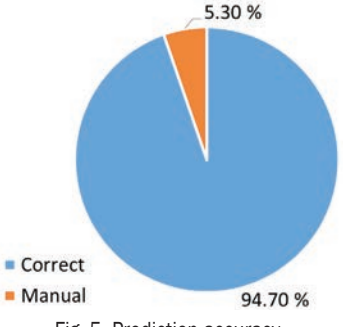

Fig. 5. Prediction accuracy

A total of 262 activities were entered by all four research participants; 248 (94.7 %) were successful predictions made by the NN and only 14 (5.3 %) were manually entered codes to correct the ANN chatbot. Looking at the manual entries, there were a

total of 9 MODAPTS related errors produced by the chatbot relating to the codes "E", "R", and the "finger-movement". The remaining manual entries were due to a dialect miscommunication between the research participant and the chatbot. Table 14 shows the total number of predictions against manual predictions.

Fig. 5 shows the percentage difference between total manual predictions against the correct predictions made by the ANN chatbot.

2.4 Progressive Rate

The progressive rate is a measure that calculates the response time of each research participant moving from one element (buttons, inputs, etc.) to another in the NN application. The measure was applied to establish how quickly a research participant used and understood the NN application.

Table 15 shows the average time (in seconds) that the research participants took to move from one element in the NN application to the next throughout each scenario.

Table 15. *Application element times [s]*

Elements	SC1	SC2	SC3	SC4	SC5	Average
Inactive - Scenario Button Open	6.06	2.88	3.32	3.74	3.66	3.75
Prediction Button Close - Main Input	4.88	4.85	4.81	3.92	6.33	5.02
Prediction Button Open - Prediction Button Confirm	4.22	3.23	2.25	1.81	2.13	2.42
Average	5.07	3.33	2.95	2.34	3.32	

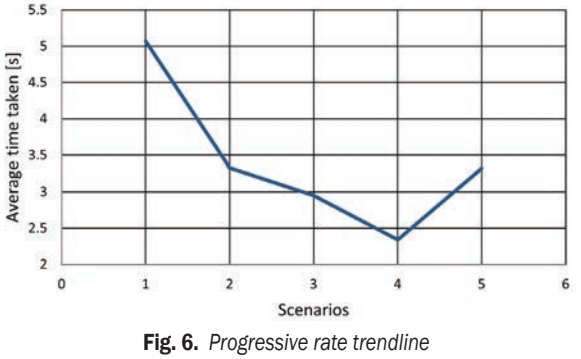

Fig. 6. *Progressive rate trendline*

Scenario 1 (SC1) showed that the research participants spent more time navigating around the template on average at 5.07 s. This was expected as the template was new to each research participant. The time dropped significantly through each proceeding scenario at average of 2.99 s (SC2 to SC5). A percentage decrease was calculated and found a drop rate to be 41.02 % from the initial scenario time. Fig. 6 shows the trendline with regards of the progressive rate.

2.5 Activity Formulation

Activity formulation is a measure that keeps track of the number of entered activities and the time spent observing the scenario description by the research participant. The measure correlates the time spent viewing a scenario description with the number of produced activities by the ANN template from the research participant. Table 16 shows the duration and corresponding activities of each scenario.

A total of 262 activities was entered collectively by all research participants. A total duration of 370 minutes was spent viewing the activity scenario descriptions by all research participants. The number of entered activities directly impacted the total time a scenario activity was viewed.

Table 16. *Scenario description viewing duration*

Elements	SC1	SC2	SC3	SC4	SC5	TTE
Duration	54	85	80	58	93	370
Activities	19	52	54	84	53	262

2.6 Paired T-Test – ANN against Traditional MODAPTS

The following analysis tests for a statistical difference when conducting a MODAPTS study traditionally against the ANN Chatbot alternative. Participant 4 was removed from the final analysis as their final time was an outlier toward the rest of the research participants. The analysis makes use of a paired t-test analysing the total durations of each scenario from the two groups, as shown in Table 17.

Table 17. *Error entities by scenario*

Scenario	Traditional	ANN
SC1	13.30	19
SC2	37.65	27
SC3	30.90	23
SC4	18.82	38
SC5	39.60	32
Mean	28.05	27.80

The following analysis made use of Excel's t-test function to compute the P-value.

The t-test was paired so that the two groups were compared looking at five scenarios, with no reference

from each other. The mean difference between the two methods is 0.25 minutes, the t-test was calculated at 95 % confidence level (0.05) and produced a P-value of 0.9663. The computed P-value was greater than the 0.05 showing that no significant difference between the two generated studies.

3 CONCLUSION AND RECOMMENDATIONS

The objective of the study was to apply NN to MODAPS. This was achieved by gathering training data in the form of MODAPTS keywords. Training data were acquired as raw data in the form of MODAPTS time studies. This data, however, were then broken and processed to extract the keywords for the training of the NN. The NN was also trained with the data collected using the TensorFlow algorithm assisted by the Keras library. This was achieved by first learning the fundamentals of creating a NN. Thereafter, consolidating several tools, such as the Python programming language and the Keras library, were used to implement the ANN. The approach of this ANN made use of a chatbot application, such that the collected keywords would be trained in the NN and act as dialect for the chatbot when in conversation with the research participant.

After conducting a successful study, the following could be concluded:

1. 94.7 % successful predictions were made by the NN while only 5.3 % were manually entered codes to correct the ANN chatbot. The mean difference between the two methods is 0.25 minutes, the t-test was calculated at 95 % confidence level (0.05) and produced a P-value of 0.9663. The computed P-value was greater than the 0.05 showing that there is no significant difference between the two generated studies.
2. The ANN approach could replace tedious tasks of manually conducting MODAPTS using spreadsheets and other laborious methods.
3. Although some degree of MODAPTS knowledge is required, the time for a novice engineer to learn and understand the time standard would have greatly reduced.
4. The chatbot is able keep track of user events, such that more patterns besides the ones mentioned in this research could be developed for the continual benefit of the engineer and study.

The results show that the MODAPTS enabled by machine learning applications such as the NN can replace the tedious MODAPTS analysis on the computer with a mobile alternative that consistently records the user and study analytics to improve the overall analysis. The MODAPTS-ANN template demonstrated in this study possesses great potential to improve and refine work measurement. Furthermore, the template is flexible enough to be moulded into a tool that all engineers can adapt to their different working environments, not only the automotive industry.

It can make the data sharing amongst engineers easier owing to its descriptive database. Hence, there is a potential to add other ML learning techniques to time study methods. The novelty of this study lies in the fact that the coupling of the MODAPTS with NN to further extend the use of MODAPTS and make it practical for an engineer to use and understand it quickly for work measurement and motion analysis has not been sufficiently highlighted by the existing literature. The ANN approach makes it far easier to implement MODAPTS in multiple industries owing to the customisable keywords and dialect recognition of the chatbot.

The study is limited to the MODAPTS time standard in relation to material handling activities conducted by the logistics company, DSV. The process activities were sourced from actual feasibility studies conducted by logistics engineers carried out throughout each study observation with a focus falling on the keywords. The study also explored the use of machine learning in the form of NNs with a view to applying them to chatbots. This included its functionality regarding the building blocks of a simple NN structure, the activity of training the NN through these collected process keywords, and the delivery of the template. This study did not build a NN from scratch but rather to make use of an open-source library called Keras to assist with all NN-training activities. Hence, the combination of the NN and MODAPTS is recommended for conducting work measurement and motion analysis in the industry.

The newly proposed approach was compared with the traditional approach and the mean difference between the two methods was 0.25 minutes. This implies that this approach still has room for improvement. Therefore, future work can consider improving the vocabulary of the chatbot; this is to allow for a more natural flow of communication when conversating with the chatbot. This would require going deeper in research field of NLP to understand and to gain more tools to make this possible.

4 REFERENCES

[1] Golpîra, H. (2013). Estimating duration of projects manual tasks using MODAPTS plus method. *International Journal of Research in Industrial Engineering*, vol. 2, vol. 1, p. 12-19.

[2] Cho, H., Park, J. (2014). Motion-based method for estimating time required to attach self-adhesive insulators. *Computer-Aided Design*, vol. 56, p. 68-87, **DOI:10.1016/j.cad.2014.06.004**.

[3] Mallembakam, V.R. (2020). Incorporating modular arrangement of predetermined time standard with a wearable sensing glove. *Electronic Theses and Dissertations*, 8524, University of Windsor, Windsor.

[4] Kumar, R., Charak, A., Thakur, G. (2020). Productivity improvement of an automotive assembly line using modular arrangement of predetermined time standards (MODAPTS). *i-Manager's Journal on Future Engineering and Technology*, vol. 16, no. 2, p. 32-42, **DOI:10.26634/jfet.16.2.17694**.

[5] Cho, H., Lee, S., Park, J. (2014). Time estimation method for manual assembly using MODAPTS technique in the product design stage. *International Journal of Production Research*, vol. 52, no. 12, p. 3595-3613, **DOI:10.1080/00207543.2013.878480**.

[6] Graupe, D. (2013). *Principles of Artificial Neural Networks*, University of Illinois, Chicago, World Scientific, **DOI:10.1142/8868**.

[7] Svozil, D., Kvasnicka, V., Pospichal, J.Í. (1997). Introduction to multi-layer feed-forward neural networks. *Chemometrics and Intelligent Laboratory Systems*, vol. 39, no. 1, p. 43-62. **DOI:10.1016/S0169-7439(97)00061-0**.

[8] Abraham, A. (2005). *Artificial Neural Networks. Handbook of Measuring System Design*. John Wiley & Sons, London, **DOI:10.1002/0471497398.mm421**.

[9] Landset, S., Khoshgoftaar, T.M., Richter, A.N., Hasanin, T. (2015). A survey of open source tools for machine learning with big data in the Hadoop ecosystem. *Journal of Big Data*, vol. 2, no. 24, **DOI:10.1186/s40537-015-0032-1**.

[10] Chopra, A., Prashar, A., Sain, C. (2013). Natural language processing. *International Journal of Technology Enhancements and Emerging Engineering Research*, vol. 1, p. 131-134.

[11] Brownlee, J. (2017). Deep learning for natural language processing: develop deep learning models for your natural language problems. *Machine Learning Mastery*. Edition v1.1, p. 1-414.

[12] Nelson, D. (2021). Text Generation with Python and Tensor/Flow. Available from: *https://stackabuse.com/text-generation-with-python-and-tensorflow-keras*, accessed on 2021-07-30.

[13] Levy, O., Goldberg, Y. (2014). Dependency-based word embeddings. *Proceedings of the 52nd Annual Meeting of the Association for Computational Linguistics,* vol. 2: Short Papers, p. 302-308, **DOI:10.3115/v1/P14-2050**.

[14] Agrawal, S. (2019). What the heck is word embedding, from: *https://towardsdatascience.com/what-the-heck-is-word-embedding-b30f67f01c81*, accessed on 2020-08-01.

[15] Brandtzaeg, P.B., Følstad, A. (2017). Why people use chatbots. Internet Science. *Lecture Notes in Computer Science*, vol. 10673, p. 377-392, Springer, Cham, **DOI:10.1007/978-3-319-70284-1_30**.

[16] Lishchynska, D. (2017). What are bots, how do chat bots work? from: *https://botscrew.com/blog/what-are-bots/#:~:text=Chatbot%20or%20bot%20%E2%80%93%20is%20a,an%20instant%20pre%2Dset%20answer*, accessed on 2021-02-01.

[17] Manaswi, N.K. (2018). Developing chatbots. Deep Learning with Applications Using Python. *APress*, Berkeley, **DOI:10.1007/978-1-4842-3516-4_11**.

[18] Reese, R.M., Bhatia, A. (2018). *Natural Language Processing with Java: Techniques For Building Machine Learning and Neural Network Models for NLP*, Packt Publishing Ltd., Birmingham.

[19] Park, K., Lee, J., Jang, S., Jung, D. (2020). An empirical study of tokenization strategies for various Korean NLP tasks. *arXiv* preprint arXiv:2010.02534, **DOI:10.48550/arXiv.2010.02534**.

[20] Donkers, T., Loepp, B., Ziegler, J. (2017). Sequential user-based recurrent neural network recommendations. *Proceedings of the 11th ACM Conference on Recommender Systems*, p. 152-160, **DOI:10.1145/3109859.3109877**.

[21] Zaremba, W., Sutskever, I., Vinyals, O. (2014). Recurrent neural network regularization. *arXiv*, preprint arXiv:1409.2329, from *http://arxiv.org/abs/1409.2329*.

[22] Wu, S., Wang, Y., Bolabola, J.Z., Qin, H., Ding, W., Wen, W., Niu, J. (2016). Incorporating motion analysis technology into modular arrangement of predetermined time standard (MODAPTS). *International Journal of Industrial Ergonomics*, vol. 53, p. 291-298, **DOI:10.1016/j.ergon.2016.03.001**.

[23] Daniyan, I.A., Tlhabadira, I., Mpofu, K., Adeodu, A.O. (2020). Development of numerical models for the prediction of temperature and surface roughness during the machining operation of titanium alloy (Ti6Al4V). *Acta Polytechnica Journal*, vol. 60, no. 5, p. 369-390, **DOI:10.14311/AP.2020.60.0369**.

[24] Daniyan, I.A., Mpofu, K., Tlhabadira, I. Ramatsetse, B.I. (2021). Process design for milling operation of titanium alloy (Ti6Al4V) using artificial neural network. *International Journal of Mechanical Engineering and Robotics Research*, vol. 10, no. 11, p. 601-611, **DOI:10.18178/ijmerr.10.11.601-611**.

[25] Pykes, K. (2021). Build A Simple Chatbot In Python with Deep Learning. available from: *https://towardsdatascience.com/a-simple-chatbot-in-python-with-deep-learning-3e8669997758*, accessed on 2022-03-31].

[26] Alpaydin, E. (2021). *Machine Learning*, MIT Press, Massachusetts, **DOI:10.7551/mitpress/13811.001.0001**.

[27] Aissani, N., Beldjilali, B., Trentesaux, D. (2008). Use of machine learning for continuous improvement of the real time heterarchical manufacturing control system performances. *International Journal of Industrial and Systems Engineering*, vol. 3, no. 4, p. 474-497, **DOI:10.1504/IJISE.2008.017555**.

Strojniški vestnik - Journal of Mechanical Engineering 69(2023)1-2, 73-81
DOI:10.5545/sv-jme.2022.375
Original Scientific Paper
Received for review: 2022-09-24
Received revised form: 2022-12-25
Accepted for publication: 2023-01-19

Analytical Formulae and Applications of Vertical Dynamic Responses for Railway Vehicles

Yuewei Yu – Yunpeng Song – Leilei Zhao* – Changcheng Zhou
Shandong University of Technology, School of Transportation and Vehicle Engineering, China

To effectively improve the estimated level of railway vehicles' vertical dynamic responses and provide a more suitable reference for the selection of its secondary suspension damping parameter, this paper has derived the root mean square values analytical formulae of the car body vertical acceleration, the secondary suspension vertical stroke, and the axle box vertical action force for railway vehicles under the random excitation of the track closer to the actual track characteristics. The correctness of the analytical formulae is verified by testing a real vehicle. Then, according to the analytical formulae derived, an analytical design method of the optimal damping ratio for the secondary suspension system is constructed based on the multi-objective programming and single-objective interval constraint analysis, which can be used to find the best trade-off for conflicting performance indices, such as ride comfort, running smoothness, and running safety, and the influences of the system parameters on the optimal damping ratio are analysed. This research can effectively characterize the vertical vibration response of railway vehicles and provide an effective reference for the initial design of the railway vehicle secondary suspension damping parameter.

Keywords: railway vehicle, vertical dynamic response, model deduction, damping parameter design, optimal compromise

Highlights

- *The analytical formulae of the vertical dynamic response for railway vehicles were derived.*
- *An optimal damping ratio design method for the secondary suspension system was constructed.*
- *The influences of the system parameters on the optimal damping ratio were analysed.*

0 INTRODUCTION

As bogie suspension system parameters are essential for the running stability, safety, and comfort of railway vehicles, the design of their suspension system parameters has become an important part of the bogie system design and has become a key concern for designers [1].

Generally, a bogie suspension system is composed of the elastic element and the damper element; it mainly includes two important parameters to be designed, i.e., the spring static deflection value and the suspension damping parameter value. In order to obtain an accurate and reliable design result for the suspension damping parameter, one widely used method is to use computer simulation technology and vehicle dynamic analysis software to optimize and determine the final value [2] to [4]. This method can simulate the actual operation of railway vehicles well [5] and [6] and can achieve a more accurate design result. However, the simulation analysis requires much time and cannot visually show the one-to-one correspondence between parameters and responses, which is not conducive to the adjustment and optimization of the structural parameters in the initial design stage of suspension systems. Meanwhile, the suspension parameter values before design are often unknown. The complexity of the model makes it complicated to do much work to design the suspension damping parameters, which is not conducive to the designers making a reasonable engineering choice quickly and effectively. In order to solve this problem, the most effective method is to use the analytical method, i.e., through reasonable model simplification, from the theoretical analysis point of view, and then obtain the required design value of the damping parameters [7] to [9]. For this reason, based on the simplified 1/4 vehicle model, using the simplified track irregularity power spectral density (of the form $1/\omega^4$ and $1/\omega^2$) as the input excitation of the system, the analytical formula for calculating the root mean square (RMS) value of the bogie frame vertical acceleration for railway vehicles is derived, and an analytical design method for the primary vertical suspension damping ratio of railway vehicles is given in [1] and [10], respectively. In addition, according to the simplified 1/4 vehicle model (mainly refers to the two-axle bogie railway vehicle), using the simplified track irregularity power spectral density (of the form $1/\omega^4$ and $1/\omega^2$) as the input excitation of the system, the analytical formulae for calculating the RMS values of the car body vertical acceleration, the secondary suspension vertical stroke, and the axle box vertical action force for railway vehicles are derived; an analytical design method for the secondary vertical suspension damping ratio of railway vehicles is given in [11] and [12].

*Corr. Author's Address: Shandong University of Technology, Zibo, China, zhaoleilei611571@163.com

However, compared with the power spectral density of the form $1/[(\omega^2+v_2\Omega_c^2)\ (\omega_2+v^2\Omega_r^2)]$, which is widely used in the dynamic simulation of railway vehicles, the power spectral density of the form $1/\omega^4$ overestimates and underestimates in the low-frequency and high-frequency parts of the track irregularity, respectively, and the power spectral density of the form $1/\omega^2$ overestimates in both the low-frequency and high-frequency parts of the track irregularity.

Thus, in this paper, using the Germany track vertical irregularity power spectral density, which is closer to the actual track line, as the input excitation of the vehicle system, based on the analytical method, the RMS values analytical formulae of the vertical dynamic response of railway vehicles under the excitation of the form of $1/[(\omega^2+v_2\Omega_c^2)(\omega_2+v^2\Omega_r^2)]$ are deduced, and a more reasonable analytical design method for the secondary vertical suspension damping ratio of railway vehicles is given. As an extension and supplementing **[11]** and **[12]**, it will provide effective technical support for the engineering selection of the bogie vertical suspension system parameters to deeply explore the vertical dynamic of railway vehicles on actual track lines in the theoretical analysis field.

1 SYSTEM MODEL

1.1 Vertical Vibration Model of Railway Vehicles for Analytical Calculation

Because of the weak coupling between the vertical and lateral dynamic behaviours of railway vehicles, when analysing its dynamic performance, they are often modelled separately and analysed separately, which can simplify the model establishment and facilitate the result analysis **[13]** on the premise of ensuring sufficient analysis accuracy. Numerous studies have shown that the commonly used vertical dynamic models of railway vehicles mainly include three types **[14]** to **[16]**: the 1/4 vehicle model, the single vehicle model, and the multi-marshalling vehicle model; each of the models has its advantages and its application occasions. Here, the 1/4 vehicle model is widely used in the analytical design of the suspension system parameters **[10]** to **[12]** and the semi-active and active suspension control research **[17]** and **[18]**, because of its advantages of easy qualitative understanding of the relationship between the vehicle vertical dynamic characteristics and the structural parameters, simple solving process and easy engineering application. Therefore, in order to construct the analytical calculation model of the vertical dynamic response of railway vehicles and to provide effective guidance for the initial design of the secondary suspension damping parameter, this paper takes the 1/4 railway vehicle model **[11]** (which mainly contains two bogies per carriage, two wheelsets per bogie) as the model reference and carries out various research work, as shown in Fig. 1.

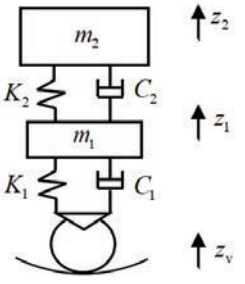

Fig. 1. *1/4 vehicle model*

In Fig. 1, m_1 is the half mass of the bogie frame; m_2 is the quarter mass of the car body; K_1 and K_2 are the vertical equivalent stiffness of the primary suspension and the secondary suspension; C_1 and C_2 are the vertical equivalent damping of the primary suspension and the secondary suspension; z_1 and z_2 are the vertical displacements of the bogie frame and the car body; z_v is the track irregularity.

According to the d'Alembert principle, the vibration differential equations of the 1/4 vehicle model can be obtained.

$$\begin{cases} m_1\ddot{z}_1 + C_1(\dot{z}_1-\dot{z}_v) + C_2(\dot{z}_1-\dot{z}_2) + K_1(z_1-z_v) \\ \qquad\qquad + K_2(z_1-z_2) = 0 \\ m_2\ddot{z}_2 + C_2(\dot{z}_2-\dot{z}_1) + K_2(z_2-z_1) = 0 \end{cases}. \quad (1)$$

By using Fourier transform, the transfer functions between $\ddot{z}_2$ and z_v, f_d and z_v, F_d and z_v can be solved respectively according to Eq. (1), as follows:

$$H(\mathrm{j}\omega)_{\ddot{z}_2\sim z_v} = \frac{C_1C_2\omega^4 - (C_1K_2+C_2K_1)\mathrm{j}\omega^3 - K_1K_2\omega^2}{\left[m_1m_2\omega^4 - (C_1m_2+C_2m_1+C_2m_2)\mathrm{j}\omega^3 + K_1K_2 - (C_1C_2+K_1m_2+K_2m_1+K_2m_2)\omega^2 + (C_1K_2+C_2K_1)\mathrm{j}\omega\right]}, \quad (2)$$

$$H(\mathrm{j}\omega)_{f_d\sim z_v} = \frac{C_1m_2\mathrm{j}\omega^3 + K_1m_2\omega^2}{\left[m_1m_2\omega^4 - (C_1m_2+C_2m_1+C_2m_2)\mathrm{j}\omega^3 + K_1K_2 - (C_1C_2+K_1m_2+K_2m_1+K_2m_2)\omega^2 + (C_1K_2+C_2K_1)\mathrm{j}\omega\right]}, \quad (3)$$

$$H(\mathrm{j}\omega)_{F_d\sim z_v} = \frac{\left[-C_1m_1m_2\mathrm{j}\omega^5 - (C_1C_2m_1+C_1C_2m_2+K_1m_1m_2)\omega^4 + (K_1C_2+C_1K_2)(m_1+m_2)\mathrm{j}\omega^3 + K_1K_2(m_1+m_2)\omega^2\right]}{\left[m_1m_2\omega^4 - (C_1m_2+C_2m_1+C_2m_2)\mathrm{j}\omega^3 + K_1K_2 - (C_1C_2+K_1m_2+K_2m_1+K_2m_2)\omega^2 + (C_1K_2+C_2K_1)\mathrm{j}\omega\right]}, \quad (4)$$

where, f_d is the secondary suspension vertical stroke $f_d=z_2-z_1$; F_d is the axle box vertical action force $F_d = C_1(\dot{z}_1 - \dot{z}_v) + K_1(z_1 - z_v)$.

1.2 Excitation Model of Track Irregularity

As the main excitation source of the vertical vibration of railway vehicles, the random input of the track vertical irregularity is basically a stationary random process along the track. Usually, according to the measured irregularity data of the track, the mathematical statistics is made, and the irregularity is expressed as the power spectral density form by interpolation processing [19]. The research indicates that there are mainly three kinds of analytical expressions for the track irregularity power spectral density commonly used in the research of railway vehicles at present, as shown in Eqs. (5), (6), and (7). The power spectral densities shown in Eqs. (5) and (6) are mainly used in the analytical calculation of railway vehicle dynamics and the semi-active and active suspension control research. The power spectral density shown in Eq. (7) is the closest to the actual track line and is widely used in the dynamic simulation analysis of railway vehicles [19].

$$S_{v1}(\omega) = \frac{A_b(2\pi v)^3}{\omega^4}, \tag{5}$$

where, A_b is the track roughness coefficient, A_b=0.928× 10^{-10} m^{-1}, v is the vehicle speed.

$$S_{v2}(\omega) = \frac{2\pi A_r v}{\omega^2}, \tag{6}$$

where, A_r is the track roughness coefficient, A_r = 2.5×10^{-7} m.

$$S_{v3}(\omega) = \frac{2\pi A_v \Omega_c^2 v^3}{\left(\omega^2 + v^2\Omega_c^2\right)\left(\omega^2 + v^2\Omega_r^2\right)}, \tag{7}$$

where, A_v is the track roughness coefficient, A_v= 4.032×10^{-7} m; Ω_c and Ω_r are the truncated spatial frequencies, Ω_c=0.824 6 m^{-1}, Ω_r=0.020 6 m^{-1}.

According to Eqs. (5) to (7), the power spectral density functions of the track irregularity at 300 km/h are expressed in the double logarithmic coordinate system, as shown in Fig. 2. It can be seen from the figure that, the power spectral densities shown in Eqs. (5) and (6) are straight lines with slopes of -4:1 and -2:1, respectively. The power spectral density shown in Eq. (7) can be approximated to a combination of three slopes (0:1, -2:1, -4:1). Compared with Eq. (7), Eq. (5) overestimates and underestimates in the low-frequency and high-frequency parts of the track irregularity, respectively; Eq. (6) overestimates in both the low-frequency and high-frequency parts of the track irregularity, but it is consistent with the actual line in the mid-frequency range.

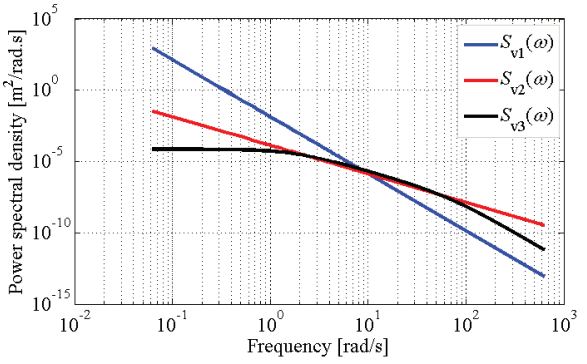

Fig. 2. *Power spectral density curve of track irregularity*

2 ANALYTICAL DESCRIPTION OF THE RAILWAY VEHICLE VERTICAL DYNAMICS RESPONSE

To quickly and effectively characterize the vertical vibration response of railway vehicles in actual operation and to enable designers to make reasonable judgments and choices on the initial design values of the system parameters quickly, using the power spectral density of the track irregularity shown in Eq. (7) as the input excitation source of the railway vehicle, the RMS values analytical formulae of the railway vehicle vertical dynamic response will be solved in this section. Note that the RMS values analytical formulae of the railway vehicle vertical dynamic response under the power spectral densities shown in Eqs. (5) and (6) can be found in references [11] and [12], respectively, which will not be introduced here.

2.1 RMS Values of the railway Vehicle Vertical Vibration Response

In the study of railway vehicle dynamics, the RMS values of the system response are usually used to evaluate the vibration characteristics and isolation effect of the vehicle system [11], [12] and [14]. According to the theory of random vibration, the following equation can be obtained.

$$\sigma_x^2 = \int_{-\infty}^{+\infty} \left| H(j\omega)_{x\sim z_v} \right|^2 S_v(\omega) d\omega. \tag{8}$$

Here, x represents the response of the system, $H(j\omega)_{x\sim z_v}$ is the transfer function, $S_v(\omega)$ is the power spectral density of the system input.

For a linear system, the following relationship exists between its amplitude-frequency characteristics:

$$\left|H(\mathrm{j}\omega)_{x\sim z_v}\right|^2 = H(\mathrm{j}\omega)_{x\sim z_v} H(-\mathrm{j}\omega)_{x\sim z_v}. \quad (9)$$

Therefore, according to Eq. (9), Eqs. (2) to (4) can be expressed as follows

$$\left|H(\mathrm{j}\omega)_{x\sim z_v}\right|^2 = \frac{N(\mathrm{j}\omega)N(-\mathrm{j}\omega)}{D(\mathrm{j}\omega)D(-\mathrm{j}\omega)}, \quad (10)$$

where, $N(\mathrm{j}\omega)$ and $D(\mathrm{j}\omega)$ are the numerator and the denominator of the Eq. (2), Eq. (3) and Eq. (4), respectively.

In addition, the power spectral density function shown in Eq. (7) can be rewritten as follows:

$$S_{v3}(\omega) = \frac{2\pi A_v \Omega_c^2 v^3}{(v\Omega_c + \mathrm{j}\omega)(v\Omega_c - \mathrm{j}\omega)(v\Omega_r + \mathrm{j}\omega)(v\Omega_r - \mathrm{j}\omega)}, \quad (11)$$

Thus, according to Eqs. (10) and (11), the RMS values of the car body vertical vibration acceleration, the secondary suspension vertical stroke, and the axle box vertical action force can be obtained by using the method of integral solution of the complex variable function [20], respectively.

$$\sigma_{\ddot{z}_2} = \sqrt{\frac{2\pi^2 A_v \Omega_c^2 v^3 \left[(a_6 a_3^2 - a_4 a_3 a_5 + a_2 a_5^2 - a_1 a_6 a_5)b_0 + (a_0 a_5^2 + a_1 a_3 a_6 - a_1 a_4 a_5)b_1 + (a_1^2 a_6 + a_0 a_3 a_5 - a_1 a_2 a_5)b_2\right]}{\left(a_0^2 a_5^3 + a_0 a_3^2 a_4 a_5 - a_0 a_3^3 a_6 - a_0 a_2 a_3 a_5^2 + 3a_0 a_1 a_3 a_5 a_6 - 2a_0 a_1 a_4 a_5^2 + a_1^3 a_6^2 - 2a_1^2 a_2 a_5 a_6 - a_1^2 a_3 a_4 a_6 + a_1^2 a_4^2 a_5 + a_1 a_2^2 a_5^2 + a_1 a_2 a_3^2 a_6 - a_1 a_2 a_3 a_4 a_5\right)}}, \quad (12)$$

$$\sigma_{f_d} = \sqrt{\frac{2\pi^2 A_v \Omega_c^2 v^3 \left[(a_0 a_5^2 - a_1 a_4 a_5 + a_1 a_3 a_6)d_0 + a_0(a_1^2 a_6 + a_0 a_3 a_5 - a_1 a_2 a_5)d_1\right]}{\left(a_0^2 a_5^3 + a_0 a_3^2 a_4 a_5 - a_0 a_3^3 a_6 - a_0 a_2 a_3 a_5^2 + 3a_0 a_1 a_3 a_5 a_6 - 2a_0 a_1 a_4 a_5^2 + a_1^3 a_6^2 - 2a_1^2 a_2 a_5 a_6 - a_1^2 a_3 a_4 a_6 + a_1^2 a_4^2 a_5 + a_1 a_2^2 a_5^2 + a_1 a_2 a_3^2 a_6 - a_1 a_2 a_3 a_4 a_5\right)}}, \quad (13)$$

$$\sigma_{F_d} = \sqrt{\frac{2\pi^2 A_v \Omega_c^2 v^3 \left[(a_1 a_3 a_4 a_6 - a_1^2 a_6^2 + 2a_1 a_2 a_5 a_6 - a_1 a_4^2 a_5 - a_2^2 a_5^2 - a_2 a_3^2 a_6 + a_2 a_3 a_4 a_5 - a_0 a_3 a_5 a_6 + a_0 a_4 a_5^2)e_0 + a_0(a_3 a_4 a_5 - a_2 a_5^2 - a_3^2 a_6 + a_1 a_5 a_6)e_1 + a_0(a_1 a_4 a_5 - a_0 a_5^2 - a_1 a_3 a_6)e_2 + a_0(a_1 a_2 a_5 - a_1^2 a_6 - a_0 a_3 a_5)e_3\right]}{-a_0\left(a_0^2 a_5^3 + a_0 a_3^2 a_4 a_5 - a_0 a_3^3 a_6 - a_0 a_2 a_3 a_5^2 + 3a_0 a_1 a_3 a_5 a_6 - 2a_0 a_1 a_4 a_5^2 + a_1^3 a_6^2 - 2a_1^2 a_2 a_5 a_6 - a_1^2 a_3 a_4 a_6 + a_1^2 a_4^2 a_5 + a_1 a_2^2 a_5^2 + a_1 a_2 a_3^2 a_6 - a_1 a_2 a_3 a_4 a_5\right)}}, \quad (14)$$

where,

$b_0 = C_1^2 C_2^2$,
$b_1 = (C_1K_2 + C_2K_1)^2 - 2C_1C_2K_1K_2$,
$b_2 = K_1^2 K_2^2$;
$d_0 = C_1^2 m_2^2$,
$d_1 = K_1^2 m_2^2$;
$e_0 = C_1^2 m_1^2 m_2^2$,
$e_1 = [C_1C_2(m_1 + m_2) + K_1 m_1 m_2]^2$
$\quad -2C_1 m_1 m_2 (K_1C_2 + K_2C_1)\,(m_1 + m_2)$,
$e_2 = [(K_1C_2 + K_2C_1)^2 - 2K_1K_2C_1C_2](m_1 + m_2)^2$
$\quad -2K_1^2 K_2 m_1 m_2 (m_1 + m_2)$,
$e_3 = K_1^2 K_2^2 (m_1 + m_2)^2$;
$a_0 = m_1 m_2$,
$a_1 = C_1 m_2 + C_2 m_1 + C_2 m_2 + m_1 m_2 v(\Omega_c + \Omega_r)$,
$a_2 = C_1C_2 + v(\Omega_c + \Omega_r)(C_1 m_2 + C_2 m_1 + C_2 m_2)$
$\quad + K_1 m_2 + K_2 m_1 + K_2 m_2 + m_1 m_2 \Omega_c \Omega_r v^2$,
$a_3 = C_1K_2 + C_2K_1 + v(\Omega_c + \Omega_r)$
$\quad \cdot (C_1C_2 + K_1 m_2 + K_2 m_1 + K_2 m_2)$
$\quad + (C_1 m_2 + C_2 m_1 + C_2 m_2)\Omega_c \Omega_r v^2$,
$a_4 = K_1K_2 + v(C_1K_2 + C_2K_1)(\Omega_c + \Omega_r)$
$\quad + (C_1C_2 + K_1 m_2 + K_2 m_1 + K_2 m_2)\Omega_c \Omega_r v^2$,
$a_5 = K_1K_2(\Omega_c + \Omega_r)(C_1K_2 + C_2K_1)\Omega_c \Omega_r v^3$,
$a_6 = K_1K_2 \Omega_c \Omega_r v^2$.

2.2 Test Verification of the Analytical Formulae

In order to verify the correctness of the RMS values analytical formulae for the vertical dynamic response of railway vehicles, a CRH2 EMU, which is widely used in China, is taken as an example to test its vibration, and the result of the vibration test and the analytical calculation is analysed. The vehicle running speed is 200 km/h, the sampling frequency is 500 Hz, and the sampling time length is 120 s. The vehicle parameter values (1/4 vehicle equivalent parameters) of the CRH2 EMU are shown in Table 1.

Table 1. *Equivalent parameters of 1/4 CRH2 EMU*

Parameters	Unit	Values
m_1	kg	1,300
m_2	kg	8,150
K_1	N/m	2,352,000
K_2	N/m	189,140
C_1	N·s/m	39,200
C_2	N·s/m	20,000

Fig. 3 shows a picture of the vehicle vibration test. Table 2 gives the comparisons results of the RMS values of the car body vertical acceleration and the secondary suspension vertical stroke obtained from the test and the analytical calculation.

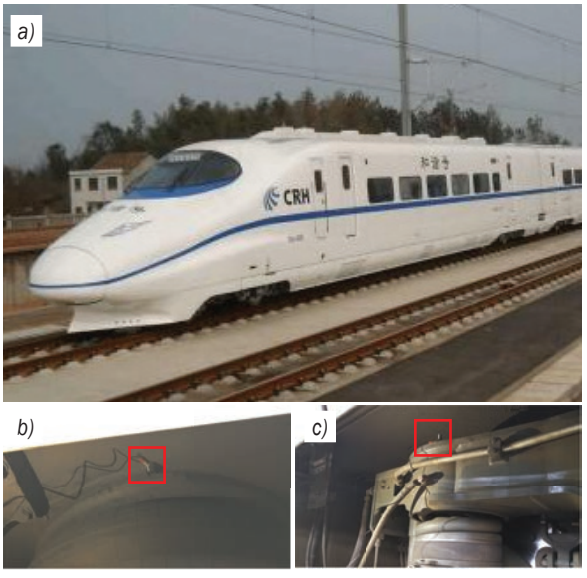

Fig. 3. *Vehicle vibration test; a) test vehicle, b) acceleration sensor installed on the upper end of the secondary suspension, and c) acceleration sensor installed on the lower end of the secondary suspension*

Table 2. *Comparisons of the test and calculation results*

RMS values	Calculation results	Test results	Absolute deviation
$\sigma_{\ddot{z}_2}$ [m/s²]	0.440	0.487	−0.047
σ_{f_d} [m]	0.013	0.012	0.001

As can be seen from Table 2, the analytical results are in good agreement with the actual vehicle test results, and the relative deviations of the RMS values of the car body vertical acceleration and the secondary suspension vertical stroke between the analytical results and the vehicle test results are only 9.65 % and 8.33 %, respectively. This shows that the RMS values analytical formulae for the vertical dynamic response of railway vehicles established are correct and reliable.

3 INFLUENCE OF SECONDARY VERTICAL SUSPENSION ON RAILWAY VEHICLE VERTICAL VIBRATION RESPONSE

In the parameter design of railway vehicles suspension system, in order to make the design result be of more practical value in engineering, the stiffness parameter is usually converted to frequency, and the damping coefficient is usually converted to the damping ratio. Therefore, according to the definition of the frequency and the damping ratio, it is known that the frequency and the damping ratio of the secondary suspension system can be written as [1]:

$$f_2 = \frac{1}{2\pi}\sqrt{\frac{K_2}{m_2}}, \quad \xi_2 = \frac{C_2}{2\sqrt{K_2 m_2}}. \tag{15}$$

According to Eq. (15), substitute it into Eqs. (12) to (14), then the influence of the secondary vertical suspension on the vertical vibration response of the train can be obtained, as shown in Figs. 4 to 6. Here, the vehicle parameter values are shown in Table 1.

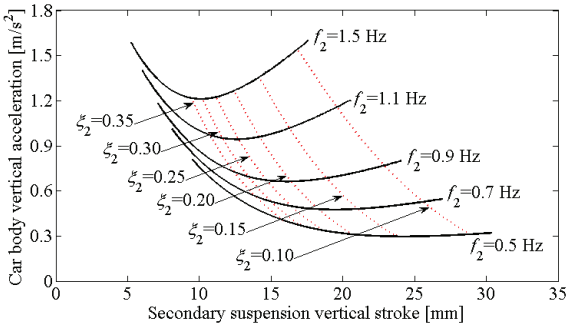

Fig. 4. *Influence of secondary vertical suspension on the car body vertical vibration acceleration and the secondary suspension vertical stroke*

As can be seen from Figs. 4 to 6, under a certain natural frequency f_2, if the damping ratio ξ_2 is too small, the secondary suspension vertical stroke will be too large, which is not conducive to the train operation. With the increase of the damping ratio ξ_2, the secondary suspension vertical stroke decreases gradually, while the car body vertical vibration acceleration and the axle box vertical action force first decrease and then increase, that is, there are minimum extreme points for both. It can be seen that, when the actual frequency value of the high-speed train is adopted, i.e., f_2 = 0.7 Hz to 1.2 Hz [4], selecting an appropriate damping ratio ξ_2 can make the car body vertical vibration acceleration, the secondary

suspension vertical stroke, and the axle box vertical action force reach a low compromise effect at the same time.

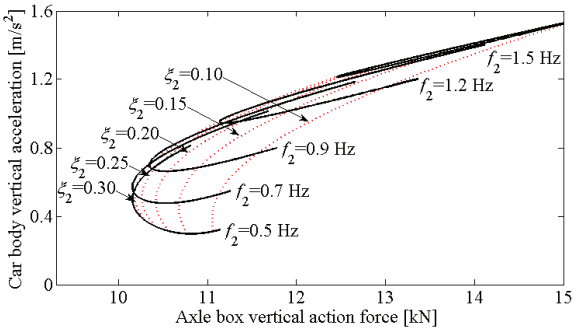

Fig. 5. *Influence of secondary vertical suspension on the car body vertical vibration acceleration and the axle box vertical action force*

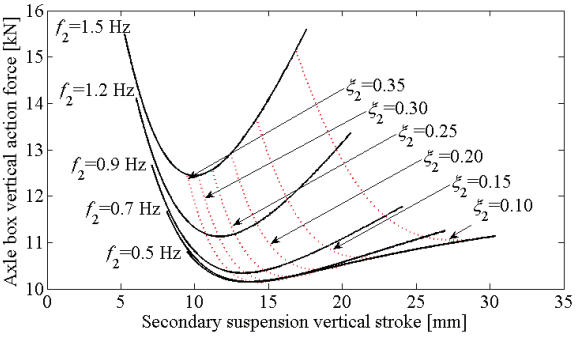

Fig. 6. *Influence of secondary vertical suspension on the secondary suspension vertical stroke and the axle box vertical action force*

4 ANALYTICAL DESIGN OF THE SECONDARY SUSPENSION DAMPING PARAMETER

It can be seen from Section 3 that the secondary vertical suspension damping parameter has a highly significant influence on the car body vertical acceleration, the secondary suspension vertical stroke, and the axle box vertical action force for railway vehicles. Therefore, in order to make the train have good running quality, when designing the secondary suspension damping parameter, the influence of these three indexes should be considered comprehensively. Based on this, a design method of the secondary suspension damping parameter for railway vehicles will be studied in this section by using the established RMS values analytical formulae.

4.1 Damping Ratio Design of the Secondary Suspension System

According to Eq. (15), substituting $C_2 = 2\xi_2\sqrt{K_2 m_2}$ into Eq. (12), solving the partial derivative of the car body vertical acceleration RMS value $\sigma_{\ddot{z}_2}$ with respect to the secondary suspension damping ratio ξ_2, and let $\left(\mathrm{d}\sigma_{\ddot{z}_2}\right)/\left(\mathrm{d}\xi_2\right)=0$, then, the analytical design equation of the optimal damping ratio for the secondary suspension system based on the minimum RMS of the car body vertical acceleration can be established, that is

$$\Lambda_{c0}\xi_2^8+\Lambda_{c1}\xi_2^7+\Lambda_{c2}\xi_2^6+\Lambda_{c3}\xi_2^5+\Lambda_{c4}\xi_2^4 +\Lambda_{c5}\xi_2^3+\Lambda_{c6}\xi_2^2+\Lambda_{c7}\xi_2+\Lambda_{c8}=0, \quad (16)$$

where, Λ_{c0} to Λ_{c8} are the coefficients of the analytical design equation expressed by vehicle parameters and vehicle speed, respectively.

Similarly, if let the partial derivative of the axle box vertical action force RMS value σ_{f_d}, Eq. (14), with respect to the secondary suspension damping ratio ξ_2 equal to zero, the analytical design equation of the optimal damping ratio for the secondary suspension system based on the minimum RMS of the axle box vertical action force can be established.

$$\Lambda_{s0}\xi_2^8+\Lambda_{s1}\xi_2^7+\Lambda_{s2}\xi_2^6+\Lambda_{s3}\xi_2^5+\Lambda_{s4}\xi_2^4 +\Lambda_{s5}\xi_2^3+\Lambda_{s6}\xi_2^2+\Lambda_{s7}\xi_2+\Lambda_{s8}=0, \quad (17)$$

where, Λ_{s0} to Λ_{s8} are the coefficients of the analytical design equation expressed by vehicle parameters and vehicle speed, respectively.

Thus, solving Eqs. (16) and (17) with respect to the positive real root of ξ_2, the optimal damping ratios of the secondary suspension system based on the minimum RMS value of the car body vertical acceleration and the axle box vertical action force can be obtained, respectively, i.e., the design values of ξ_c, and ξ_s.

Furthermore, in order to effectively avoid the probability of the suspension hitting the elastic stop block, according to the relationship between the probability distribution and the standard deviation, the relationship between the RMS value of the vertical stroke and the limit stroke $[f_d]$ of the secondary suspension system can be obtained, that is:

$$3\sigma_{f_d}=[f_d]. \quad (18)$$

Therefore, according to Eq. (13), solving Eq. (18) with respect to the positive real root of ξ_2, the minimum damping ratio of the secondary suspension system, i.e., ξ_b can be obtained based on the maximum

RMS value of the secondary suspension vertical stroke.

It can be seen that the design of the secondary suspension damping parameter is a multi-objective optimization problem. In order to improve a railway vehicle's comprehensive performance and to simplify the design process, this paper transforms the multi-objective optimization problem into a single-objective interval constraint problem by using the linear weighting method. Based on this, the optimal compromise between the minimum RMS value of the car body vertical acceleration and the minimum RMS value of the axle box vertical action force can be obtained. Also, the optimal damping ratio can effectively avoid the suspension impact limit stroke:

$$\xi_2 = \begin{cases} \xi_u = \alpha\xi_c + (1-\alpha)\xi_s, & \xi_b \le \xi_u \\ \xi_b, & \xi_b > \xi_u \end{cases}. \quad (19)$$

Here, α is a weighting factor, and its value can be determined according to the importance of each sub-target, $\alpha \in [0,1]$. Note that, in order to meet the needs of the engineering and improve the design efficiency, the golden section method [21] can be used to let $\alpha = 0.618$.

4.2 Influence of System Parameters on the Optimal Ration of the Secondary Suspension

To determine the influence of each parameter on the optimal damping ratio of the secondary suspension system, the optimal damping ratios of the secondary

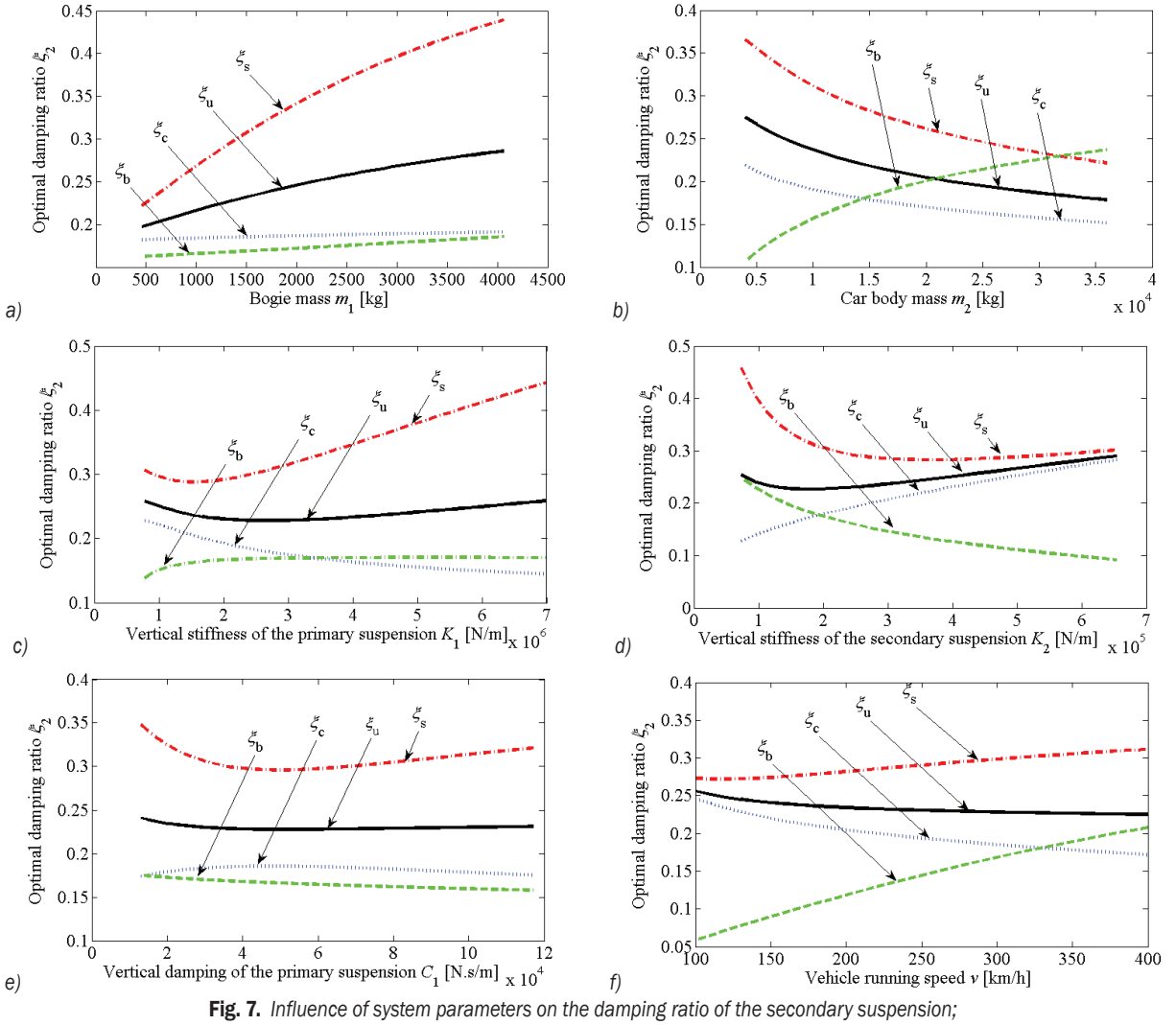

Fig. 7. *Influence of system parameters on the damping ratio of the secondary suspension; a) bogie mass m_1, b) car body mass m_2, c) vertical stiffness of the primary suspension K_1, d) vertical stiffness of the secondary suspension K_2, e) vertical damping of the primary suspension C_1, and f) vehicle running speed v*

suspension system under each parameter are analysed with the example of the railway vehicle shown in Table 1. The curves of the secondary suspension damping ratio with the variation of the system parameters are obtained, as shown in Fig. 7. Here, the weighting factor $\alpha = 0.618$, the vehicle running speed $v = 300$ km/h, and the limit stroke $[f_d] = 60$ mm.

As can be seen from Fig. 7, the optimal damping ratio ξ_c: almost unchanged with the increase of m_1; decreases with the increase of m_2; decreases with the increase of K_1; increases with the increase of K_2; increases first and then decreases with the increase of C_1, but the overall change is not obvious; decreases with the increase of v. The optimal damping ratio ξ_s: increases with the increase of m_1; decreases with the increase of m_2; decreases first and then increases with the increase of K_1; decreases first and then almost unchanged with the increase of K_2; decreases first and then increases with the increase of C_1; increases gradually with the increase of v, but the overall change is not obvious. The minimum damping ratio ξ_b: increases with the increase of m_1; increases with the increase of m_2; first increases with the increase of K_1 and then remains unchanged; decreases with the increase of K_2; almost unchanged with the increase of C_1; increases with the increase of v. The compromised damping ratio ξ_u: increases with the increase of m_1; decreases with the increase of m_2; decreases first and then increases with the increase of K_1; decreases first and then increases with the increase of K_2; almost remains unchanged with the increase of C_1; decreases with the increase of v, but the overall change is small. It can be seen that, among the system parameters, the car body mass m_2 and bogie frame mass m_1 have the greatest influence on the optimal damping ratio of the secondary suspension system, followed by the secondary suspension vertical stiffness K_2, the primary suspension vertical stiffness K_1, the vehicle running speed v, and the primary suspension vertical damping C_1. Therefore, when choosing the damping parameter of the secondary suspension system for railway vehicles, the influence of vehicle running speed should be taken into account in addition to the parameters of the vehicle itself, in which this phenomenon has not been found in previous studies.

4.3 Engineering Design Example

Taking the train shown in Table 1 as an example, the damping ratio of its secondary vertical suspension is designed by using the established analytical design method. The design results of the damping ratio at different vehicle running speeds as shown in Table 3. Here, the secondary suspension vertical limit stroke $[f_d] = 60$ mm.

Table 3. *Design results of the damping ratio*

Damping ratio	Design value			
	$v = 200$ km/h	$v = 250$ km/h	$v = 300$ km/h	$v = 350$ km/h
ξ_c	0.206	0.195	0.187	0.180
ξ_s	0.307	0.321	0.334	0.345
ξ_b	0.107	0.131	0.154	0.175
ξ_u	0.244	0.243	0.243	0.243
ξ_2	0.244	0.243	0.243	0.243

As can be seen from Table 3, the design values of the secondary suspension damping ratio corresponding to the CRH2's operation speed range (200 km/h to 350 km/h) are all around 0.24, which is basically the same. Therefore, in order to take into account the running quality of the vehicle at different running speeds, the damping ratio of the secondary suspension system can be chosen as $\xi_2 = 0.24$. It can be seen that the design result is close to the original vehicle design value 0.25; moreover, it is within the feasible design range (0.2 to 0.4) of the damping ratio of the secondary vertical suspension system given in literature [1], which indicates that the design value of the damping ratio obtained by this method is reliable.

5 CONCLUSIONS

1. According to the 1/4 railway vehicle model, using the Germany track vertical irregularity power spectral density as the input excitation of the vehicle system, the RMS values analytical formulae of the car body vertical acceleration, the secondary suspension vertical stroke, and the axle box vertical action force are derived, and the correctness of the analytical formulae is verified by the real vehicle test. The analytical formulae can more reasonably and accurately estimate the dynamic characteristics of the actual vehicle running on the track.
2. According to the analytical calculation formulae derived, an analytical design method of the optimal damping ratio for the secondary suspension system is proposed based on the multi-objective programming and single-objective interval constraint analysis, which can be used to find the best trade-off for conflicting performance indices such as ride comfort, running smoothness and running safety.
3. The influences of the system parameters on the optimal damping ratio are analysed. It can be seen

that, when choosing the secondary suspension damping parameter, the influence of the vehicle running speed should be taken into account in addition to the parameters of the vehicle itself. This study can provide an effective theoretical reference for the selection of the initial design value of the secondary suspension damping parameter for railway vehicles.

Note that this paper has deduced the analytical formulae of the vertical dynamic responses for railway vehicles and proposed an analytical design method of the damping parameter for its secondary suspension system. Although the research is based on the simplified model of the railway vehicle, it can help to have a qualitative understanding of the phenomena referring to suspension dynamics and enable designers to make reasonable engineering choices quickly and effectively. Moreover, it can greatly simplify the inconvenience of analysis and solution caused by many unknown parameters in the early stage of design.

6 ACKNOWLEDGEMENTS

This work is supported by the Natural Science Foundation of Shandong Province under Grant ZR2021QE082 and ZR2020ME127.

7 REFERENCES

[1] Yang, G.Z., Wang, F.T. (2002). *Locomotive Vehicle Hydraulic Shock Absorber*. China Railway Press, Beijing.

[2] Eichberger, A., Hofmann, G. (2007). TMPT: multi-body package SIMPACK. *Vehicle System Dynamics*, vol. 45, Sup. 1, p. 207-216, **DOI:10.1080/00423110701803385**.

[3] Eom, B.G., Lee, H.S. (2010). Assessment of running safety of railway vehicles using multibody dynamics. *International Journal of Precision Engineering and Manufacturing*, vol. 11, p. 315-320, **DOI:10.1007/s12541-010-0036-x**.

[4] Verros, G., Goudas, H., Natsiavas, S., Hache, M. (2000). Dynamics of large scale vehicle models using ADAMS/FLEX. *International ADAMS User Conference*, p. 1-11.

[5] Evans, J., Berg, M. (2009). Challenges in simulation of rail vehicle dynamics. *Vehicle System Dynamics*, vol. 47, no. 8, p. 1023-1048, **DOI:10.1080/00423110903071674**.

[6] Dukkipati, R.V., Amyot, J.R. (1988). *Computer-Aided Simulation in Railway Dynamics*. Marcel Dekker, Inc., New York.

[7] Zhu, L. F., Zhu. J. G., Tong, W. M., Han, X. Y. (2017). Analytical method of no-load iron losses of axial flux amorphous alloy permanent magnet motor. *Proceedings of the CSEE*, vol. 37, no. 3, p. 923-930, **DOI:10.13334/j.0258-8013.pcsee.160027**.

[8] Gobbi, M., Mastinu, G. (2001). Analytical description and optimization of the dynamic behaviour of passively suspended road vehicles. *Journal of Sound and Vibration*, vol. 245, no. 3, p. 457-481, **DOI:10.1006/jsvi.2001.3591**.

[9] Gong, D., Zhou, J. S., Sun, W. J., Shen, G. (2014). Modal matching between suspended equipment and car body of a high-speed railway vehicle and in-situ experiment. *Journal of the China Railway Society*, vol. 36, no. 10, p. 13-20, **DOI:10.3969/j.issn.1001-8360.2014.10.003**.

[10] Zhou, C.C., Yu, Y.W., Zhao, L.L. (2016). Analytical calculation of the optimal damping ratio of primary vertical suspension system for high-speed train. *Journal of Railway Science and Engineering*, vol. 13, no. 10, p. 1891-1898, **DOI:10.3969/j.issn.1672-7029.2016.10.003**.

[11] Mastinu, G.R.M., Gobbi, M., Pace, G.D. (2001). Analytical formulae for the design of a railway vehicle suspension system. *Proceedings of the Institution of Mechanical Engineers Part C Journal of Mechanical Engineering Science*, vol. 215, no. 6, p. 683-698, **DOI:10.1243/0954406011524054**.

[12] Zhou, C.C., Yu, Y.W., Zhao, L.L. (2016). Analytical formulae of secondary vertical suspension system design for high-speed train. *Journal of Mechanical Engineering*, vol. 52, no. 19, p. 53-60, **DOI:10.3901/JME.2016.19.053**. (in Chinese)

[13] Garg, V.K., Dukkipati, R.V. (1984). *Dynamics of Railway Vehicle System*. Academic Press, Toronto, **DOI:10.1016/B978-0-12-275950-5.X5001-9**.

[14] Mastinu, G., Gobbi, M., Miano, C. (2006). Optimal *Design of Complex Mechanical Systems*. Springer, Berlin, **DOI:10.1007/978-3-540-34355-4**.

[15] Zhai, W.M., Sun, X. (1994). A detailed model for investigating vertical interaction between railway vehicle and track. *Vehicle System Dynamics*, vol. 23, no. Supl. 1, p. 603-615, **DOI:10.1080/00423119308969544**.

[16] Zhai, W.M. (1997). A study of vertical coupling dynamics of high speed train and track systems. *Journal of the China Railway Society*, vol. 19, no. 4, p. 16-21, **DOI:CNKI:SUN:TDXB.0.1997-04-002**.

[17] Zhao, Y., Huang, X. (2014). Using the delayed feedback to control the vibration of semi-active suspension system for high-speed train. *IEEE International Conference on Mechatronics & Automation*, p. 1376-1381, **DOI:10.1109/ICMA.2014.6885900**.

[18] Nguyen, S.D., Choi., S.B., Nguyen, Q.H. (2018). A new fuzzy-disturbance observer-enhanced sliding controller for vibration control of a train-car suspension with magneto-rheological dampers. *Mechanical Systems and Signal Processing*, vol. 105, p. 447-466, **DOI:10.1016/j.ymssp.2017.12.019**.

[19] Zhai, W.M. (2015). *Vehicle-Track Coupled Dynamics*, 4th ed. Science Press, Beijing.

[20] Zhong, Y.Q. (2004). *Theory of Functions of a Complex Variable*, 3rd ed., Higher Education Press, Beijing.

[21] Yu, Y.W., Zhou, C.C., Zhao, L.L. (2018). Analytical research of yaw damper damping matching for high-speed train. *Journal of Mechanical Engineering*, vol. 54, no. 2, p. 159-168, **DOI:10.3901/JME.2018.02.159**.

List of reviewers who reviewed manuscripts in 2022

Husam Jawad Abdulsamad, Iraq
Abuzer Açıkgöz, Turkey
Mike Adams, UK
Emre İsa Albak, Turkey
Irina Stefanova Aleksandrova, Bulgaria
Karim Aliakbari, Iran
Wael Al-Kouz, Jordan
Ahmed Ramadhan Al-Obaidi, Iraq
Miha Ambrož, Slovenia
Jorge Enrique Araque Isidro, Italy
Meysam Atashafrooz, Iran
Gokhan Aydin, Turkey

Suresha B., India
Matej Babič, Slovenia
Sebastian Baloš, Serbia
Milan S. Banić, Serbia
Jorge L.V. Barbosa, Brazil
Sinan Basaran, Turkey
Aravind Baskar, US
Michał Batsch, Poland
Branko Bauer, Croatia
Marko Bek, Slovenia
Aleš Belšak, Slovenia
Károly Beneda, Hungary
Zoran Bergant, Slovenia
Tomaž Berlec, Slovenia
Miha Bobic, Slovenia
Miha Boltežar, Slovenia
sampath Boopathi, India
Zahra Bouramdane, Morocco
Tomaž Brajlih, Slovenia
Miha Brojan, Slovenia

Hrvoje Cajner, Croatia
Betül Gülçimen Çakan, Turkey
Michele Cali, Italy
Gürel Çam, Turkey
Song Cen, China
Ferdinand Cerbe, Germany
Shankar Chakraborty, India
Ali J. Chamkha, Saudi Arabia
G. Chandrasekar, India
Chuanhai Chen, China
Jipeng Chen, China
Zhen Chen, China
Gang Cheng, China
Peng Cheng, US
Anurag Choudhary, India
Yu-Ming Chu, China
Oktay Çiçek, Turkey
Marco Cirelli, Italy
Daniele Contini, Italy
Martin Česnik, Slovenia
Gregor Čepon, Slovenia
Martin Česnik, Slovenia
Ante Čikić, Croatia
Mirko Čudina, Slovenia

Piotr Danielczyk, Poland
Omar Dávalos, Mexico
Krisztián Deák, Hungary
Marco Dell'Isola, Italy
Murat Demiral, Kuwait
Cihan Demircan, Turkey
Anderson dePaiva, Brasil
Hamed Aghajani Derazkola, Spain
Janez Diaci, Slovenia
Franz Dietrich, Germany
Mehmet Direk, Turkey
Ján Dižo, Slovakia
Oana Dodun, Romania
Radomir, Đokić, Serbia
Grzegorz Domek, Poland
David B. Dooner, Puerto Rico
Mateja Dovjak, Slovenia
L. Canan Dülger, Turkey
Paweł Dunaj, Poland
Mihai Dupac, UK
Radomir Đokić, Serbia

Andrea Ehrmann, Germany
Majid Elyasi, Iran
Andreas Endruweit, UK

Imre Felde, Hungary
Cuneyt Fetvaci, Turkey
Bogdan Filipič, Slovenia
José Dalfré Filho, Brasil
Grzegorz Filo, Poland
Snježana Firšt Rogale, Croatia
Rastko Fišer, Ljubljana
Jürgen Fleischer, Germany
Dávid Földes, Hungary
Regiane Fortes-Patella, France

Andrés García, Argentina
Juan Carlos García, Mexico
Mehran Ghasempour-Mouziraji, Iran
Gilbert-Rainer Gillich, Romania
Adam Glowacz, Poland
F. Gómez-Silva, Spain
Przemysław Golewski, Poland
Christoph Greb, Germany
Damir Grguraš, Slovenia
Laurent Guillier, France
Ibrahim Gunes, Turkey
Kai Guo, China

Jiří Hajek, Czech Republic
Ali Hajnayeb, Canada
R Halicioglu, Turkey
Patricia Habib Hallak, Brazil
Ouafae Hamdoun, Morocco
Mingxing Han, China
Boštjan Harl, Slovenia
Ngo Le Huy Hien, OK
Sergej Hloch, Slovakia
Matija Hoić, Croatia
Richárd Horváth, Hungary
Matjaz Hriberšek, Slovenia
Wen-Chen Huang, Taiwan
Yongxian Huang, China
Anica Hursa Šajatović, Croatia

The Editorial would like to thank all the reviewers in participating in reviewing process.
We appreciate the time and effort and greatly value the assistance as a manuscript reviewer for Strojniški vestnik – Journal of Mechanical Engineering.

Vsebina

Strojniški vestnik - Journal of Mechanical Engineering
letnik 69, (2023), številka 1-2
Ljubljana, januar-februar 2023
ISSN 0039-2480

Izhaja mesečno

Razširjeni povzetki (extended abstracts)

Strojniški vestnik - Journal of Mechanical Engineering 69(2023)1-2, SI 3

Prejeto v recenzijo: 2022-09-26
Prejeto popravljeno: 2022-12-13
Odobreno za objavo: 2023-01-04

Študija dinamičnih lastnosti vrtanja sidrnih vrvi z nastavkom v peščene sedimente spodnjih vrtin v mehki zemljini

Kuidong Gao[1,2] – Jihai Liu[1,2,*] – Qingliang Zeng[3] – Jingyi Cheng[4] – Liqing Sun[1] – Lisong Lin[1,2]

1 Kolidž za strojništvo in elektrotehniko, Znanstveno-tehniška univerza v Shandongu, Kitajska
2 Laboratorij province Shandong za geotehniko, Znanstveno-tehniška univerza v Shandongu, Kitajska
3 Šola za informatiko in tehniko, Normalka v Shandongu, Kitajska
4 Rudarska šola, Kitajska rudarska in tehniška univerza, Kitajska

Pri obdelavi dvignjenih tal se v fazi priprave sidrnih lukenj v spodnji vrtini pogosto kopičijo peščeni sedimenti, ki lahko povzročijo velike težave pri vgradnji sidrnih vrvi. Na podlagi te ugotovitve je bila predlagana nova metoda za vgradnjo sidrnih vrvi z uporabo vrtalnega nastavka pred vrvjo, ki pomaga pri vrtanju. Vpliv vrtalnega nastavka, parametrov gibanja in razmer v vrtini na zmogljivost vrtanja sidrnih vrvi je bil preučen na posebnem preizkuševališču. Proces vrtanja vrvi z nastavkom je bil simuliran po metodi diskretnih elementov in dinamike več teles (DEM–MBD). Analizirane so bile lastnosti dinamike pri vrtanju vrvi z nastavkom v peščeni sediment spodnje vrtine. Glavne ugotovitve:

1. Globina vrtanja v smeri urnega kazalca s sidrno vrvjo brez vrtalnega nastavka je znašala samo 0,25 m. Ko je bil pred sidrno vrvjo nameščen vrtalni nastavek, se je globina vrtanja povečala na 0,6 m. Vgradnja nastavka pred sidrno vrvjo lahko znatno zmanjša upor in zavorni moment pri vrtanju. Vrtanje z nastavkom v smeri urnega kazalca pri vgrajevanju vrvi daje boljše rezultate kot vrtanje v smeri nasproti vrtenju urnega kazalca. Upor in zavorni moment pri vrtanju z vrvjo z nastavkom sta obratno sorazmerna vrtilni frekvenci.
2. Upor in zavorni moment pri vrtanju z vrvjo z nastavkom sta bila največja pri vrtanju v namočena zrna, temu je sledilo vrtanje v suha zrna, najmanjši pa je bil upor pri vrtanju v vlažna zrna. Pesek mora biti torej med vgradnjo sidrne vrvi z vrtalnim nastavkom kar se da vlažen, čezmerni vodi v vrtini pa se je treba izogibati. Ob porušitvi oz. ponovni vzpostavitvi stabilnosti strukture peščenih zrn med vrtanjem lahko prihaja do velikih sprememb upora in zavornega momenta. Pri vrtanju vrvi z nastavkom v namočena zrna z vrtilno frekvenco 300/min sta upor in zavorni moment na globini 0,5 m znašala 446 % in 400 % ustreznih vrednosti na globini 0,4 m.
3. Upor in zavorni moment pri vrtanju z nastavkom sta obratno sorazmerna s premerom peščenih delcev. Najboljši učinek eksperimentalnega vrtanja je bil dosežen pri premeru zrn peska 10 do 13 mm. Vrtanje v pesek enakomerne zrnavosti je povezano z manjšim uporom oz. zavornim momentom kot vrtanje v pesek neenakomerne zrnavosti. Vpliv oblike delcev na vrtanje s sidrno vrvjo z nastavkom se zmanjšuje s povečevanjem vrtilne frekvence. Če so zrna peska majhna in je njihova oblika neenakomerna, je treba za ohranitev učinkovitosti vgradnje dodatno povečati vrtilno frekvenco sidrne vrvi z nastavkom.

Raziskava ponuja rešitev za težave pri vgradnji sidrnih vrvi, ki se pojavljajo zaradi zbiranja peska v vrtinah. Dodatni pripomočki za vgradnjo sidrnih vrvi lahko odpravijo težave s pomanjkljivo učinkovitostjo in visokimi stroški ročne vgradnje sidrnih vrvi. Simulacija DEM–MBD je razkrila vpliv sidrne vrvi z vrtalnim nastavkom na gibanje diskretnih zrn. Dokazano je bilo, da se stabilna struktura peska med procesom vrtanja z nastavkom nenehno ruši in ponovno vzpostavlja. Na vgradnjo sidrnih vrvi z vrtalnim nastavkom v vrtine s prisotnostjo peska torej ugodno vplivajo: vrtenje sidrne vrvi z nastavkom v smeri urnega kazalca, nizka hitrost podajanja, visoka vrtilna frekvenca, vlažnost zrn peska, premer delcev 10 do 13 mm in pravilna oblika zrn.

Ključne besede: vrtalni nastavek, sidrna vrv, vrtanje v pesek, dinamične lastnosti, DEM–MBD, diskretna zrna

*Naslov avtorja za dopisovanje: Kolidž za strojništvo in elektrotehniko, Znanstveno-tehniška univerza v Shandongu, Kitajska, ljhsdust@163.com

Strojniški vestnik - Journal of Mechanical Engineering 69(2023)1-2, SI 4

Prejeto v recenzijo: 2022-10-27
Prejeto popravljeno: 2022-12-30
Odobreno za objavo: 2023-01-09

Analiza dinamičnih lastnosti sistema zobnik–rotor–ležaj z zunanjim vzbujanjem

Risu Na – Kaifa Jia* – Shujing Miao – Weiguo Zhang – Quan Zhang
[1] Kolidž za strojništvo, Tehniška univerza Notranje Mongolije, Kitajska

Določitev dinamičnega odgovora rotorja v granulatorju z matričnim prstanom pod vplivom zunanjih sil, podpornih sil ter sil pri ubiranju zobnikov je kompleksen in težaven problem. V pričujoči študiji sta bili za razrešitev omenjenega problema uporabljeni metoda končnih elementov in teorija ekstrudiranja za razvoj dinamičnega modela votlega obešenega rotorja z vzbujanjem zunanjih sil. Od zunanjih obremenitvenih dejavnikov so bili upoštevani sila ubiranja vijačnega zobnika s časovno spremenljivo togostjo in blaženjem, vpliv nelinearne sile krogličnega ležaja z globokim kanalom ter vpliv zunanjega vzbujanja na podlagi predlaganega eksponentnega modela.

Rezultati vključujejo diagrame odgovora v časovni in frekvenčni domeni ter fazne, Poincaréjeve in bifurkacijske diagrame. V članku je opisana eksperimentalna verifikacija modela na realnem granulatorju z matričnim prstanom, rezultati eksperimentov pa so bili primerjani s teoretičnimi rezultati za potrditev veljavnosti in točnosti teoretičnega modela. Hkrati je bila preverjena tudi točnost in uporabnost modela mehanike ekstrudiranja, modela ubiranja zobnikov, modela ležajne podpore in modela večkratne sklopitve vzbujanja rotorskega sistema. Rezultati so v pomoč pri reševanju dinamike kompleksne konstrukcije in vzbujanega rotorja. Končno je bila v skladu s teoretičnim modelom opravljena še analiza dinamičnega odgovora z bifurkacijskimi diagrami za močno nelinearne dejavnike, kot so dolžina ležajne podpore, ekscentričnost valjev in variabilnost zračnosti ležajev. Opredeljeni so bili tudi vplivi njihovih parametrov na zmogljivost rotorja.

Rezultate študije je mogoče strniti v tri glavne točke:

1. Povečanje dolžine ležajne podpore koristi pri optimizaciji dinamičnega odgovora sistema. Če je dolžina ležajne podpore premajhna, postane odgovor kompliciran in lahko se pojavi kaotično gibanje. Če se ležajna dolžina poveča za 120 mm, se amplituda odmika v smereh x in y zmanjša za 0,35 mm oz. 0,37 mm, kazalniki dinamične zmogljivosti sistema pa se izboljšajo. Premišljena konstrukcija rotorja in izbira dolžine ležajne podpore sta zato zelo pomembni za optimizacijo odgovora in izboljšanje stabilnosti sistema.
2. Zmanjšanje ekscentričnosti matričnega prstana pozitivno vpliva na optimizacijo odgovora sistema. Primerjava krivulj v frekvenčni domeni, faznih diagramov in Poincaréjevih diagramov je pokazala, da se z zmanjšanjem ekscentričnosti potisnega valja zmanjša tudi amplituda odgovora sistema, pojav kaotičnosti se zmanjša in kazalniki dinamične zmogljivosti se izboljšajo. Ekscentričnost je glavni dejavnik, ki vpliva na učinkovitost in kakovost granulacije. Izbira prave ekscentričnosti valjev je zato pomembna za optimizacijo odgovora in izboljšanje produktivnosti sistema.
3. Zmanjšanje zračnosti ležaja koristi pri optimizaciji dinamičnega odgovora sistema. Primerjava krivulj v frekvenčni domeni, faznih diagramov in Poincaréjevih diagramov je pokazala, da se z zmanjšanjem zračnosti ležaja zmanjša amplituda odgovora sistema, pojav kaotičnosti se zmanjša in izboljšajo se kazalniki dinamične zmogljivosti. Zračnost ležaja je glavni dejavnik, ki vpliva na stabilnost rotorskega sistema.

Redno vzdrževanje in menjava ležajev sta zato pomembna za optimizacijo odgovora in izboljšanje zanesljivosti sistema. Metoda tako ne razrešuje le problema težavnega izračuna odgovora rotorskega sistema granulatorja z matričnim prstanom, ampak tudi podaja smernice za analizo dinamike rotorjev neenakomerne oblike in rotorjev z večkratno sklopitvijo vzbujanj. Računski model obremenitev pri ekstrudiranju je osnova teoretičnih optimizacij pri projektiranju strojev za izdelavo peletov ter je primeren za usmerjanje optimizacije dinamičnega odgovora.

Ključne besede: dinamika rotorja, zunanje vzbujanje, metoda končnih elementov, ležaj, zobnik, sila pri ekstrudiranju

*Naslov avtorja za dopisovanje: Kolidž za strojništvo, Tehniška univerza Notranje Mongolije, Kitajska, 1642523516@qq.com

Strojniški vestnik - Journal of Mechanical Engineering 69(2023)1-2, SI 5

Prejeto v recenzijo: 2022-08-17
Prejeto popravljeno: 2022-12-22
Odobreno za objavo: 2023-01-03

Modeli tipa Angstrom-Prescott za napovedovanje sončnega obsevanja na različnih lokacijah v Zimbabveju

Cedrick Iradukunda[1] – Kudzanayi Chiteka[2,*]

[1] Oddelek za industrijski inženiring in mehatroniko, Univerza v Zimbabveju, Zimbabve
[2] Fakulteta za tehniko in okolje, Državna univerza v Gwandi, Zimbabve

Glavni cilj pričujoče študije je razvoj splošnega modela tipa Angstrom-Prescott za napovedovanje sončnega obsevanja v Zimbabveju.

Podatki o sončnem obsevanju in trajanju osončenosti iz 29 postaj v Zimbabveju so bili uporabljeni za generiranje mesečnih in letnih koeficientov tipa Angstrom-Prescott a in b, ki se nanašajo na lokacijo. Koeficienti so bili določeni na podlagi linearne korelacije med indeksom jasnosti in trajanjem osončenosti. Razvit je bil model za napovedovanje sončnega obsevanja, prilagojen iz satelitskih podatkov ter novejših in zgodovinskih podatkov o izmerjenem sončnem obsevanju iz zemeljskih postaj v Zimbabveju.

Uporabljeni podatkovni seti obsegajo tri različne vire podatkov, vključno z meritvami iz 29 zemeljskih meteoroloških postaj v Zimbabveju, meritvami iz opazovalne postaje Univerze v Zimbabveju in satelitskimi podatki o sončnem obsevanju, pridobljenimi na spletnem mestu NASA POWER Data Access (https://power.larc.nasa.gov/data-access-viewer). Satelitski podatki so bili korigirani z ustreznim faktorjem za pridobitev ustreznih podatkov na zemlji. Zemeljski podatki so bili uporabljeni za kalibracijo satelitskih meritev in s tem za združljivost podatkovnih setov. Opravljeno je bilo tudi preverjanje kakovosti podatkov za zmanjšanje napak v modelih.

Izračunana sta bila mesečna in letna regresijska koeficienta a in b. Mesečna koeficienta sta bila uporabljena skupaj z meritvami trajanja osončenosti S, mesečnega zunajzemeljskega sončnega sevanja H_0 in vrednostjo najdaljšega trajanja osončenosti S_o iz vsake postaje za oceno mesečnega globalnega sončnega obsevanja H_e po modelih tipa Angstrom-Prescott.

Vrednost R^2 za ujemanje med satelitskimi in zemeljskimi meritvami obsevanja je znašala 0,6738. Korelacija med indeksom jasnosti in trajanjem osončenosti na večini postaj je bila razmeroma visoka z determinacijskim koeficientom R^2 v višini 0,9030. Vrednost regresijskega koeficienta a po Angstrom-Prescottu, generiranega iz podatkov iz vsake postaje, je znašala med 0,2252 in 0,3976, medtem ko je vrednost regresijskega koeficienta b znašala med 0,3218 in 0,6256. Ocenjene in izmerjene vrednosti globalnega sončnega obsevanja iz posameznih postaj H_e in H_m so bile primerjane na podlagi srednje absolutne odstotne napake (MAPE), korena srednje kvadratne napake (RMSE), srednje absolutne napake (MAE) in relativne standardne napake (RSE). Vrednosti MAE za modele so znašale od 0,5438 MJ/m^2 do 2,2845 MJ/m^2. Vrednosti MAPE so znašale od 2,5642 % do 10,334 %. Vrednosti RSE so znašale od 0,0346 % do 0,1537 %, medtem ko so vrednosti RMSE za modele znašale od 0,7360 MJ/m^2 do 2,9454 MJ/m^2. Rezultati so glede na statistične kazalce znotraj priporočenega območja za modele napovedovanja sončnega obsevanja iz podobnih študij.

Rezultati študije so omejeni na izbrane lokacije. To pomeni, da koeficientov in ostalih rezultatov ni mogoče uporabiti za ocenjevanje sončnega obsevanja na drugih območjih z drugačnimi podnebnimi razmerami.

Razviti modeli lahko zagotovijo ocene sončnega obsevanja, ki trenutno niso na voljo iz meteoroloških postaj v Zimbabveju ter tako zapolnjujejo vrzel v podatkih o sončnem obsevanju.

Ključne besede: empirični koeficienti, modeli Angstrom-Prescott, sončno obsevanje, trajanje osončenosti

*Naslov avtorja za dopisovanje: Fakulteta za tehniko in okolje, Državna univerza v Gwandi, Zimbabve, tavakudzira@gmail.com

Strojniški vestnik - Journal of Mechanical Engineering 69(2023)1-2, SI 6

Prejeto v recenzijo: 2022-10-15
Prejeto popravljeno: 2022-12-21
Odobreno za objavo: 2023-01-11

Vpliv vzorca dezena, ki posnema blazinico na mačji šapi, na vibracije in hrupnost pnevmatik

Guolin Wang[1] – Kexin Zhu[1] – Lei Wang[1] – Jian Yang[1,*] – Lin Bo[2]
[1] Univerza Jiangsu, Šola za avtomobilsko in prometno tehniko, Kitajska
[2] KENDA Industrial Co., Ltd, Kitajska

Koncept bionike se uporablja v različnih industrijah in predstavlja pomemben vir tehnoloških inovacij. Struktura dezena pnevmatike neposredno vpliva na sile, s katerimi cesta deluje na pnevmatiko med kotaljenjem in s tem posredno na vibracije in na hrup. Članek preučuje korelacije med karakterističnimi parametri stika z voziščem in hrupnostjo pnevmatike ter mehanizmom blaženja vibracij in utišanja mačje hoje s ciljem oblikovanja malohrupnega dezena.

Analizirane so dinamične lastnosti stika s podlago in mehanizem zmanjšanja vibracij pri blazinicah na šapi domače mačke. Na podlagi tega je izdelana bionična modifikacija dezena pnevmatike za zmanjšanje hrupnosti. Imitacija blazinice mačje šape za blaženje udarcev je bila realizirana z umestitvijo zamaknjenega vzorca v osrednji del pnevmatike. To je bilo izhodišče za preučitev mehanizma zmanjševanja hrupnosti pri pnevmatikah z omenjenim vzorcem.

Kot raziskovalni objekt za preučitev zmanjševanja nizkofrekvenčnih vibracij in hrupnosti je bila uporabljena avtomobilska pnevmatika (205/55 R16). Analizirane so dinamične lastnosti stika s podlago in mehanizem blaženja vibracij blazinice pri mačji šapi. Izkazalo se je, da so za blaženje udarcev ter za zmanjšanje vibracij in hrupnosti zaslužne predvsem deformacijske lastnosti blazinic med hojo. Stik pnevmatike z voziščem je bil za analizo vpliva na hrup razdeljen na pet območij, katerih lastnosti so bile analizirane s preizkusi na desetih pnevmatikah. Odvisnost hrupnosti pnevmatike od osmih najpomembnejših parametrov stika z voziščem je bila določena s Pearsonovo korelacijsko analizo. Opravljena je bila tudi multipla linearna regresijska analiza lastnosti osmih območij stika. Zmnožek koeficienta korelacije in povprečne vrednosti lastnosti območja stika z voziščem je pokazal, da k hrupnosti pnevmatike najbolj prispeva osrednji del dezena. Deformacijske lastnosti, ki posnemajo blazinico mačje šape, so bile realizirane s postavitvijo zamaknjenega vzorca na sredino pnevmatike. Lastnosti zmanjšanja vibracij bionične pnevmatike so bile analizirane po metodi končnih elementov.

Rezultati in ugotovitve:

1. Mehanski preizkusi blazinicah na šapah domače mačke so pokazali, da lastnosti stika blazinic s tlemi med hojo poglavitno prispevajo k učinku zmanjšanja vibracij in hrupnosti med hojo.
2. Analiza parametrov stika desetih pnevmatik s podlago je pokazala, da na hrupnost pnevmatik vpliva predvsem osrednji del dezena. Učinek blaženja vibracij blazinic mačje šape med hojo je bil tako dosežen z umestitvijo zamaknjenega vzorca na sredino pnevmatike.
3. Bionična pnevmatika lahko znatno zmanjša amplitudo in nihanja radialne vzbujalne sile tal ter tako učinkovito zmanjša hrup zaradi vibracij v nizkofrekvenčnem območju za zmanjšanje vibracij in hrupnosti pnevmatike.

Število vzorcev, ki so bili uporabljeni v statistični analizi, je omejeno zaradi dveh razlogov: (1) omejitve preizkusnih pogojev; (2) podatki o preizkusih zmogljivosti pnevmatik v članku izhajajo iz poročila, ki ga je izdala specializirana ustanova po strogih preizkusih pnevmatik v skladu s predpisi EU. Vzorec dezena na raziskovalnem objektu tega članka ustreza značilnemu vzorcu in je primeren za analizo vpliva vzorcev na deformacije dezena v območju stika. V prihodnjih raziskavah bo povečano število vzorcev in vključenih bo več pnevmatik z drugačnimi dezeni za določitev objektivnejših pravil in smernic pri oblikovanju visokozmogljivih pnevmatik.

Članek vzpostavlja numerično povezavo med lastnostmi stika in hrupnostjo pnevmatik ter analizira prispevek različnih območij na dezenu k hrupnosti pnevmatike. Poleg tega prenaša biofunkcijske lastnosti blazinic šap domače mačke v raziskave dezenov pnevmatik in predstavlja predlog metode za bionično zasnovo strukture dezena s ciljem zmanjšanja vibracij in hrupnosti pnevmatik. S tem ima svojo uporabnost na področju raziskav in razvoja malohrupnih pnevmatik.

Ključne besede: bionika, mehanizem blaženja vibracij, vibracije in hrup, vzorec dezena, konstrukcijska zasnova, analiza po metodi končnih elementov

*Naslov avtorja za dopisovanje: Univerza Jiangsu, Šola za avtomobilsko in prometno tehniko, Zhenjiang, Kitajska, yangjian@ujs.edu.cn

Strojniški vestnik - Journal of Mechanical Engineering 69(2023)1-2, SI 7

Prejeto v recenzijo: 2022-06-16
Prejeto popravljeno: 2022-10-10
Odobreno za objavo: 2022-11-03

Uporaba nevronske mreže pri modularni ureditvi vnaprej določenih časovnih normativov

Emmanuel Basitere[1] – Ilesanmi Daniyan[1,*] – Khumbulani Mpofu[1] – Adefemi Adeodu[2]

[1] Tehniška univerza Tshwane, Oddelek za industrijski inženiring, Južna Afrika
[2]Univerza Južne Afrike, Oddelek za strojništvo, Južna Afrika

Modularna ureditev vnaprej določenih časovnih normativov (MODAPTS) je uspešna in učinkovita metoda za meritve dela in z njim povezanih dejavnosti. Časovni normativi se uporabljajo po vsem svetu in v različnih panogah, metoda pa je stara, počasna in zahtevna za uporabnike začetnike. V pričujoči študiji je bila uporabljena nevronska mreža za modeliranje modularne ureditve vnaprej določenih časovnih standardov. Kot primarni vir podatkov za učenje so bile uporabljene ključne besede MODAPTS. Za učenje so bili pridobljeni surovi podatki v obliki časovnih študij MODAPTS. Podatki so bili nato razgrajeni in obdelani za določitev ključnih besed za učenje nevronske mreže. Učenje nevronske mreže je bilo opravljeno tudi na podlagi podatkov, zbranih z algoritmom TensorFlow s pomočjo knjižnice Keras. Najprej je bilo opravljeno učenje osnov za pripravo nevronske mreže. Umetna nevronska mreža (ANN) je bila nato implementirana z različnimi orodji, kot sta programski jezik Keras in knjižnica Keras. Rezultati kažejo, da je bila nevronska mreža 94,7-odstotno uspešna pri napovedih, le 5,3 odstotka kod pa je bilo vnesenih ročno za popravljanje klepetalnega robota ANN. Srednja vrednost razlike med metodama znaša 0,25 minute, t-test je bil izračunan s 95 % stopnjo zaupanja (0,05) in vrednost P je znašala 0,9663. Izračunana vrednost P je večja od 0,05, kar pomeni, da ni signifikantne razlike med generiranima študijama. Rezultati kažejo, da lahko pristop z ANN nadomesti utrudljivo ročno izvajanje MODAPTS z razpredelnicami in drugimi zamudnimi sredstvi. Čeprav je potrebno določeno predznanje na področju MODAPTS, si lahko novinci s predstavljeno metodo znatno skrajšajo čas za učenje in razumevanje časovnih normativov. Klepetalni robot lahko sledi uporabniškim dogodkom in zato bo za potrebe inženirjev oz. razvoja mogoče razviti dodatne vzorce poleg tistih, ki so že omenjeni v raziskavi.

Izkazalo se je tudi to, da lahko metoda MODAPTS ob podpori aplikacij strojnega učenja, kot so nevronske mreže, nadomesti zamudne analize MODAPTS na računalniku z mobilno alternativo, ki nenehno spremlja uporabnika za izboljšanje celotne analize. Predloga, ki je predstavljena v pričujoči študiji, ima velik potencial za izboljšanje in izpopolnitev meritev delovnih procesov. Predloga je tudi dovolj fleksibilna, da jo je mogoče oblikovati v orodje, ki ga lahko vsi inženirji prilagodijo potrebam svojega delovnega okolja ter ni omejeno le na avtomobilsko industrijo. Izmenjava podatkov med inženirji je olajšana zahvaljujoč deskriptivni podatkovni bazi. Obstaja torej potencial za dodajanje drugih tehnik strojnega učenja med metode časovnih študij. Študija predstavlja novost, saj sklopitev MODAPTS z nevronsko mrežo za razširitev uporabnosti metode MODAPTS v smeri hitrega usvajanja za meritve delovnih procesov in analizo gibanj ni dovolj obdelana v dostopni literaturi. Pristop z ANN občutno poenostavlja implementacijo metode MODAPTS v različnih panogah zahvaljujoč prilagodljivim ključnim besedam in sposobnosti klepetalnega robota za prepoznavanje narečij.

Ključne besede: umetna nevronska mreža, modularna ureditev vnaprej določenih časovnih normativov, algoritem TensorFlow

*Naslov avtorja za dopisovanje: Tehniška univerza Tshwane, Oddelek za industrijski inženiring, Južna Afrika, afolabiilesanmi@yahoo.com

Strojniški vestnik - Journal of Mechanical Engineering 69(2023)1-2, SI 8

Prejeto v recenzijo: 2022-09-24
Prejeto popravljeno: 2022-12-25
Odobreno za objavo: 2023-01-19

Analitične formule in uporaba vertikalnega dinamičnega odgovora železniških vozil

Yuewei Yu – Yunpeng Song – Leilei Zhao* – Changcheng Zhou
Tehniška univerza v Shandongu, Šola za transport in avtomobilsko tehniko, Kitajska

Parametri vzmetenja podstavnih vozičkov pomembno vplivajo na stabilnost teka, varnost in udobje železniških vozil. Izbira parametrov sistemov vzmetenja je zato ključna pri projektiranju podstavnih vozičkov. Konstruktorji za hitro in učinkovito odločanje pogosto uporabljajo analitično metodo, t. j. smiselno poenostavijo model na podlagi teoretične analize in nato določijo parametre blaženja s pomočjo tega modela. S tem problemom se je ukvarjalo že veliko raziskovalcev, ki so razvili različne analitične formule za izračun efektivne vrednosti (RMS) vertikalnega vibracijskega odgovora železniških vozil. Te analitične formule pa so običajno pridobljene na podlagi poenostavljene formule za gostoto močnostnega spektra nepravilnosti na progi, kar močno odstopa od dejanskega stanja.

Za odpravo tega problema je bila najprej uporabljena metoda integralske rešitve funkcije s kompleksnimi spremenljivkami za določitev analitičnih formul za efektivno vrednost (RMS) vertikalnega pospeška vagona, vertikalnega hoda sekundarnega vzmetenja in vertikalne sile ohišja osnega ležaja pod vplivom naključnega vzbujanja proge, ki bolje posnema dejansko stanje med vožnjo. Pravilnost analitičnih formul je bila preverjena s preizkusi na vozilu. S pomočjo izpeljanih analitičnih formul je bila nato oblikovana analitična metoda za projektiranje optimalne stopnje dušenja sekundarnega vertikalnega vzmetenja na podlagi večciljnega programiranja in enociljne analize omejitve intervalov, ki daje najboljši kompromis pri nasprotujočih si zahtevah, kot so udobje, mirna vožnja in varnost. Končno so bili analizirani vplivi parametrov sistema na optimalno stopnjo blaženja. Pri izbiri parametrov blaženja sekundarnega vertikalnega vzmetenja je treba poleg parametrov samega vozila upoštevati tudi vpliv hitrosti vožnje.

Analitične formule za efektivno vrednost, predstavljene v članku, lahko v primerjavi z obstoječimi pristopi bolj smiselno in točno ocenijo lastnosti vertikalne dinamike vozila na progi. Predlagana analitična metoda za določitev optimalne stopnje blaženja bo lahko učinkovito teoretično izhodišče pri izbiri začetnih vrednosti parametrov sekundarnega vertikalnega vzmetenja železniških vozil. Omeniti je treba, da je bila raziskava opravljena na podlagi poenostavljenega modela, ki učinkovito popisuje samo lastnosti vertikalnih vibracij železniških vozil ter ni primeren za horizontalni vibracijski odgovor železniških vozil. V prihodnjih študijah bo mogoče določiti še analitične formule za efektivno vrednost horizontalnega vibracijskega odgovora železniških vozil na podlagi poenostavljenega modela, da bodo lahko konstruktorji hitro in učinkovito ocenjevali oz. določali tudi horizontalni vibracijski odgovor železniških vozil in pripadajoče parametre vzmetenja.

Ključne besede: železniško vozilo, vertikalni dinamični odgovor, izpeljava modela, projektiranje parametrov blaženja, optimalen kompromis, analiza vpliva stopnje blaženja

*Corr. Author's Address: Tehniška univerza v Shandongu, Šola za transport in avtomobilsko tehniko, Zibo, Kitajska, zhaoleilei611571@163.com

Guide for Authors

All manuscripts must be in English. Pages should be numbered sequentially. The manuscript should be composed in accordance with the Article Template given above. The suggested length of contributions is 10 to 20 pages. Longer contributions will only be accepted if authors provide justification in a cover letter. For full instructions see the Information for Authors section on the journal's website: http://en.sv-jme.eu .

SUBMISSION:

Submission to SV-JME is made with the implicit understanding that neither the manuscript nor the essence of its content has been published previously either in whole or in part and that it is not being considered for publication elsewhere. All the listed authors should have agreed on the content and the corresponding (submitting) author is responsible for having ensured that this agreement has been reached. The acceptance of an article is based entirely on its scientific merit, as judged by peer review. Scientific articles comprising simulations only will not be accepted for publication; simulations must be accompanied by experimental results carried out to confirm or deny the accuracy of the simulation. Every manuscript submitted to the SV-JME undergoes a peer-review process.

The authors are kindly invited to submit the paper through our web site: http://ojs.sv-jme.eu. The Author is able to track the submission through the editorial process - as well as participate in the copyediting and proofreading of submissions accepted for publication - by logging in, and using the username and password provided.

SUBMISSION CONTENT:

The typical submission material consists of:

- A **manuscript** (A PDF file, with title, all authors with affiliations, abstract, keywords, highlights, inserted figures and tables and references),
- Supplementary files:
  - a **manuscript** in a WORD file format
  - a **cover letter** (please see instructions for composing the cover letter)
  - a ZIP file containing **figures** in high resolution in one of the graphical formats (please see instructions for preparing the figure files)
  - possible **appendicies** (optional), cover materials, video materials, etc.

Incomplete or improperly prepared submissions will be rejected with explanatory comments provided. In this case we will kindly ask the authors to carefully read the Information for Authors and to resubmit their manuscripts taking into consideration our comments.

COVER LETTER INSTRUCTIONS:

Please add a **cover letter** stating the following information about the submitted paper:

1. Paper **title**, list of **authors** and their **affiliations**. **One** corresponding author should be provided.
2. **Type of paper**: original scientific paper (1.01), review scientific paper (1.02) or short scientific paper (1.03).
3. A **declaration** that neither the manuscript nor the essence of its content has been published in whole or in part previously and that it is not being considered for publication elsewhere.
4. State the **value of the paper** or its practical, theoretical and scientific implications. What is new in the paper with respect to the state-of-the-art in the published papers? Do not repeat the content of your abstract for this purpose.
5. We kindly ask you to suggest at least two **reviewers** for your paper and give us their names, their full affiliation and contact information, and their scientific research interest. The suggested reviewers should have at least two relevant references (with an impact factor) to the scientific field concerned; they should not be from the same country as the authors and should have no close connection with the authors.

FORMAT OF THE MANUSCRIPT:

The manuscript should be composed in accordance with the Article Template. The manuscript should be written in the following format:

- A **Title** that adequately describes the content of the manuscript.
- A list of **Authors** and their **affiliations**.
- An **Abstract** that should not exceed 250 words. The Abstract should state the principal objectives and the scope of the investigation, as well as the methodology employed. It should summarize the results and state the principal conclusions.
- 4 to 6 significant **key words** should follow the abstract to aid indexing.
- 4 to 6 **highlights;** a short collection of bullet points that convey the core findings and provide readers with a quick textual overview of the article. These four to six bullet points should describe the essence of the research (e.g. results or conclusions) and highlight what is distinctive about it.
- An **Introduction** that should provide a review of recent literature and sufficient background information to allow the results of the article to be understood and evaluated.
- A **Methods** section detailing the theoretical or experimental methods used.
- An **Experimental section** that should provide details of the experimental set-up and the methods used to obtain the results.
- A **Results** section that should clearly and concisely present the data, using figures and tables where appropriate.
- A **Discussion** section that should describe the relationships and generalizations shown by the results and discuss the significance of the results, making comparisons with previously published work. (It may be appropriate to combine the Results and Discussion sections into a single section to improve clarity.)
- A **Conclusions** section that should present one or more conclusions drawn from the results and subsequent discussion and should not duplicate the Abstract.
- **Acknowledgement** (optional) of collaboration or preparation assistance may be included. Please note the source of funding for the research.
- **Nomenclature** (optional). Papers with many symbols should have a nomenclature that defines all symbols with units, inserted above the references. If one is used, it must contain all the symbols used in the manuscript and the definitions should not be repeated in the text. In all cases, identify the symbols used if they are not widely recognized in the profession. Define acronyms in the text, not in the nomenclature.
- **References** must be cited consecutively in the text using square brackets [1] and collected together in a reference list at the end of the manuscript.
- **Appendix(-icies)** if any.

SPECIAL NOTES

Units: The SI system of units for nomenclature, symbols and abbreviations should be followed closely. Symbols for physical quantities in the text should be written in italics (e.g. *v*, *T*, *n*, etc.). Symbols for units that consist of letters should be in plain text (e.g. ms^{-1}, K, min, mm, etc.). Please also see: http://physics.nist.gov/cuu/pdf/sp811.pdf .

Abbreviations should be spelt out in full on first appearance followed by the abbreviation in parentheses, e.g. variable time geometry (VTG). The meaning of symbols and units belonging to symbols should be explained in each case or cited in a **nomenclature** section at the end of the manuscript before the References.

Figures (figures, graphs, illustrations digital images, photographs) must be cited in consecutive numerical order in the text and referred to in both the text and the captions as Fig. 1, Fig. 2, etc. Figures should be prepared without borders and on white grounding and should be sent separately in their original formats. If a figure is composed of several parts, please mark each part with a), b), c), etc. and provide an explanation for each part in Figure caption. The caption should be self-explanatory. Letters and numbers should be readable (Arial or Times New Roman, min 6 pt with equal sizes and fonts in all figures). Graphics (submitted as supplementary files) may be exported in resolution good enough for printing (min. 300 dpi) in any common format, e.g. TIFF, BMP or JPG, PDF and should be named Fig1.jpg, Fig2.tif, etc. However, graphs and line drawings should be prepared as vector images, e.g. CDR, AI. Multi-curve graphs should have individual curves marked with a symbol or otherwise provide distinguishing differences using, for example, different thicknesses or dashing.

Tables should carry separate titles and must be numbered in consecutive numerical order in the text and referred to in both the text and the captions as Table 1, Table 2, etc. In addition to the physical quantities, such as *t* (in italics), the units [s] (normal text) should be added in square brackets. Tables should not duplicate data found elsewhere in the manuscript. Tables should be prepared using a table editor and not inserted as a graphic.

REFERENCES:

A reference list must be included using the following information as a guide. Only cited text references are to be included. Each reference is to be referred to in the text by a number enclosed in a square bracket (i.e. [3] or [2] to [4] for more references; do not combine more than 3 references, explain each). No reference to the author is necessary.

References must be numbered and ordered according to where they are first mentioned in the paper, not alphabetically. All references must be complete and accurate. Please add DOI code when available. Examples follow.

Journal Papers:

Surname 1, Initials, Surname 2, Initials (year). Title. *Journal*, volume, number, pages, DOI code.

[1] Hackenschmidt, R., Alber-Laukant, B., Rieg, F. (2010). Simulating nonlinear materials under centrifugal forces by using intelligent cross-linked simulations. *Strojniški vestnik - Journal of Mechanical Engineering,* vol. 57, no. 7-8, p. 531-538, DOI:10.5545/sv-jme.2011.013.

Journal titles should not be abbreviated. Note that journal title is set in italics.

Books:

Surname 1, Initials, Surname 2, Initials (year). Title. Publisher, place of publication.

[2] Groover, M.P. (2007). *Fundamentals of Modern Manufacturing*. John Wiley & Sons, Hoboken.

Note that the title of the book is italicized.

Chapters in Books:

Surname 1, Initials, Surname 2, Initials (year). Chapter title. Editor(s) of book, book title. Publisher, place of publication, pages.

[3] Carbone, G., Ceccarelli, M. (2005). Legged robotic systems. Kordić, V., Lazinica, A., Merdan, M. (Eds.), Cutting Edge Robotics. Pro literatur Verlag, Mammendorf, p. 553-576.

Proceedings Papers:

Surname 1, Initials, Surname 2, Initials (year). Paper title. Proceedings title, pages.

[4] Štefanić, N., Martinčević-Mikić, S., Tošanović, N. (2009). Applied lean system in process industry. *MOTSP Conference Proceedings*, p. 422-427.

Standards:

Standard-Code (year). Title. Organisation. Place.

[5] ISO/DIS 16000-6.2:2002. *Indoor Air – Part 6: Determination of Volatile Organic Compounds in Indoor and Chamber Air by Active Sampling on TENAX TA Sorbent, Thermal Desorption and Gas Chromatography using MSD/FID.* International Organization for Standardization. Geneva.

WWW pages:

Surname, Initials or Company name. Title, from http://address, date of access.

[6] Rockwell Automation. Arena, from *http://www.arenasimulation.com,* accessed on 2009-09-07.

EXTENDED ABSTRACT:

When the paper is accepted for publishing, the authors will be requested to send an **extended abstract** (approx. one A4 page or 3500 to 4000 characters or approx. 600 words). The instruction for composing the extended abstract are published on-line: http://www.sv-jme.eu/information-for-authors/ .

COPYRIGHT:

Authors submitting a manuscript do so on the understanding that the work has not been published before, is not being considered for publication elsewhere and has been read and approved by all authors. The submission of the manuscript by the authors means that the authors automatically agree to publish the paper uder CC-BY 4.0 Int. or CC-BY-NC 4.0 Int. when the manuscript is accepted for publication. All accepted manuscripts must be accompanied by a Copyright Agreement, which should be sent to the editor. The work should be original work by the authors and not be published elsewhere in any language without the written consent of the publisher. The proof will be sent to the author showing the final layout of the article. Proof correction must be minimal and executed quickly. Thus it is essential that manuscripts are accurate when submitted. Authors can track the status of their accepted articles on https://en.sv-jme.eu/.

PUBLICATION FEE:

Authors will be asked to pay a publication fee for each article prior to the article appearing in the journal. However, this fee only needs to be paid after the article has been accepted for publishing. The fee is 380 EUR (for articles with maximum of 6 pages), 470 EUR (for articles with maximum of 10 pages), plus 50 EUR for each additional page. The additional cost for a color page is 90.00 EUR (only for a journal hard copy; optional upon author's request). These fees do not include tax.

Strojniški vestnik -Journal of Mechanical Engineering
Aškerčeva 6, 1000 Ljubljana, Slovenia, e-mail: info@sv-jme.eu

9 770039 248001
ISSN 0039-2480

http://www.sv-jme.eu

Contents

Papers